DESIGN AND IMPLEMENTATION OF RECONFIGURABLE TRANSMITARRAY
UNIT CELLS EMPLOYING THE ELEMENT ROTATION METHOD BY
MICROFLUIDICS


A THESIS SUBMITTED TO
THE GRADUATE SCHOOL OF NATURAL AND APPLIED SCIENCES
OF
THE MIDDLE EAST TECHNICAL UNIVERSITY


BY

EMRE ERDİL


IN PARTIAL FULFILMENT OF THE REQUIREMENTS
FOR
THE DEGREE OF DOCTOR OF PHILOSOPHY
IN
ELECTRICAL AND ELECTRONICS ENGINEERING


SEPTEMBER 2014

Approval of the thesis:

# DESIGN AND IMPLEMENTATION OF RECONFIGURABLE TRANSMITARRAY UNIT CELLS EMPLOYING THE ELEMENT ROTATION METHOD BY MICROFLUIDICS

submitted by **EMRE ERDİL** in partial fulfillment of the requirements for the degree of **Doctor of Philosophy in Electrical and Electronics Engineering Department**, **Middle East Technical University** by,

Prof. Dr. Canan Özgen
Dean, Graduate School of **Natural and Applied Sciences**　　—————————

Prof. Dr. Gönül Turhan Sayan
Head of Department, **Electrical and Electronics Eng.**　　—————————

Prof. Dr. Özlem Aydın Çivi
Supervisor, **Electrical and Electronics Eng. Dept., METU**　—————————

Assist. Prof. Dr. Kağan Topallı
Co-Supervisor, **UNAM, Bilkent University**　　—————————

**Examining Committee Members:**

Prof. Dr. Gülbin Dural
Electrical and Electronics Eng. Dept., METU　　—————————

Prof. Dr. Özlem Aydın Çivi
Electrical and Electronics Eng. Dept., METU　　—————————

Prof. Dr. Sencer Koç
Electrical and Electronics Eng. Dept., METU　　—————————

Assoc. Prof. Dr. Lale Alatan
Electrical and Electronics Eng. Dept., METU　　—————————

Assoc. Prof. Dr. Vakur B. Ertürk
Electrical and Electronics Eng. Dept., Bilkent University　—————————

**Date**:　　01/09/2014

**I hereby declare that all information in this document has been obtained and presented in accordance with academic rules and ethical conduct. I also declare that, as required by these rules and conduct, I have fully cited and referenced all material and results that are not original to this work.**

Name, Last name: Emre ERDİL

Signature:

# ABSTRACT

## DESIGN AND IMPLEMENTATION OF RECONFIGURABLE TRANSMITARRAY UNIT CELLS EMPLOYING THE ELEMENT ROTATION METHOD BY MICROFLUIDICS

Erdil, Emre

Ph. D., Department of Electrical and Electronics Engineering

Supervisor: Prof. Dr. Özlem Aydın Çivi

Co-Supervisor: Assist. Prof. Dr. Kağan Topallı

September 2014, 131 pages

This thesis presents design, fabrication and measurement of a novel, continuously tunable, circularly polarized X-band microfluidic transmitarray unit cell. To the author's knowledge, this is the first study in the literature where a microfluidics approach is used to tune the phase of the transmitted field through the unit cell by the element rotation method. Furthermore, the generalized transmitarray design conditions necessary to utilize the element rotation method are derived. To implement the novel microfluidic approach, a unit cell comprising a double layer nested ring-split ring is realized as microfluidic channels embedded in Polydimethylsiloxane using soft

lithography techniques and bonded to a glass substrate. Conductive regions of the rings are formed by injecting a liquid metal (an alloy of Ga, In, and Sn), whereas the split region is the air gap in the inner ring. Movement of the liquid metal together with the split around the ring realizes the rotation of the unit cell around its axis, which controls the phase of the transmitted field through the unit cell and provides 360° linear phase shift range. A circularly polarized unit cell is designed by using periodic boundary conditions to implement the infinite array approach and satisfies the design conditions at 8.8 GHz. To realize the rotation, unit cell prototypes at different split positions are fabricated in the facilities of METU and the proposed concept is verified by the measurements using the waveguide simulator method, within the frequency range of 8−10 GHz. The simulation and measurement results show a fair agreement, illustrating the viability of the approach to be used in reconfigurable reflectarrays and transmitarrays.


Keywords: Transmitarray, microfluidics, reconfigurable, split ring, element rotation method.

# ÖZ

# MİKROAKIŞKAN TEKNOLOJİSİ İLE ELEMAN DÖNDÜRME METODUNU UYGULAYAN AYARLANABİLİR İLETİ DİZİ BİRİM HÜCRELERİ TASARIMI VE ÜRETİMİ

Erdil, Emre

Doktora, Elektrik ve Elektronik Mühendisliği Bölümü

Tez Yöneticisi: Prof. Dr. Özlem Aydın Çivi

Ortak Tez Yöneticisi: Yrd. Doç. Dr. Kağan Topallı

Bu tezde, kesintisiz biçimde ayarlanabilen, dairesel kutuplu yeni bir X-bant mikroakışkan ileti dizi birim hücresinin tasarımı, üretimi ve ölçümü sunulmaktadır. Bu çalışma, yazarın bilgisi dahilinde, literatürde mikroakışkan tekniğinin birim hücrede iletilen alanın fazının eleman döndürme yöntemiyle ayarlanması için kullanıldığı ilk çalışmadır. Ayrıca, eleman döndürme yöntemini uygulayabilmek için gerekli olan genelleştirilmiş tasarım koşulları ileti diziler için türetilmiştir. Birim hücre, yumuşak baskı litografisi teknikleri kullanılarak polidimetilsiloksan içine gömülen ve cam tabana yapıştırılan çift katmanlı iç içe geçmiş halka-ayrık halka

yapısını içermektedir. Halkaların iletken kısımları (Ga, In ve Sn karışımı olan) bir sıvı metalin enjekte edilmesiyle, ayrık bölgesi ise iç halkadaki hava boşluğundan oluşmaktadır. Sıvı metalin ayrık ile beraber halka içinde hareket etmesi, birim hücrenin ekseni etrafında dönmesini gerçekleştirmekte, bu sayede birim hücre üzerinden iletilen alanın fazını kontrol etmekte ve 360° doğrusal faz kayma menzili sağlamaktadır. 11.43 mm × 10.16 mm alan kaplayan ve eleman döndürme metodunun doğrusal faz kaydırmak için gerektirdiği koşulları 8.8 GHz'de sağlayan dairesel kutuplu birim hücre sonsuz dizi yaklaşımını uygulayacak şekilde periyodik sınır koşulları kullanılarak tasarlanmıştır. Ayrığın dönüşünü benzeştirecek şekilde farklı ayrık konumlarına sahip birim hücre prototipleri ODTÜ tesislerinde üretilmiş ve önerilen yaklaşım dalga kılavuzunda ölçümler yapılarak, 8-10 GHz aralığında doğrulanmıştır. Benzetim ve ölçüm sonuçları tatmin edici benzerlik sergilemekte ve sunulan yaklaşımın ayarlanabilir yansıtıcı anten ve ileti anten dizilerinde kullanılabilirliğini göstermektedir.


Anahtar Kelimeler: İleti dizi, mikroakışkanlar, ayarlanabilir, ayrık halka, eleman döndürme yöntemi.

*To Evren and Deniz*

# ACKNOWLEDGMENTS

# TABLE OF CONTENTS

# LIST OF TABLES

# LIST OF FIGURES

# CHAPTER 1

# INTRODUCTION

In long range communication systems and millimeter-wave radars, high gain antennas are required to enhance the performance of the system. Typically, phased arrays, parabolic reflectors, and dielectric lenses are used to increase the gain. Phased arrays need large feed networks increasing cost and RF loss. Parabolic reflectors are bulky and hard to manufacture especially at high frequencies due to their curved structure. Moreover parabolic reflectors are more suitable for fixed beam applications [1]. Dielectric lenses are high-cost antennas [2]. Reflectarrays and transmitarrays, also called as lens arrays, are planar alternatives for achieving high antenna gain by combining the best features of phased arrays and parabolic reflectors. These structures eliminate the manufacturing difficulties coming from the non-planar surfaces of the reflectors. They need a simple feed antenna illuminating the planar array of printed elements and the usage of space feeding removes the loss and parasitic effects of the complicated feed networks in phased arrays [3]. It is also possible to implement beam steering as it allows the integration of tunable elements. In conclusion, to achieve high gain, compared to other options such as parabolic reflectors, dielectric lenses, and phased arrays; reflectarrays and transmitarrays are promising alternatives that provide a planar, lightweight, and low volume solution with their simpler and low loss beamforming networks.

Transmitarray surface consisting of a planar array of printed elements is illuminated by a feed antenna on one side of the array and the radiation is produced on the other side as shown in Figure 1.1, whereas for reflectarrays, the radiation is produced on the

same side with the feed antenna. Therefore, the offset feed applied to prevent feed blockage in reflectarrays is not required in transmitarrays. Illumination of the transmitarray surface by a feed antenna at the center reduces the angle of incidence to elements even located close to the edges. This prevents the growth in the grating lobes as formed in reflectarrays [1]. The difference in the side utilization between the reflectarrays and transmitarrays also differentiates their possible application areas. Transmitarrays need space on both sides for excitation and radiation whereas reflectarrays, being single sided structures, can be mounted on a flat surface. The design criteria of reflectarrays and transmitarrays are also different. Due to the presence of a ground plane, the reflection of the incident wave is ensured in the reflectarrays whereas in the transmitarray designs, high level of transmission should be provided while inserting the required phase value at each element.
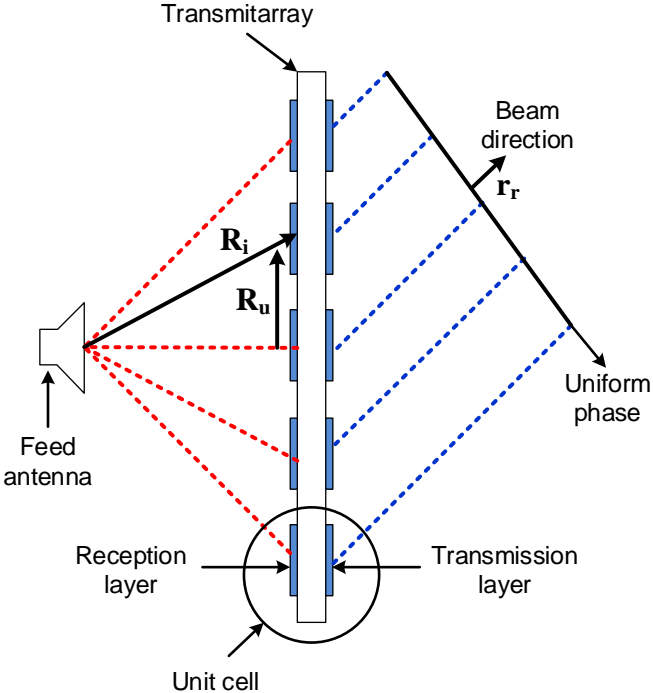


Figure 1.1    Conceptual drawing of a transmitarray. A planar phasefront is achieved by controlling the phase shift on the antenna elements.

Number of studies on beam forming transmitarray applications for satellite communications and radars and usage of microfluidics on antennas for designing wearable, stretchable radiators for sensor applications are increasing tremendously in the last decade. The aim of this thesis is to design novel transmitarray unit cells whose transmitted phase can be adjusted by using microfluidics and proposing a novel technique for the implementation of the element rotation method. To the author's knowledge the designs presented in this thesis are the first examples of the transmitarray unit cells whose reconfiguration is enabled by using microfluidics in the literature. It is considered that this reconfiguration mechanism will be inspiring and encouraging for the future efforts combining microfluidics with antenna engineering in order to eliminate the disadvantages of the previous approaches used in the implementation of reconfigurable antennas. Figure 1.2 (a) shows an illustration of a split ring unit cell structure for implementing the element rotation method by microfluidics. The rings are in the form of microfluidic channels where the liquid metal is confined in. The liquid metal can be inserted inside the channels by feed lines. Rotation of the split region together with the liquid metal performs the rotation of the element which tunes the transmitted phase through the unit cell. It is demonstrated in this thesis that the characteristics of the unit cell and the phase shifting technique is proper to construct a reconfigurable beam steering transmitarray from these elements. Figure 1.2 (b) shows an illustration of a typical transmitarray consisting of microfluidic split ring unit cells.

## 1.1. Transmitarray Overview

Transmitarrays are illuminated by an incident spherical wave coming from a feed antenna and radiate it with a planar phase front. The electromagnetic wave coming from the center-positioned feed antenna is incident on each element with a phase difference related to the distance between the elements. To achieve a planar phase front on the transmitting side or to rotate the beam to the desired direction, these phase

differences should be compensated by tuning the phase of each element at a specific value. The required transmission phase value of each element, $\Phi_i$ should satisfy,

$$k_0(R_i - \boldsymbol{R_u}.\boldsymbol{r_r}) - \Phi_i = 2\pi N \qquad (1.1)$$

where $N$ is an integer, $k_0$ is the wavenumber in free space, the distance from the feed center to the $i^{th}$ unit element is $R_i$, the vector from the center element to the $i^{th}$ element is $\boldsymbol{R_u}$, and the unit vector in the desired transmitted beam direction is $\boldsymbol{r_r}$, respectively, as shown in Figure 1.1.

To reconfigure the beam for any angular direction, the elements must be capable of providing 360° of phase range. Transmitarray elements are generally cascaded in multilayers in order to increase the phase range as each layer has a limited effect on the amount of transmitted phase and to decrease the insertion loss level [4]-[7]. The layer opposite the feed antenna, the reception layer, receives the electromagnetic wave coming from the feed antenna. The received electromagnetic wave is coupled between the layers by using slots in the ground plane [4], by using vias connecting the reception and transmission elements [8], or by direct coupling through the substrate between the layers [9]. The phase-adjusted plane wave is radiated from the transmission layer.

The adjustment in the transmission phase of each unit cell can be realized by changing the lengths of the delay lines (transmission line, stub, stripline) or resonators in the unit cells, by loading the resonators, by rotating the elements in the array, or by integrating phase shifters or varactors. The transmitarrays can be categorized as fixed beam or reconfigurable according to the tuning methodology. The researches including these categories together with the studies on bandwidth are given in the following sections.
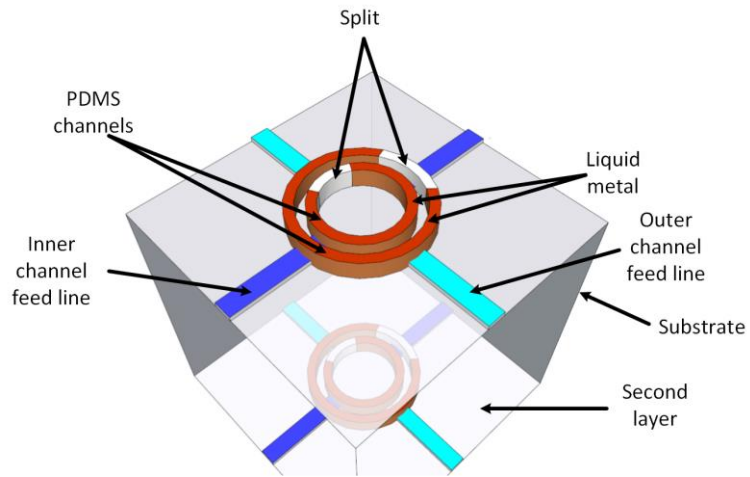
(a)
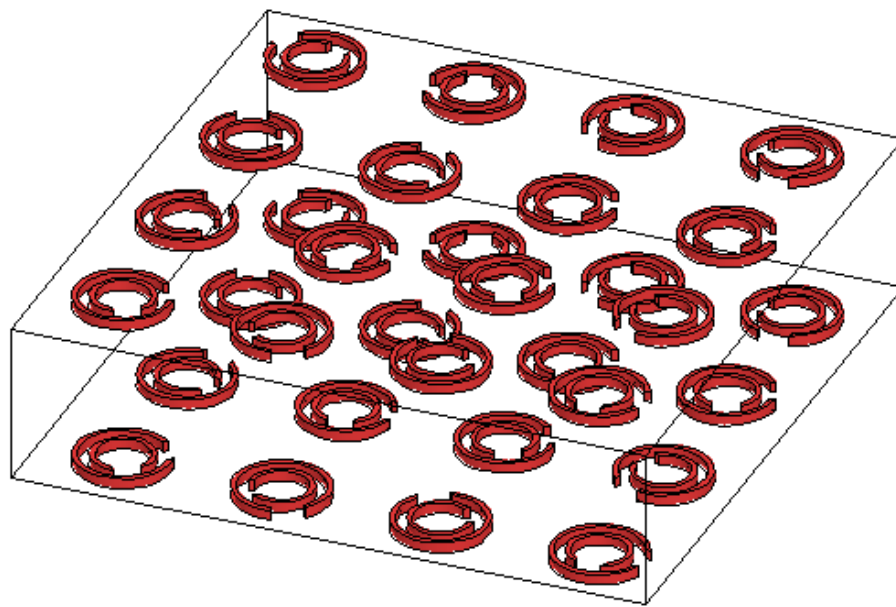


(b)

Figure 1.2    (a) 3-D view of a split ring unit cell for the implementation of the element rotation method by microfluidics. (b) An illustration of a transmitarray composed of the unit cells in (a).

### 1.1.1. Fixed Beam Transmitarrays

This category includes the transmitarrays radiating in a fixed direction with a static phase difference between its elements. The necessary phase difference between the elements is achieved by varying the resonator dimensions or varying the length of the delay lines either attached to the radiators or placed in a layer between the radiators to modify the traveling length of the guided wave coupled to it. This mechanism is also suitable for discretized reconfiguration by integrating variable switches to control the effective length. However, it should be noted that the effective length is constant in fixed beam applications and these applications are presented in this section.

The first transmitarray structure in the literature is proposed by McGrath and it is a double layer planar array of radiators utilizing variable length transmission lines for phase tuning [8]. The received electromagnetic wave is coupled to these lines connected to the radiators. A shorting pin through an aperture in the ground plane between the radiators provides the connection between the transmission lines. Different structures are examined in terms of phase agility by Pozar [4]. Using a single variable, the length of the slot in the ground plane in a frequency selective surface (FSS), 70°-100° of phase agility is obtained. Increasing the number of variables by using varying length patches on the reception and transmission layers, the phase agility is increased up to 150°-180°. By aperture coupling of two parallel resonant patches to a variable length stripline, the phase agility is increased further. In a similar fixed-beam application where the phase is controlled by changing the length of the transmission lines between the two ground planes, two designs showing a broadside pattern and 10° vertical tilt pattern are manufactured [10].

Another design demonstrates two coupled patches via a variable length CPW line [11]. The design is aimed to steer the beam for three different angles by changing the position of the feed. This beam scanning method is also used in an application where -40° to +40° beam scanning is achieved by switching between the feeds and controlling

6

the phase by the length of the stripline [12]. This feed switching method is not categorized as reconfigurable as the reconfiguration is not provided electronically.

The major drawback of changing the length of the delay lines method is the necessity of long delay lines to satisfy the required phase value, which expands the unit cell size resulting in the formation of grating lobes. Also, when the length of the delay line is long, spurious cross-polarized radiation is formed and undesired modes are generated [9].

## 1.1.2. Reconfigurable Transmitarrays

Dynamical reconfiguration of the phase distribution of the unit cell enables beam steering. To reconfigure the beam for any angular direction, the unit cells should be capable of providing 360° of phase agility. To this end, switches, microelectromechanical systems (MEMS) components, varactors, and phase shifters are used. These components are used for adaptive change of the electrical characteristics of the radiators or shifting the phase of the electromagnetic wave coupled between the layers, dynamically.

To focus the beam of the transmitarray, a multigrid approach is applied in [13] where the structure composed of 30 × 30 elements divided into 5 × 5 unit blocks. Unit cell reactance is changed by utilizing a switch within each element. All the switches in a unit block are biased such that all the switches are either on or off in a unit block making 1-bit reconfiguration possible. 1-bit phase resolution reduces the complexity of the structure however it also reduces the radiation performance [14].

In a reconfigurable transmitarray structure, the length of the striplines can be changed by activating different segments of the lines using MEMS switches [3]. Four different modes having 90° of phase difference with respect to the preceding mode is obtained

by this activation. The required mode to achieve the planar phasefront and beam steering for each element is implemented. This modular approach is successful in beam steering but the quantization of the phase prevents continuous phase shifting causing a phase error loss of 0.75 dB. Another work using similar concept shows 1-D beamforming for 0°, 10°, 20°, 30°, 40°, and 50° of beamscanning [15]. Since the biasing is established only for each row, 2-D beamforming is not achieved. For 2-D beamforming each cell in the lens array must be biased independently. However, the bias lines that are required for carrying DC actuation voltages of MEMS switches cause parasitic radiation. In order to alleviate this issue, the use of high-resistive lines is suggested [15], which adds additional steps to the manufacturing process. Another drawback of MEMS technology is the reliability problems such as contact degradation, dielectric charging, and fatigue that may occur in MEMS switches. Furthermore, continuous tunability cannot be obtained by reconfigurable structures with switches.

In addition to MEMS switches, active devices such as diodes or varactors are also employed in reconfigurable transmitarrays to change the characteristic impedance of the unit cell. However, the power consumption and the complexity of the arrays increase significantly for large arrays [16], [13]. Also, only limited phase range could be achieved by using varactors due to the limitations of their capacitance ranges [16], [17]. Another solution for the implementation of reconfigurable transmitarrays is the use of phase shifting elements placed in between direct-coupled [18] or proximity-coupled [19] receive and transmit layers. The phase shifter and the lines used for coupling increase the dimensions of the unit cells, preventing the implementation of high-density transmitarrays.

### 1.1.2.1.  The Element Rotation Method

The element rotation method, which enables realization of transmitarray and reflectarray unit cells without increasing the unit cell size, is another method for phase

8

tuning and applied to the structures excited by circularly polarized electromagnetic waves [7], [20]-[24]. The method provides continuous tuning of the phase and 360° of linear phase shift can be achieved by rotating the elements of the array around the axis which is normal to the array plane. In transmitarrays, the phase of the transmitted wave is shifted twice the rotation angle providing the conditions presented in the following sections. Rotation of the elements can be realized mechanically (e.g. by using motors controlling the rotation angle of the unit cells) as suggested in [21], [22]. However, the placement of the motor for each element of the array is not practical and it might also ruin the RF performance of the transmitarrays since most transmitarrays utilize double sided radiating structures. The other approach to realize element rotation is the use of MEMS switches on a split ring structure. In a dual frequency beam switching reflectarray, rotational orientation of the split rings has been implemented by integrating series 6 RF MEMS switches uniformly distributed on the ring [23]. Although this approach is successful in orienting the beam, continuous beam steering is not possible due to finite number of switches. Actually, to this end, any reflectarray and transmitarray employing the element rotation method with continuous beam steering has not been demonstrated.

## 1.1.3. Bandwidth Studies

There are also studies, out of the aforementioned categorization, to increase the bandwidth of the transmitarrays. Transmitarrays are inherently narrow bandwidth structures. This is mainly due to the type of the radiators, patches or FSS structures, used in the transmitarrays. Also, the changes in the size of the resonators or delay lines affect the resonance frequency which has negative effect on the transmission magnitude as the magnitude is maximized for a specific size value at the operating frequency. In order to increase the bandwidth, the effect of different feed antenna types and stacked structures on bandwidth are examined in the literature [25]-[27]. Bialkowski et al. demonstrates that the uniform excitation of the array increases the

operational bandwidth [25]. Using stacked patch antennas increases the bandwidth further as by using stacked patches, the phase agility requirement for each layer decreases providing a larger bandwidth [26].

In another application, dual resonant double square elements are used [9]. The width of the inner ring of the element is varied in order to shift the transmitted phase. Fixing the size of the outer ring results in keeping one resonance frequency constant which increases the bandwidth compared to varying sizes of both rings. To enhance the phase agility, number of layers are increased.

In these studies about bandwidth, it is observed that although using stacked layers in transmitarray unit cells increases the bandwidth, it increases the thickness of the unit cell and makes the overall array bulky.

## 1.2. Microfluidics

The microfluidics deals with the processing and controlling the transportation of liquid in micro and nanoliter scales [28]. The transportation is carried out in capillary channels and controlling the amount, movement and direction is carried out by using micropumps [29], and valves [30]. The materials used in microfluidic applications are silicon [31], glass [32], ceramics [33] or polymers [34]. Polydimethylsiloxane (PDMS), one of these polymers, is the common used material due to the advantages of low cost, fast fabrication and implementation convenience [35]. PDMS is a low toxic, optically transparent, soft elastomer [28] cured on the molds formed via conventional micromachining or photolithography [35]. Electrically, it has low permittivity between 2.72-2.82 and tangent loss of 0.0119-0.0135 across 0.1-40.0 GHz frequency range [36]. Microchip systems increasing the analysis capability are developed using microfluidics and they are called as lab on a chip systems, functioning as sample preparation [37], separation [38], and sensing and detection [39]. The

application areas of microfluidic systems are focused on the chemical and biological applications on cell biology [40], bioanalysis [41], point of care diagnostics [42] and drug development [43].

## 1.2.1. Microfluidics in Antenna and Microwave Engineering

The use of conductive fluids with microfluidics enables different approaches in antenna and microwave engineering such as wearable and textile antennas which can adapt to the physical surface of the wearer without significant deviation in the response [44]-[46], stretchable antennas formed by placing liquid metal on a stretchable substrate to change the resonance frequency with the change in length [47], [48], flexible coils fabricated by encasing a liquid metal inside the channels in an elastomeric substrate [49], sensor and antenna applications related to the response of the liquid metal on the change in the temperature or pressure [50]-[53] and beam steering antennas [54], [55]. Liquid metal is used in the conductive parts of these structures. Although the commonly known liquid metal is mercury, due to its high toxicity, materials that remain liquid in a wide range of temperature with good conductivity are developed. In general, alloys of gallium, indium, and tin are preferred as they can be liquid below room temperature [56].

Another use of fluids in an RF system is demonstrated as a frequency selective surface (FSS) [57]: A fluidically tunable FSS consisting of multiple metallic layers whose surface impedance is controlled by moving a Teflon solution and a liquid metal in the tubes using a micropump. Microfluidics is also applied on reflectarrays to change the reflected phase by altering the aggregate permittivity of a colloidal dispersion [58] and on tunable bandpass filters where the shape of the broadside coupled split ring resonators is changed by moving the liquid metal forming one side of the resonators [59].

The usage of conductive fluids together with microfluidics on antennas or microwave components is quite new but the advantages that the technology offers are promising. For example, this technology might offer low-cost and low power consuming systems with continuous tuning. It is also considered that this technology might reduce the deterioration in the RF performance due to the parasitic effects caused by metallic bias lines or cabling. In this thesis, this approach is implemented to enable the element rotation method on reconfigurable transmitarray unit cells operating at X-band. The unit cells comprise double layer nested split ring structures realized as microfluidic channels embedded in PDMS using soft lithography techniques. Conductive regions of the rings are formed by injecting a liquid metal (an alloy of Ga, In, and Tin). Instead of rotating the element by means of a mechanical approach, a liquid metal confined in a channel is rotated inside the ring by using microfluidic techniques. Movement of the liquid metal together with the split around the ring provides 360° linear phase shift range in the transmitted field through the unit cells.

## 1.3.     Thesis Objectives and Organization

The goal of this thesis is to design, fabricate and measure novel reconfigurable transmitarray unit cells utilizing microfluidics. Designed unit cells are composed of split ring resonator elements. Element rotation method is used for tuning the transmitted phase and it is implemented by changing the position of the liquid metal forming the conductive part of the unit cells. The fabrication process and RF measurements are carried out at Middle East Technical University. The objectives of this thesis can be summarized as follows:

- To analyze the element rotation method for transmitarray structures and derive generalized design conditions by taking into account the linearly polarized components of the circularly polarized wave for a two port system.

- To implement the element rotation method on split ring resonator (SRR) and complementary split ring resonator (CSRR) unit cells by changing the location of the split region around the ring by means of microfluidic technology.

- To investigate the effect of geometrical symmetry on the insertion loss in SRR and CSRR type unit cells implementing the element rotation method for transmitarray applications, including,
  - The effect of the rotation to the S-parameters,
  - The field analysis to understand the effect of symmetrical geometry on the insertion loss,
  - A method proposed to decrease the insertion loss variation for unsymmetrical SRR and CSRR structures

- To design transmitarray unit cells operating at X-band which comprise double layer nested split ring structures and satisfy the necessary conditions for phase shifting,

- To explain the design methodology for satisfying the design conditions and to present a design guideline

- To fabricate the designed unit cell in different angular positions to realize the rotation of the unit cell,

- To measure the fabricated unit cells and show that an agreement is satisfied between the measurement and simulation results to verify the proposed concept.

The thesis is organized as follows:

Chapter 2 gives information about the design environment, the element rotation method and the derivations of the generalized design conditions for the implementation of the method in the transmitarrays.

Chapter 3 describes the unit cell designs. The simulation results of the structures are presented and it is shown that the design conditions are satisfied. Design methodology is also given in the chapter.

Chapter 4 gives information about the effect of the geometrical symmetry on the insertion loss variation with respect to the rotation angle. The study involves examination of the insertion loss variation on the S-parameters and field distributions of several CSRR and SRR structures and proves that the symmetrical structures has more constant insertion loss distribution over rotation angle.

Chapter 5 describes the fabrication process and the measurement results of the fabricated structures.

Chapter 6 concludes the thesis and gives information about the future work related to the subject in the thesis.

Appendix gives the illustrations, parameter values and the reflection and transmission coefficient characteristics of the CSRR and SRR type unit cell designs.

# CHAPTER 2

# ELEMENT ROTATION METHOD

## 2.1.    Introduction

The element rotation method is one of the appropriate ways of obtaining required phase shifts in a linear way for a transmitarray. As the method is shown in Figure 2.1, for a transmitarray illuminated by a circularly polarized wave, rotating the elements around the surface normal to the plane of the array provides a phase shift two times the rotation angle in the transmitted wave. The phase shifting conditions are derived and given in the following sections of this chapter together with the information about the design environment.
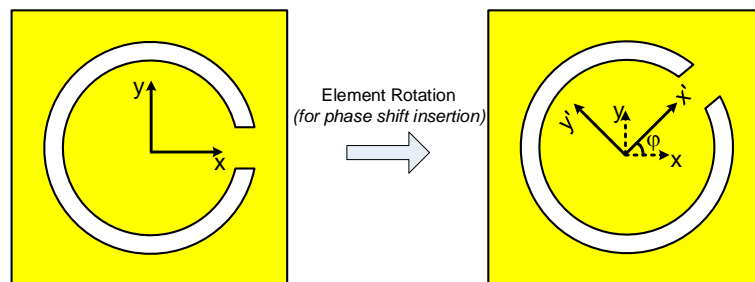


Figure 2.1      Element rotation method for phase shift insertion in split ring structures in transmitarray unit cells.

## 2.2. Design Environment

In transmitarray designs, phase design curves show the relationship between the inserted phase shift and the design variable, e. g. a physical dimension in the unit cell geometry. As such, the phase design curve provides an essential information on the change of the phase to design a transmitarray with a steered beam in a particular direction. In order to achieve the phasefront in the desired direction, it is necessary to calculate the transmitted phase value by taking into account the geometrical position of the element in the array since the distance from the feed horn to each array element is different. Then, the physical structure of each element is reconfigured to take the corresponding value in the phase design curve.

The most practical method of obtaining the phase design curve is the infinite array approach. In this approach, the array is formed by replicating identical unit cells. The approach provides an opportunity for designing array structures by analyzing only a single element, i.e., unit cell with periodic boundary conditions, including the effect of mutual coupling between the elements. In this thesis, infinite array approach is implemented using Ansys HFSS®, which is a commercially available electromagnetic solver. In HFSS®, in order to satisfy this periodicity, periodic boundary conditions are used by implementing master and slave boundaries on the unit cell walls. The E-field in any point of the slave boundary matches the correspondent point of the master boundary with a phase difference [60]. Figure 2.2 shows the illustration of the unit cell configuration used in the thesis.
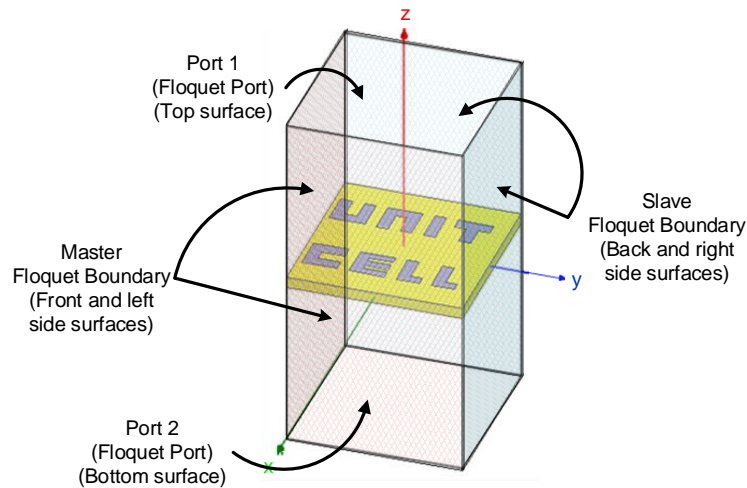
Figure 2.2    Illustration of the unit cell configuration used in the thesis.

The periodic arrangement of the array allows the approximation of the infinite array fields with Floquet modal expansion. Floquet ports are defined on the apertures of the unit cell as an interface to unbounded medium and the fields on the ports are represented by a set of Floquet modes. A Floquet mode is a plane wave function and when the unit size is less than half a wavelength, only the dominant mode propagates [7]. The propagating modes can be normalized into orthogonal modal functions, TE and TM, for simplicity. This normalization is useful in layered structures as these orthogonal modal functions propagate without producing the other transverse mode for homogeneous and isotropic media. That is, TE (TM) mode will not produce a TM (TE) mode [61]. Therefore, for a unit cell smaller than half a wavelength the propagating dominant mode is decomposed into one TE and one TM propagating modes and individual analysis of these modes are possible by using HFSS®. In this thesis, all the unit cell dimensions are smaller than half a wavelength and the normal incidence is provided by plane wave propagation in *z*- direction. For this propagation, defining a rectangular grid whose edges lie along *x*- and *y*- directions, the propagating modes are *x*- and *y*-polarized modes.

## 2.3.    Derivation of Generalized Design Conditions

In [7], the phase shifting conditions for a transmitarray are derived for symmetrical structures with respect to all orthogonal planes. In this chapter, following the same procedure, the generalized conditions are derived without restricting to the symmetry as the method is also applicable to the unsymmetrical structures.

For a two port system, the relation between the incident and scattered waves for a unit cell excited by $x$- and $y$-polarized wave modes can be written as,

$$
\begin{bmatrix} b_1^x \\ b_1^y \\ b_2^x \\ b_2^y \end{bmatrix} = \begin{bmatrix} s_{11}^{xx} & s_{11}^{xy} & s_{12}^{xx} & s_{12}^{xy} \\ s_{11}^{yx} & s_{11}^{yy} & s_{12}^{yx} & s_{12}^{yy} \\ s_{21}^{xx} & s_{21}^{xy} & s_{22}^{xx} & s_{22}^{xy} \\ s_{21}^{yx} & s_{21}^{yy} & s_{22}^{yx} & s_{22}^{yy} \end{bmatrix} \begin{bmatrix} a_1^x \\ a_1^y \\ a_2^x \\ a_2^y \end{bmatrix} \tag{2.1}
$$

where $a_m^n$ and $b_m^n$ represents the $n$-polarized incident and scattered waves for $m^{th}$ Floquet port, respectively. When the element is rotated by an angle $\psi$, the rotated scattering matrix is obtained by using the relation,

$$
S_\psi^{LP} = [R_\psi^{LP}]^{-1}[S^{LP}][R_\psi^{LP}] \tag{2.2}
$$

where the rotation matrix, $R_\psi^{LP}$, is defined as,

$$
R_\psi^{LP} = \begin{bmatrix} \cos\psi & \sin\psi & 0 & 0 \\ -\sin\psi & \cos\psi & 0 & 0 \\ 0 & 0 & \cos\psi & \sin\psi \\ 0 & 0 & -\sin\psi & \cos\psi \end{bmatrix} \tag{2.3}
$$

Also, a different scattering matrix relating the circularly polarized incident and scattered waves can be written as,

18

$$
\begin{bmatrix} b_1^l \\ b_1^r \\ b_2^r \\ b_2^l \end{bmatrix} = \begin{bmatrix} s_{11}^{lr} & s_{11}^{ll} & s_{12}^{ll} & s_{12}^{lr} \\ s_{11}^{rr} & s_{11}^{rl} & s_{12}^{rl} & s_{12}^{rr} \\ s_{21}^{rr} & s_{21}^{rl} & s_{22}^{rl} & s_{22}^{rr} \\ s_{21}^{lr} & s_{21}^{ll} & s_{22}^{ll} & s_{22}^{lr} \end{bmatrix} \begin{bmatrix} a_1^r \\ a_1^l \\ a_2^l \\ a_2^r \end{bmatrix}
\tag{2.4}
$$

Here, also the same notation in [7] is used. The superscripts $l$ and $r$ denotes the sense of the polarization, left-hand and right-hand, respectively.

The relation between the circularly polarized and linearly polarized wave modes can be established by:

$$
S_\psi^{CP} = [TR][S_\psi^{LP}][TR]^{-1}
\tag{2.5}
$$

where *TR* is the matrix transforming the coordinates from Cartesian to circular unit vectors [7]

$$
TR = \frac{1}{\sqrt{2}} \begin{bmatrix} 1 & -j & 0 & 0 \\ 1 & j & 0 & 0 \\ 0 & 0 & 1 & -j \\ 0 & 0 & 1 & j \end{bmatrix}
\tag{2.6}
$$

Each S-parameter in the scattering matrix (2.4) can be obtained by combining (2.1), (2.2) and (2.5) as,

$$
s_{11}^{lr} = \frac{1}{2} \left[ \left( s_{11}^{xx} + s_{11}^{yy} \right) + j\left( s_{11}^{xy} - s_{11}^{yx} \right) \right]
\tag{2.7}
$$

$$
s_{11}^{ll} = \frac{1}{2} \left[ \left( s_{11}^{xx} - s_{11}^{yy} \right)e^{-j2\psi} - j\left( s_{11}^{xy} + s_{11}^{yx} \right)e^{-j2\psi} \right]
\tag{2.8}
$$

$$
s_{12}^{ll} = \frac{1}{2} \left[ \left( s_{12}^{xx} + s_{12}^{yy} \right) - j\left( s_{12}^{yx} - s_{12}^{xy} \right) \right]
\tag{2.9}
$$

$$s_{12}^{lr} = \frac{1}{2}\left[(s_{12}^{xx} - s_{12}^{yy})e^{-j2\psi} - j(s_{12}^{yx} + s_{12}^{xy})e^{-j2\psi}\right] \tag{2.10}$$

$$s_{11}^{rr} = \frac{1}{2}\left[(s_{11}^{xx} - s_{11}^{yy})e^{+j2\psi} + j(s_{11}^{yx} + s_{11}^{xy})e^{+j2\psi}\right] \tag{2.11}$$

$$s_{11}^{rl} = \frac{1}{2}\left[(s_{11}^{xx} + s_{11}^{yy}) - j(s_{11}^{xy} - s_{11}^{yx})\right] \tag{2.12}$$

$$s_{12}^{rl} = \frac{1}{2}\left[(s_{12}^{xx} - s_{12}^{yy})e^{+j2\psi} + j(s_{12}^{yx} + s_{12}^{xy})e^{+j2\psi}\right] \tag{2.13}$$

$$s_{12}^{rr} = \frac{1}{2}\left[(s_{12}^{xx} + s_{12}^{yy}) - j(s_{12}^{xy} - s_{12}^{yx})\right] \tag{2.14}$$

$$s_{21}^{rr} = \frac{1}{2}\left[(s_{21}^{xx} + s_{21}^{yy}) - j(s_{21}^{yx} - s_{21}^{xy})\right] \tag{2.15}$$

$$s_{21}^{rl} = \frac{1}{2}\left[(s_{21}^{xx} - s_{21}^{yy})e^{-j2\psi} - j(s_{21}^{xy} + s_{21}^{yx})e^{-j2\psi}\right] \tag{2.16}$$

$$s_{22}^{rl} = \frac{1}{2}\left[(s_{22}^{xx} + s_{22}^{yy}) - j(s_{22}^{yx} - s_{22}^{xy})\right] \tag{2.17}$$

$$s_{22}^{rr} = \frac{1}{2}\left[(s_{22}^{xx} - s_{22}^{yy})e^{-j2\psi} - j(s_{22}^{yx} + s_{22}^{xy})e^{-j2\psi}\right] \tag{2.18}$$

$$s_{21}^{lr} = \frac{1}{2}\left[(s_{21}^{xx} - s_{21}^{yy})e^{+j2\psi} + j(s_{21}^{yx} + s_{21}^{xy})e^{+j2\psi}\right] \tag{2.19}$$

$$s_{21}^{ll} = \frac{1}{2}\left[(s_{21}^{xx} + s_{21}^{yy}) - j(s_{21}^{xy} - s_{21}^{yx})\right] \tag{2.20}$$

$$s_{22}^{ll} = \frac{1}{2}\left[(s_{22}^{xx} - s_{22}^{yy})e^{+j2\psi} + j(s_{22}^{yx} + s_{22}^{xy})e^{+j2\psi}\right] \tag{2.21}$$

$$s_{22}^{lr} = \frac{1}{2}\left[(s_{22}^{xx} + s_{22}^{yy}) - j(s_{22}^{xy} - s_{22}^{yx})\right] \tag{2.22}$$

It is seen from these equations that the circularly polarized scattering parameters are related with the linearly polarized ones and there are parameters unaffected from rotation.

In a transmitarray design, the minimization of the reflection is an important design consideration to increase the efficiency of the antenna. For an efficient transmitarray unit cell design, all the reflections should be minimized as,

$$s_{11}^{xx} = s_{11}^{yy} = s_{22}^{xx} = s_{22}^{yy} = s_{11}^{xy} = s_{11}^{yx} = s_{22}^{xy} = s_{22}^{yx} = 0 \qquad (2.23)$$

It is seen from the equations that for each sense of polarization, two transmission parameters exist i.e., when the structure is illuminated by a left-hand circularly polarized wave from port 1, both left and right-hand circularly polarized transmissions, $s_{21}^{ll}$ and $s_{21}^{rl}$, occur. The transmission with the same sense of polarization is unaffected from rotation and forms cross-pol radiation as observed from (2.20). To eliminate the scattered transmission fields independent of rotation to decrease the cross-pol radiation, following conditions should be satisfied in the design,

$$s_{mn}^{xx} = -s_{mn}^{yy} \qquad (2.24)$$

and

$$s_{mn}^{xy} = s_{mn}^{yx} \qquad (2.25)$$

for $m, n = 1,2 \ and \ m \neq n$.

Satisfying these, only four parameters are left; (2.10), (2.13), (2.16), and (2.19) and these parameters are rewritten below for convenience. Two of these parameters are advancing the transmitted phase twice the rotation angle (2.13) and (2.19) whereas (2.10) and (2.16) are delaying it. Also, the sense of the polarization changes for the transmitted wave.

$$s_{12}^{lr} = \frac{1}{2}\left[(s_{12}^{xx} - s_{12}^{yy})e^{-j2\psi} - j(s_{12}^{yx} + s_{12}^{xy})e^{-j2\psi}\right] \qquad (2.10)$$

$$s_{12}^{rl} = \frac{1}{2}\left[(s_{12}^{xx} - s_{12}^{yy})e^{+j2\psi} + j(s_{12}^{yx} + s_{12}^{xy})e^{+j2\psi}\right] \qquad (2.13)$$

$$s_{21}^{rl} = \frac{1}{2}\left[(s_{21}^{xx} - s_{21}^{yy})e^{-j2\psi} - j(s_{21}^{xy} + s_{21}^{yx})e^{-j2\psi}\right] \qquad (2.16)$$

$$s_{21}^{lr} = \frac{1}{2}\left[(s_{21}^{xx} - s_{21}^{yy})e^{+j2\psi} + j(s_{21}^{yx} + s_{21}^{xy})e^{+j2\psi}\right] \qquad (2.19)$$

(2.23) − (2.25) together with the maximization of transmission are the general conditions for applying the element rotation method in the transmitarrays. Although the implementation of (2.25) requires no phase difference between $s_{mn}^{xy}$ and $s_{mn}^{yx}$, minimizing these components also reduces the cross-pol radiation even there is phase difference between them. In the thesis, the circularly polarized transmission components with opposite sense of incident wave polarization and affected from rotation ($s_{12}^{lr}$, $s_{12}^{rl}$, $s_{21}^{lr}$, $s_{21}^{rl}$) are defined as co-pol components whereas the circularly polarized transmission components with same sense of incident wave polarization and unaffected from rotation ($s_{12}^{ll}$, $s_{12}^{rr}$, $s_{21}^{ll}$, $s_{21}^{rr}$) are defined as cross-pol components.

Further simplification is also possible for a double layer structure with identical layers. If we define, $s_{21}^{xx}$ and $s_{12}^{xx}$ as $T_x$; $s_{21}^{yy}$ and $s_{12}^{yy}$ as $T_y$; $s_{21}^{xy}$ and $s_{12}^{xy}$ as $T_{xy}$; $s_{21}^{yx}$ and $s_{12}^{yx}$ as $T_{yx}$ for such a structure; minimizing reflection, maximizing $T_x$ and $T_y$ and having 180° of phase difference between them when they have equal magnitude as implied by (2.24) and having 0° of phase difference between $T_{xy}$ and $T_{yx}$ when they have equal magnitude as implied by (2.25) or minimizing them are the sufficient conditions to design a transmitarray employing element rotation method.

# CHAPTER 3

# UNIT CELL DESIGNS

## 3.1.    Introduction

This chapter presents the transmitarray unit cells designed during this study. The designs are aimed to operate within X-band which is suitable for the measurements with WR-90 waveguide. The details of the design methodology used for the adjustment of the operating frequency and for providing the design conditions are presented in this chapter. The effect of each design parameter on the insertion loss level and the phase difference between the orthogonal polarized transmission coefficients are also explained in this chapter.

## 3.2.    Unit Cell Designs

In this thesis, CSRR and SRR type transmitarray unit cells are designed as they are appropriate for implementing the element rotation method with a microfluidics approach due to their circular structure. An SRR is a structure in the form of conductive rings on which splits take place as openings whereas a CSRR is in the form of ring slots and split is the conductive region on the slots. Due to the circular symmetry of these structures rotation of the split around the ring or ring slot realizes the rotation of the structure around its surface normal. To implement the microfluidics approach, the rings and the ring slots are realized as channels etched in PDMS and conductive

23

regions and splits are formed by injecting a liquid metal. The split region is the air gap for SRR structures whereas it is the injected liquid metal for CSRRs. The structures are designed with Ansys HFSS® by using the infinite array approach. This approach is implemented by forming periodic boundaries by imposing master and slave boundaries on the side walls of the unit cell. One pair of the master and slave boundaries are shown in dashed planes in Figure 3.1. These boundaries are constructed on the planes defined by **u** and **v** vectors. To characterize the incident and transmitted fields, Floquet ports are defined at the apertures by **a** and **b** lattice vectors which also define the geometry and periodicity of the unit cell. At the Floquet ports the incident and scattered wave modes are interrelated with the S-matrix by which the related reflection and transmission characteristics can be examined. These S-matrices can be modified and moved to a reference plane by deembedding and the surfaces of the unit cells are taken as the reference planes for the structures in this thesis.



(a)                                    (b)
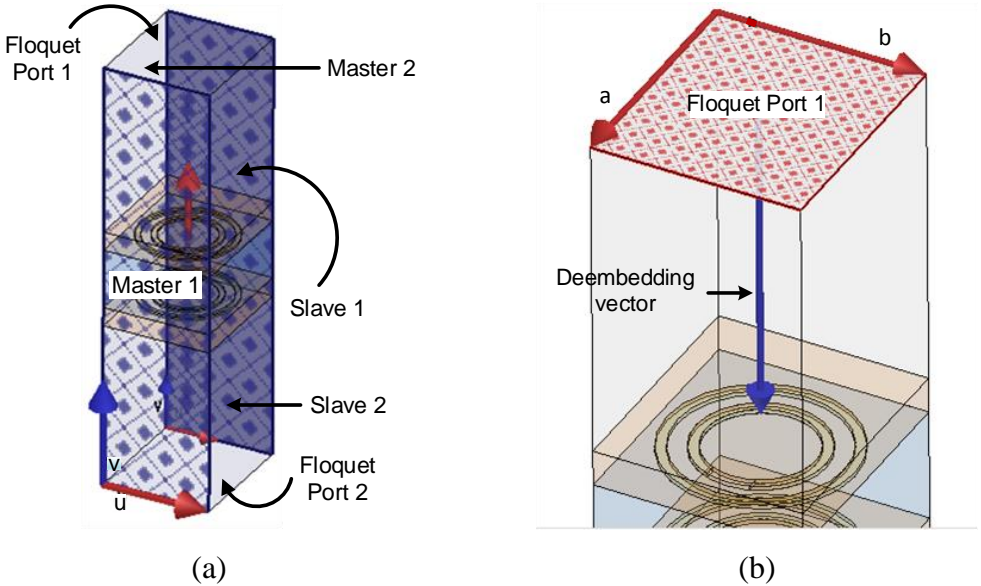
Figure 3.1      (a) Illustration of the formation of the periodic boundaries with master and slave boundaries in Ansys HFSS®. (b) Definition of one of the Floquet ports by **a** and **b** lattice vectors and the deembedding vector moving the reference plane.

24
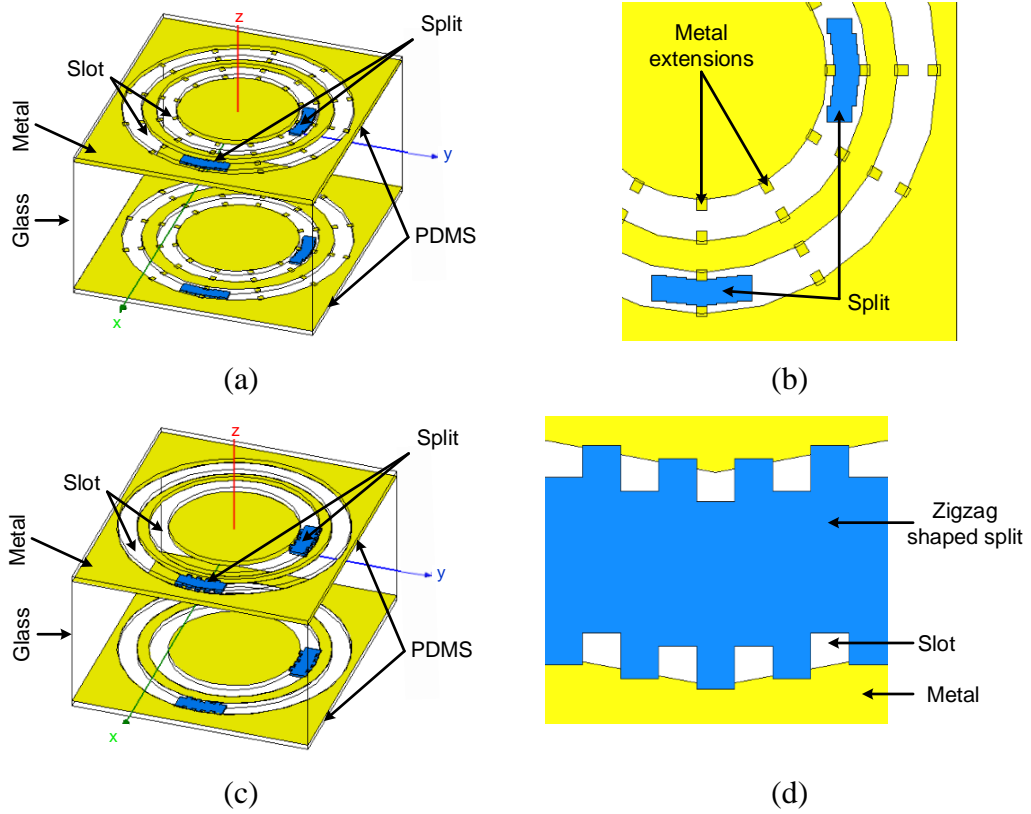
Figure 3.2     Illustrations of the CSRR transmitarray unit cells. (a) The unit cell with metal extensions, (b) close up view of the metal extensions, (c) the unit cell with zigzag type channels, (d) close up view of the zigzag type channels.

Figure 3.2 shows the CSRR unit cells. Two different unit cells with respect to the channel type are designed. The reason in forming two different types arises from the adhesion property of the PDMS. As PDMS shows more effective adhesion to the glass surfaces than metal, to decrease the possibility of leakage of the liquid metal, the structures are designed to increase the contact area between the glass and the PDMS. In the first structure, the channels of 0.5 mm width are within the 0.8 mm-width slots and periodic metal extensions separated by 30° and having 200 μm width are patterned to provide a contact between the liquid metal and the antenna metal [62], [63]. A zigzag-shaped channel is formed for the same purpose in the second CSRR structure

shown in Figure 3.2 (c). For the same radial direction, one end of the channel is bonded to the glass layer and the other end is bonded to the metal layer. By this way, the connection of the liquid metal to the antenna metal is provided and the contact area of the glass and the PDMS is increased by bonding one end of the channels to the glass.
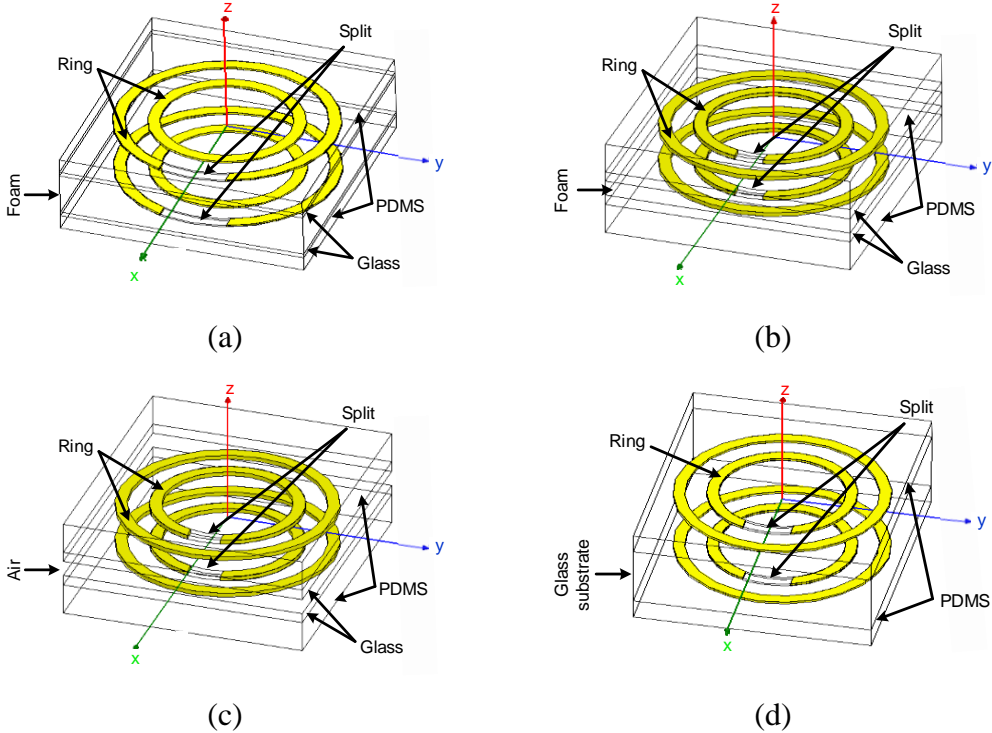


Figure 3.3    Illustrations of the SRR transmitarray unit cells. (a) The OS-SRR transmitarray unit cell, (b) the IS-SRR transmitarray unit cell with foam substrate between the layers, (c) the IS-SRR transmitarray unit cell with air gap between the layers, (d) the IS-SRR transmitarray unit cell with glass substrate.

Figure 3.3 shows the SRR type unit cells. In these structures the PDMS layer is directly bonded to the glass layer. Two types of unit cells with respect to the split positioning are designed. The split takes place on the outer ring for the structure in Figure 3.3 (a),

the outer ring split SRR (OS-SRR), and it takes place on the inner ring for the other structures, inner ring split SRR (IS-SRR), in the figure. The other ring is full of liquid metal for both types. A foam is placed between the layers for the OS-SRR whereas air gap, foam and glass are used for the IS-SRR. Due to the better insertion loss characteristics of the IS-SRR structure as will be explained in Chapter 4, different substrate types appropriate both in fabrication and measurement are used for optimizing the unit cell. The SRR type structures are advantageous over the CSRR structures in terms of fabrication simplicity since they include less steps due to the lack of the metal layer and more importantly, PDMS adhesion is better as PDMS is directly bonded to the glass layer. The design methodology to satisfy the phase shifting conditions are common in all structures and it is presented in next section.

The designs are double layer structures where each layer consists of nested rings. The rings are formed as a microfluidic channel inside the PDMS layer ($\varepsilon_r = 2.77$, *tan $\delta$* = 0.0127). These values are verified by the measurements presented in Section 5.3.2. The injected liquid metal in the channels forms the conductive parts in the structures. The liquid metal used is an alloy of 68.5% Ga, 21.5% In, and 10% Sn, ($\sigma = 3.46 \times 10^6$ Siemens/m), a product of GalliumSource, LLC [64]. The split region is the empty region in the channel filled with the liquid metal in SRR type structures whereas it is formed by the liquid metal in CSRR type structures. In the design of the unit cells, the depth of the rings (channels) is taken as 0.2 mm. The dimensions of the unit cell are 11.43 mm × 10.16 mm, approximately $0.38\lambda_0$ at 10 GHz. Since the waveguide simulator method [65] is used for the characterization of the fabricated unit cells, this dimension is chosen to ensure that two adjacent unit cells strictly fits into the WR-90 waveguide which has dimensions of 22.86 mm × 10.16 mm. The design conditions are satisfied for all of the structures; parameters and the related characteristics of the designs are given in the Appendix. Although several types of unit cells are designed to implement the element rotation method with a microfluidics approach, IS-SRR structure is preferred since it is more suitable for the implementation of this approach as the reasons will be explained in this chapter.

### 3.2.1. Design Methodology

The definitions for $T_x$, $T_y$, $T_{xy}$, and $T_{yx}$ presented in Chapter 2 are appropriate for the structures as the structures are double layer with identical layers. That is, the co-pol transmission coefficients for $x$- and $y$-polarized waves are $T_x$ and $T_y$ whereas the cross-pol transmission coefficients are $T_{xy}$ and $T_{yx}$ where the first subscript in these coefficients stands for the polarization of the transmitted wave and the second subscript is that of the incident wave.

The design methodology mainly depends on the change of the characteristic impedance of the unit cell to satisfy the phase shifting conditions derived in the previous chapter. These conditions are;

- 180° of phase difference between the transmission components ($T_x$ and $T_y$) and maximizing these components when they have equal magnitude (i.e., $T_x = -T_y$),

- 0° of phase difference between $T_{xy}$ and $T_{yx}$ or minimizing them when they have equal magnitude to decrease the cross-pol radiation,

- Minimizing reflection.

The operating frequency of the design is the frequency where $T_x$ and $T_y$ have equal magnitude. In order to have a phase difference between $T_x$ and $T_y$, to satisfy the first condition, the resonance frequencies of the structure for each orthogonal polarized propagating wave should be different. This can be achieved by making the characteristic impedance of the structure different for those propagations. The difference in the impedance results in having different resonance frequencies for the orthogonal wave modes. Splits are placed on the rings to obtain a difference in the characteristic impedance for the orthogonal polarized wave modes. Characteristic

impedance of the structure is also important in reducing the reflection losses which can be accomplished by matching the impedance of the unit cell to free space [66]. Therefore, to design a transmitarray unit cell implementing the element rotation method it is important to figure out the changes in the characteristic impedance of the structure. The characteristic impedance of an SRR can be modeled as an L-C circuit [67]-[69]. The capacitance is formed between the conductive rings and around the split whereas the inductance is formed from the rings itself and the distance between the inner and outer rings [68]. The inductance can be approximated as that of a single ring with averaged radius of midpoint between the nested rings and width of a single ring and the CSRR model is the dual of the SRR model [67].

To satisfy the aforementioned phase shifting conditions, parametric analysis is carried out where the radii of the rings, substrate thickness, PDMS thickness, ring width and split length are the design parameters. These parameters are shown in Figure 3.4 for IS-SRR with glass substrate. The effect of these parameters on the design constraints and the transmission magnitude will be presented in the next section.



(a)                                    (b)
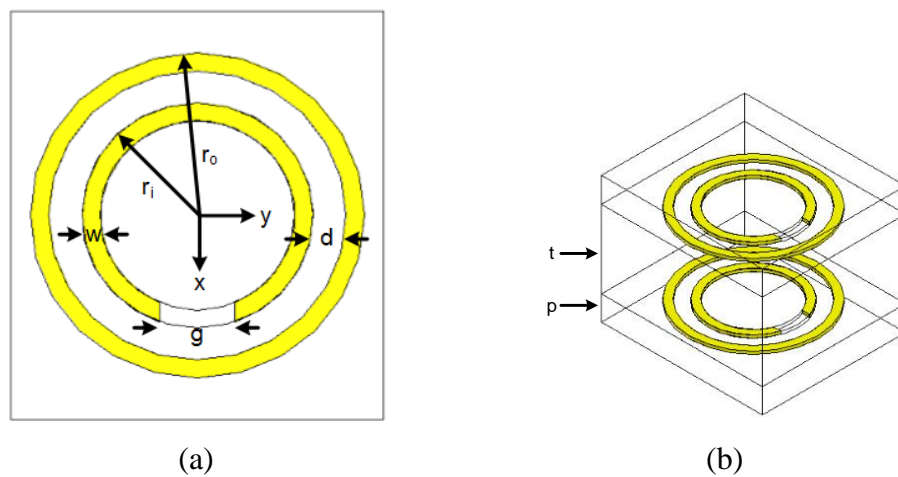
Figure 3.4     Physical design parameters of the double layer nested split ring transmitarray unit cell.

The design is optimized for the parameter values in Table 3.1 such that the magnitudes of $T_x$ and $T_y$ are equalized and the phase difference between them is 180° at 8.8 GHz as shown in Figure 3.5 (a) and (b). Figure 3.6 (a) shows that the magnitudes of $T_{xy}$ and $T_{yx}$ are equal and below −55 dB at that frequency. Figure 3.6 (b) shows the reflection coefficient characteristics of the structure.
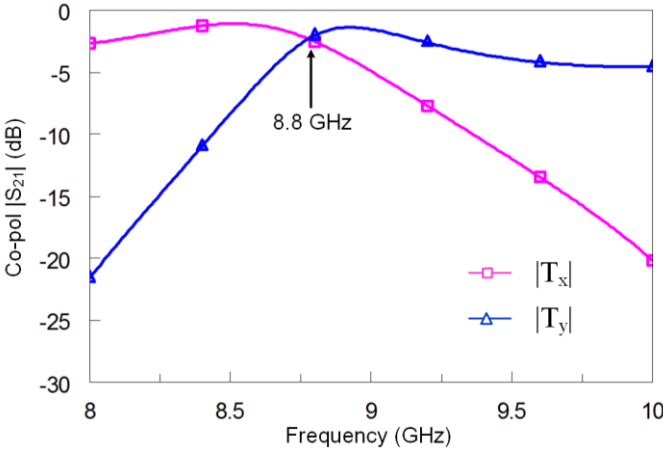


(a)
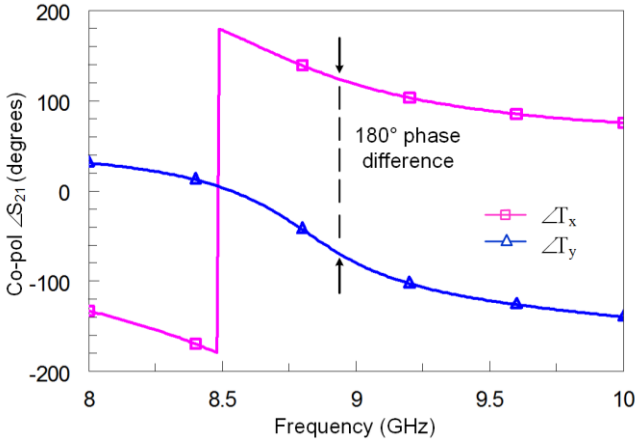


(b)

Figure 3.5    Simulated characteristics of the IS-SRR transmitarray unit cell with glass substrate. (a) Magnitude of the co-pol transmission coefficients, (b) phase of the co-pol transmission coefficients.

30
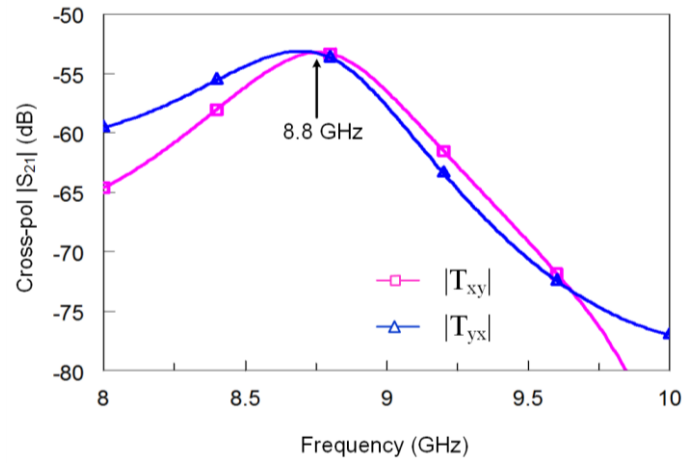
(a)
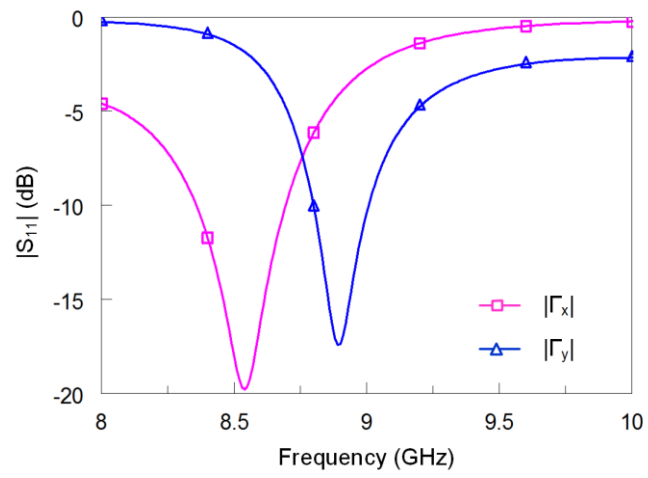


(b)

Figure 3.6     Simulated characteristics of the IS-SRR transmitarray unit cell with glass substrate. (a) Magnitude of the cross-pol transmission coefficients, (b) magnitude of the reflection coefficients.

Table 3.1      The values of the parameters of the IS-SRR transmitarray unit cell
with glass substrate.

| Substrate thickness ($t$) | Split length ($g$) | Outer ring radius ($r_o$) | Inner ring radius ($r_i$) | Ring width ($w$) | PDMS thickness ($p$) |
|---|---|---|---|---|---|
| 5.5 mm | 2.05 mm | 4.55 mm | 3.15 mm | 0.5 mm | 1.75 mm |

The same methodology is also applied to the other structures and the related parameter values and characteristics are in the Appendix as mentioned before. As it can be seen from these figures in the Appendix, the intersection of $T_{xy}$ and $T_{yx}$ are approximately at $-15$ dB for CSRR unit cells. Since these characteristics are worse than that of the SRR unit cells and considering the previously mentioned fabrication difficulties, SRR designs are deduced to be better choices for the implementation of the element rotation method. Also, as will be explained in the next chapter, IS-SRR has a better insertion loss value and the variation of the insertion loss with respect to the rotation angle is less than those of the OS-SRR. In addition, the insertion loss value of the IS-SRR unit cell with glass substrate is lower than same type of unit cells with foam substrate or air gap between the layers. Therefore, as the IS-SRR structure with glass substrate is more suitable for the implementation of the element rotation method by microfluidics, this structure is fabricated, measured and the related results also take place in [70], [71].

### 3.2.1.1.   Parametric Analysis

The parameters introduced in Figure 3.4 have effect on the phase difference, operating frequency, and the transmission magnitude. In this section, these effects are discussed by presenting the results of a parametric analysis carried out for the IS-SRR structure. The main difficulty in designing a transmitarray unit cell implementing the element

rotation method is tuning the phase difference between $T_y$ and $T_x$. This difference is based on the change in the frequency difference between the resonances. Therefore, to tune the phase difference, the resonance frequencies of each orthogonal polarized wave should be affected differently from the changes in the parameters. This difference in the shift of the resonance frequencies also affect the transmission magnitude and the operating frequency. Once these effects are determined, it is possible to choose the appropriate parameters to satisfy the conditions. Therefore, explaining the effect of each parameter on the reflection and transmission coefficients is essential in a transmitarray unit cell design implementing the element rotation method.

### 3.2.1.1.1. The Split Length

The change in the operating frequency, intersection magnitude of $T_y$ and $T_x$ and the phase difference between $T_y$ and $T_x$ with respect to the change in the split length, $g$, is presented in Table 3.2. The values of the parameters kept constant during this analysis are given in Table 3.3. It can be deduced from Table 3.2 that the operating frequency increases with the increment in the split length. The increment in the split length decreases the capacitance around the split and the capacitance between the rings by decreasing the conductive area between the rings, which increases the resonance frequency. The effect of the change in the split length can be observed more clearly from Figure 3.7 which shows the magnitude of $T_x$ and $T_y$ with respect to frequency for the split length values of 1.05 mm and 2.55 mm. It is observed from the figure that the operating frequency and the intersection magnitude of $T_x$ and $T_y$ increases with the increment in the split length. As the split length increases, the resonance frequencies and the maxima of the transmission coefficients approach each other by which, they intersect at a higher transmission magnitude. This behavior can also be observed in Figure 3.8 where the reflection and transmission coefficient characteristics of the orthogonal polarized waves are shown for each split length value, g = 1.05, 1.8, and 2.55 mm, separately.

Table 3.2    The parametric analysis of the IS-SRR transmitarray unit cell with respect to the split length.

| Split Length | $T_x$ and $T_y$ intersection frequency | $T_x$ and $T_y$ intersection magnitude | $\angle T_y - \angle T_x$ at intersection |
|---|---|---|---|
| 1.05 mm | 8.47 GHz | −3.12 dB | 194 |
| 1.3 mm | 8.55 GHz | −2.92 dB | 192 |
| 1.55 mm | 8.63 GHz | −2.74 dB | 189 |
| 1.8 mm | 8.7 GHz | −2.51 dB | 185 |
| 2.05 mm | 8.8 GHz | −2.2 dB | 180 |
| 2.3 mm | 8.86 GHz | −1.95 dB | 172 |
| 2.55 mm | 8.95 GHz | −1.68 dB | 161 |
| 2.8 mm | 9.03 GHz | −1.45 dB | 150 |
| 3.05 mm | 9.13 GHz | −1.38 dB | 138 |
| 3.3 mm | 9.39 GHz | −2.42 dB | 126 |

Table 3.3    The constant parameters for the split length analysis.

| Outer ring radius ($r_o$) | Inner ring radius ($r_i$) | Ring width ($w$) | Substrate thickness ($t$) | PDMS thickness ($p$) | Distance between rings ($d$) |
|---|---|---|---|---|---|
| 4.55 mm | 3.15 mm | 0.5 mm | 5.5 mm | 1.75 mm | 0.9 mm |
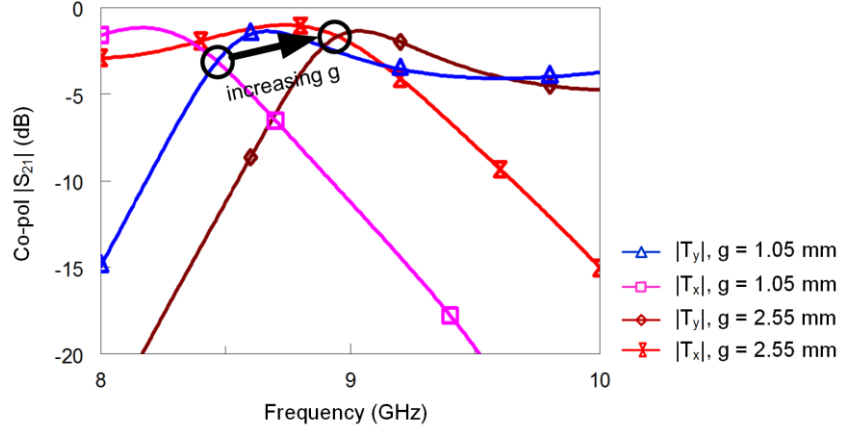
Figure 3.7     Transmission coefficient characteristics of the unit cell with respect to the change in the split length.

It is also deduced from Table 3.2 that, as the split length increases the phase difference between $T_y$ and $T_x$ decreases, which indicates that the change in the split length affects the characteristics for $x$- and $y$- polarized wave modes differently. When the reflection coefficient characteristics for both polarizations is examined in Figure 3.9, it is seen that the resonance frequency for $\Gamma_x$ is influenced more than that for $\Gamma_y$ by the change in the split length. This situation can be explained by analyzing the reflection coefficient characteristics of the IS-SRR transmitarray unit cell and the same unit cell without the inner ring. The schematics and the related reflection coefficient characteristics are shown in Figure 3.10. The values of the parameters in the analysis are; $t = 5.5$ mm, $g = 2.05$ mm, $r_o = 4.55$ mm, $r_i = 3.15$ mm, $p = 1.75$ mm. From the characteristics in Figure 3.10 (c) and (d), it is observed that, the outer ring is more effective on the resonant frequency in the examined frequency range for $\Gamma_y$. Therefore, as the split does not exist on the outer ring, the change in the split length does not change the resonance frequency for $\Gamma_y$ as for $\Gamma_x$. This difference in the change of the resonance frequencies affects the amount of phase difference between the orthogonal polarized transmission coefficients. As the resonance frequencies for $\Gamma_x$ and $\Gamma_y$ approach each other by changing the split length, the phase difference decreases.

35
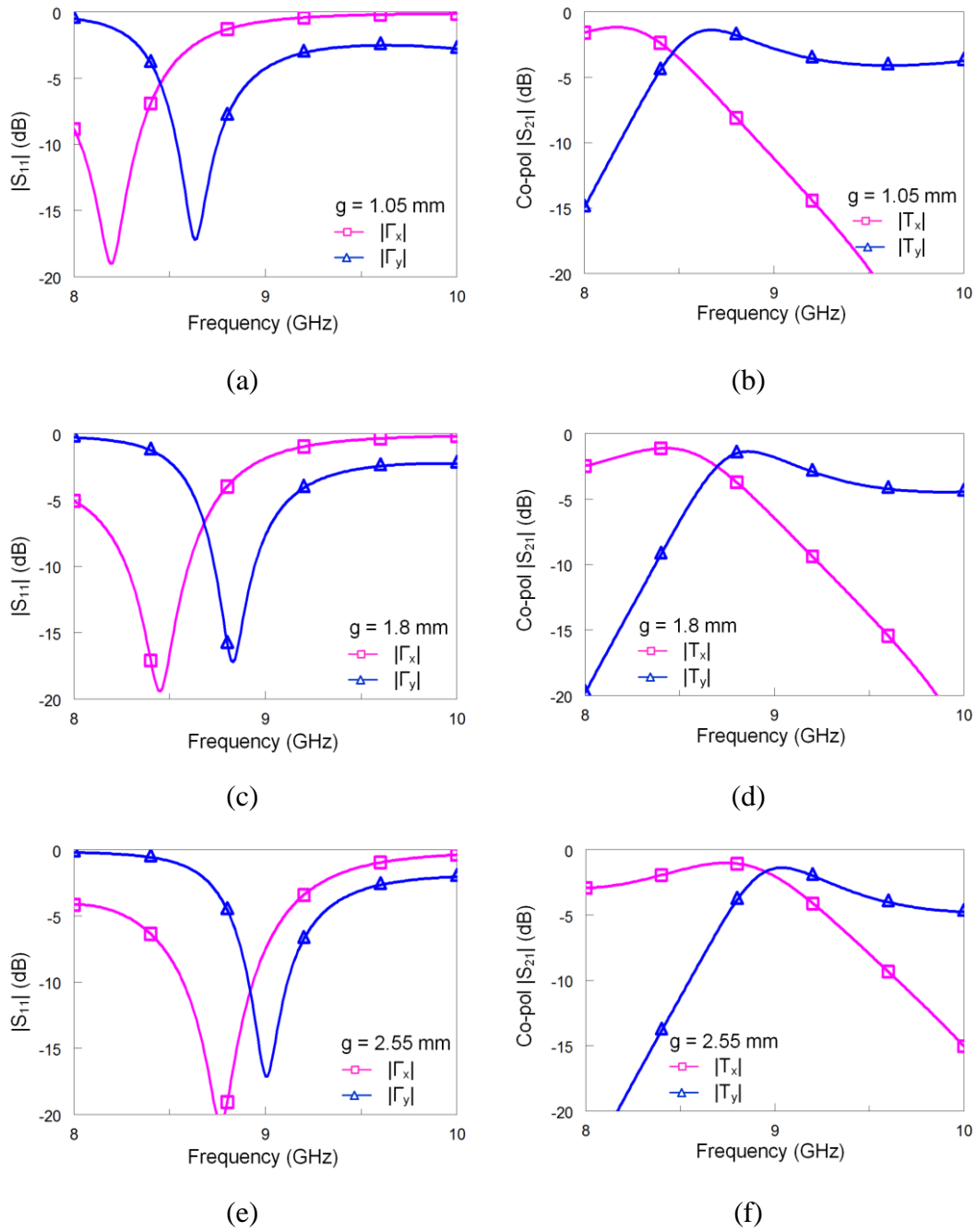
Figure 3.8    Reflection and co-pol transmission coefficient characteristics of the unit cell for the split length of (a) – (b) 3 mm, (c) – (d) 4.5 mm, (e) - (f) 6 mm.
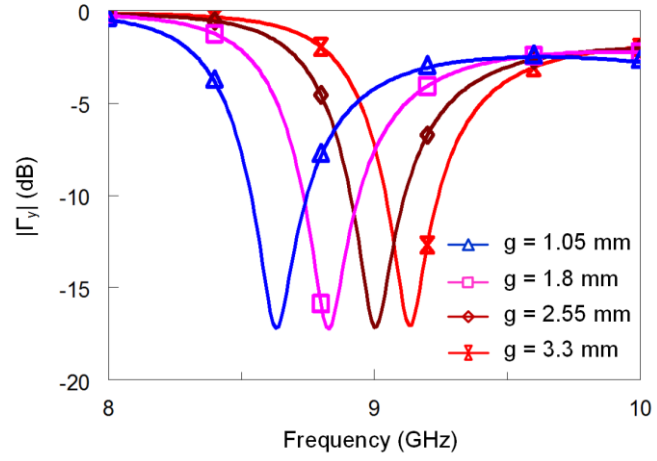
(a)
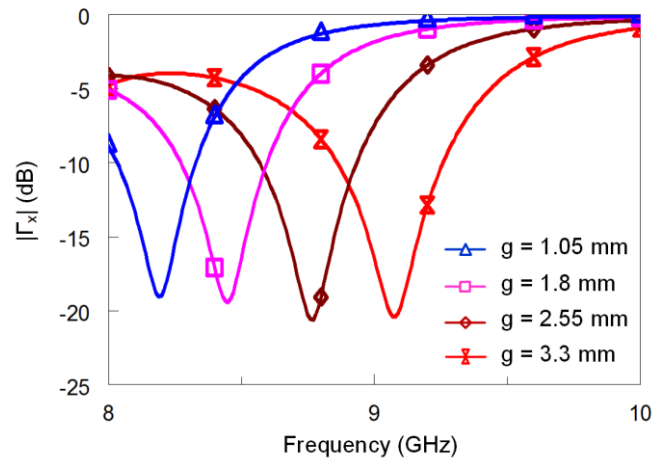


(b)

Figure 3.9     Reflection coefficient characteristics of the unit cell with respect to the change in the split length. (a) $\Gamma_y$, (b) $\Gamma_x$.

(a)

(b)

(c)

(d)
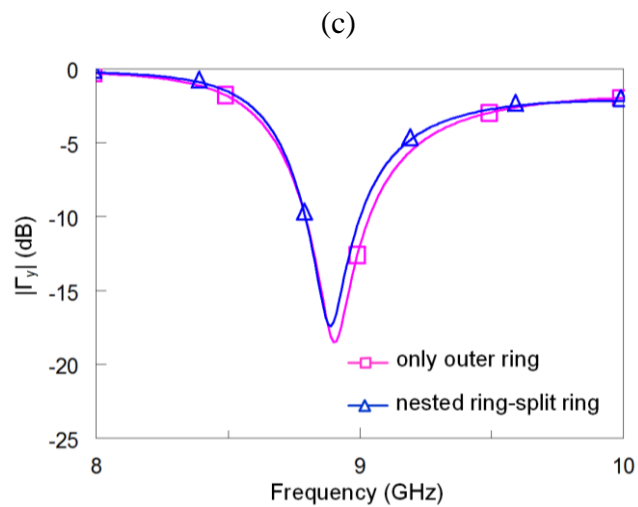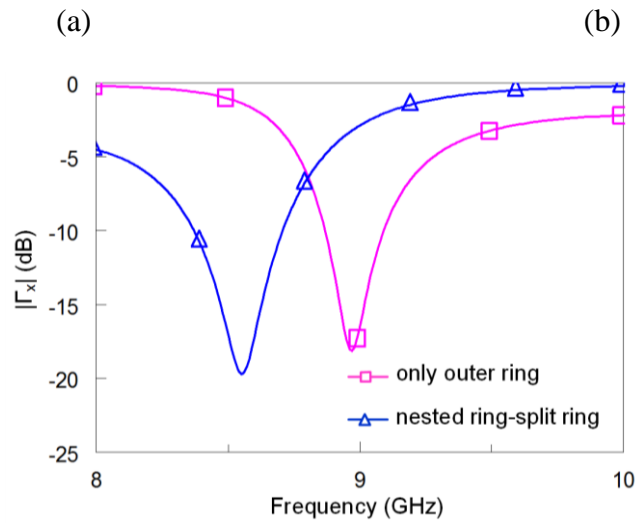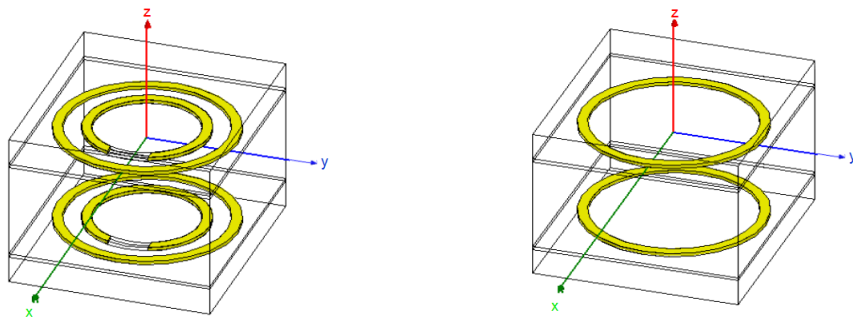
Figure 3.10    Geometry of the unit cells and their reflection coefficients characteristics. (a) IS-SRR structure, (b) double layer outer ring structure, (c) $\Gamma_x$, (d) $\Gamma_y$.

### 3.2.1.1.2. The Glass Substrate Thickness

Table 3.4 shows the values of the operating frequency, magnitude of $T_y$ and $T_x$ at the operating frequency and the phase difference between $T_y$ and $T_x$ with respect to the change in the substrate thickness, $t$. During this analysis, the values of the other parameters are kept constant as given in Table 3.5. The intersection frequency of $T_x$ and $T_y$ decreases as the substrate thickness increases. This is because of the increment in the capacitance formed due to the edge coupling between the inner ring and the outer ring [72]. It is also observed from the table that the phase difference between $T_y$ and $T_x$ at the operating frequency decreases and the corresponding magnitude of the transmission coefficients increases as the substrate thickness increases. Similar to the analysis for split length, in Section 3.2.1.1.1, as the substrate thickness increases, the resonance frequencies and the maxima of the transmission coefficients approach each other by which, they intersect at a higher magnitude, which is shown in Figure 3.11 for $t = 3$, 4.5, and 6 mm.

Table 3.4     The parametric analysis of the IS-SRR transmitarray unit cell with respect to the glass substrate thickness.

| Substrate Thickness | $T_x$ and $T_y$ intersection frequency | $T_x$ and $T_y$ intersection magnitude | $\angle T_y - \angle T_x$ at intersection |
|---|---|---|---|
| 3 mm | 9.32 GHz | −7.04 dB | 225 |
| 3.5 mm | 9.26 GHz | −6.17 dB | 222 |
| 4 mm | 9.17 GHz | −5.3 dB | 218 |
| 4.5 mm | 9.06 GHz | −4.14 dB | 208 |
| 5 mm | 8.94 GHz | −3.12 dB | 195 |
| 5.5 mm | 8.8 GHz | −2.2 dB | 180 |
| 6 mm | 8.66 GHz | −1.74 dB | 147 |

(a)

(b)

(c)

(d)

(e)

(f)
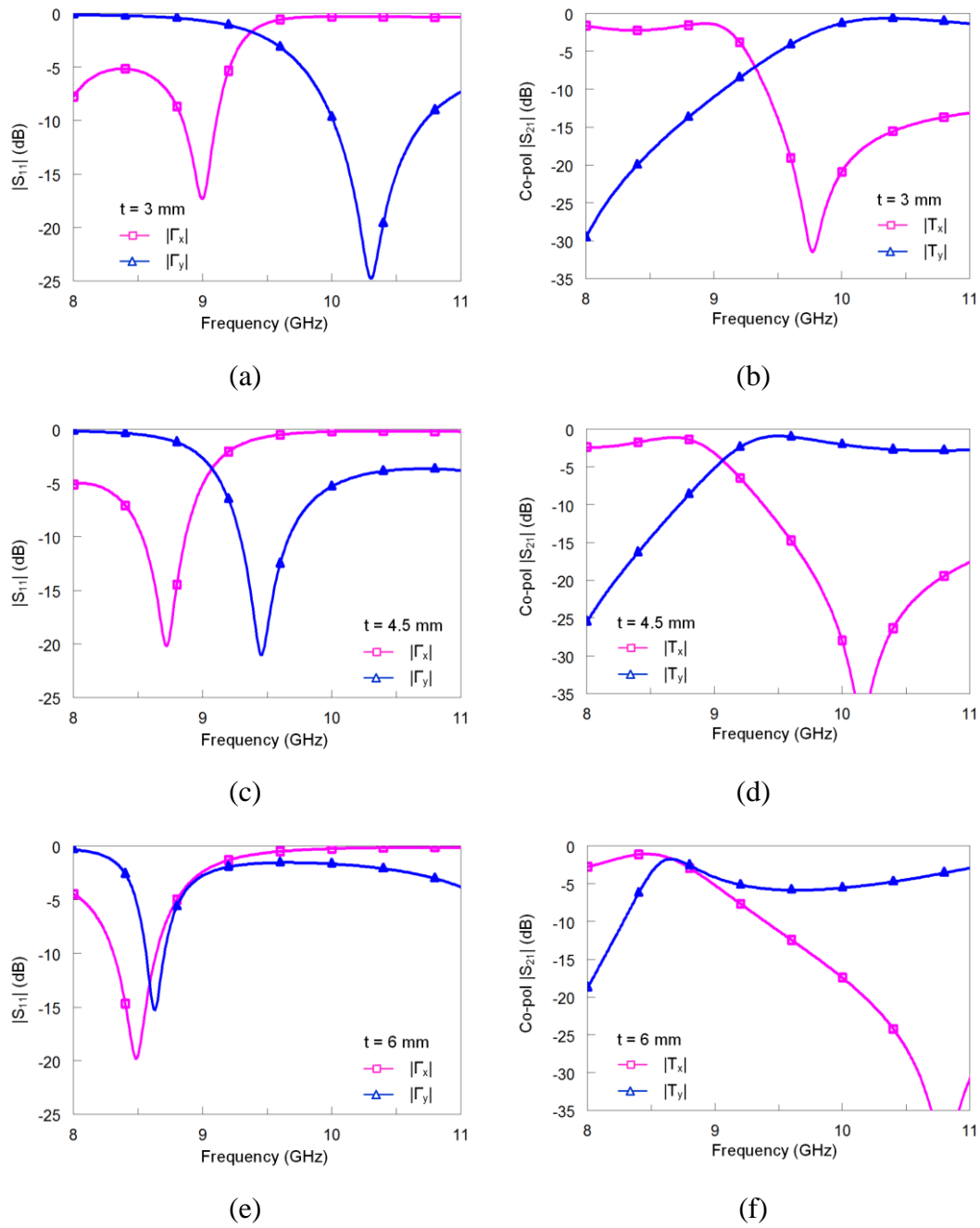
Figure 3.11    Reflection and co-pol transmission coefficient characteristics of the unit cell for the substrate thicknesses of (a) – (b) 3 mm, (c) – (d) 4.5 mm, (e) - (f) 6 mm.

Table 3.5    The constant parameters for the parametric analysis for glass substrate thickness.

| Outer ring radius ($r_o$) | Inner ring radius ($r_i$) | Ring width ($w$) | Split length ($g$) | PDMS thickness ($p$) | Distance between rings ($d$) |
|---|---|---|---|---|---|
| 4.55 mm | 3.15 mm | 0.5 mm | 2.05 mm | 1.75 mm | 0.9 mm |

Figure 3.12 shows the magnitude of $T_x$ and $T_y$ with respect to frequency for the substrate thicknesses of 3 mm and 5 mm, which indicates the changing trend of the operating frequency and the transmission magnitude. The operating frequency decreases and the magnitude of the transmission coefficients at the operating frequency increases due to the aforementioned reasons in this section.
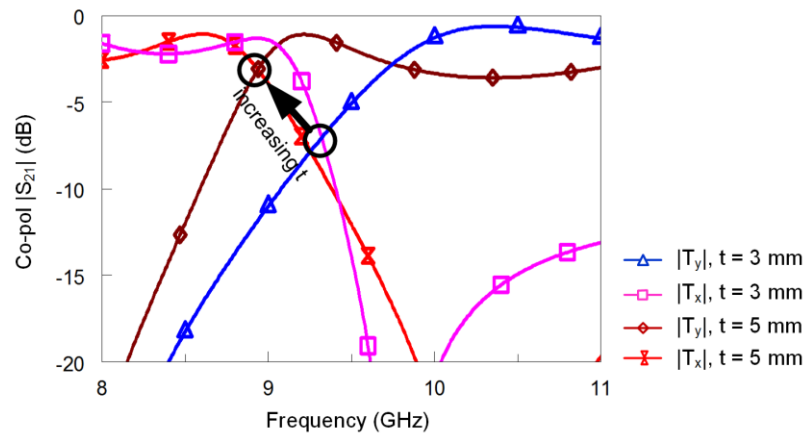


Figure 3.12    Transmission coefficient characteristics of the unit cell with respect to the change in the glass substrate thickness.

When the reflection coefficient characteristics of $\Gamma_x$ and $\Gamma_y$ are examined in Figure 3.13, it is seen that the decrease in the resonance frequency for $\Gamma_y$ is more than that for $\Gamma_x$, resulting in a decrease in the phase difference.
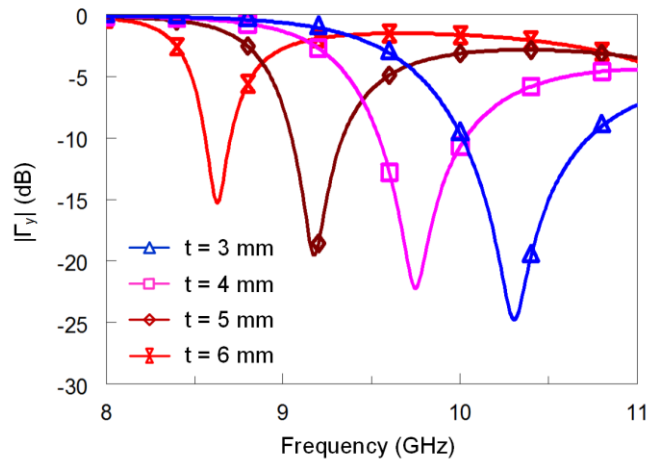


(a)
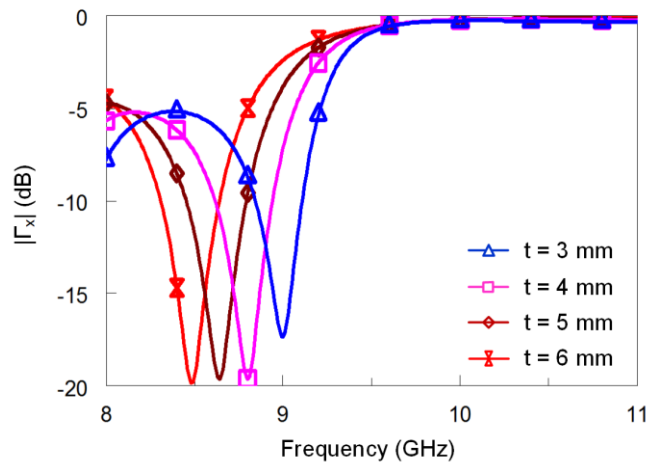


(b)

Figure 3.13 Reflection coefficient characteristics of the unit cell with respect to the change in the glass substrate thickness. (a) $\Gamma_y$, (b) $\Gamma_x$.

The reason of the difference in the change of the resonance frequencies for $\Gamma_x$ and $\Gamma_y$ can be understood better from the surface current, $J_s$ analysis shown in Figure 3.14. For $t = 3$ mm, it can be inferred from Figure 3.14 (a) that, $y$-polarized excitation induces more current on the outer ring at the resonance frequency, 10.3 GHz. As the substrate thickness increases to 6 mm, the distribution in Figure 3.14 (b) indicates that the coupling between the rings is enhanced, which increases the aforementioned capacitance due to the coupling. For $x$-polarized excitation in Figure 3.14 (c) and (d), although the coupling increases, there is no significant change in the distribution as for the $y$-polarized excitation.



(a)  (b)

(c)  (d)
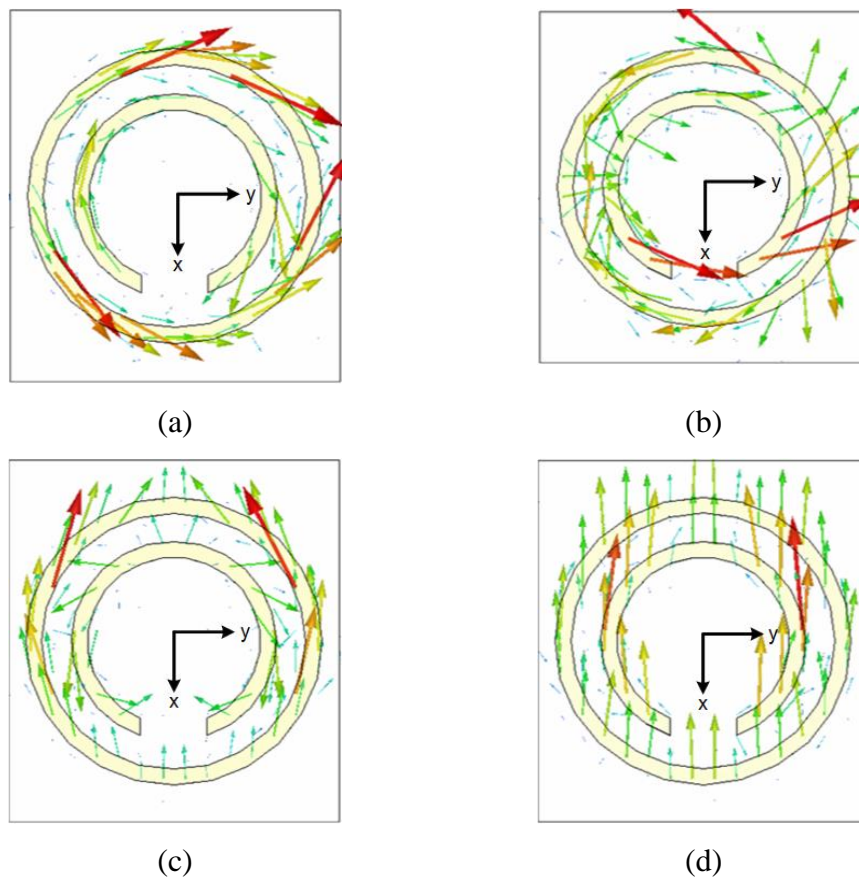
Figure 3.14    Electric surface current density distributions for the unit cell. a) For $y$-polarized wave at t = 3 mm, at 10.3 GHz. b) For $y$-polarized wave at t = 6 mm, at 8.64 GHz. c) For $x$-polarized wave at t = 3 mm, at 9 GHz. d) For $x$-polarized wave at t = 6 mm, at 8.48 GHz.

### 3.2.1.1.3. The Ring Width

Table 3.6 shows the values of the intersection frequency of $T_y$ and $T_x$, corresponding transmission magnitude and the phase difference between $T_y$ and $T_x$ when the ring width, $w$, is changed. At each step, the width of the rings is changed in two directions; out of the ring and towards the center of the ring. Therefore, the change in the ring width also changes the values of other parameters such as, the values of outer ring radius, $r_o$, inner ring radius, $r_i$, and the distance between the rings, $d$. Figure 3.15 shows the magnitude of $T_x$ and $T_y$ with respect to frequency for the ring width of 0.5 mm and 1.1 mm. It can be concluded from the plot and Table 3.6 that the increment in the ring width increases the intersection frequency of $T_y$ and $T_x$ whereas it decreases the magnitude of $T_y$ and $T_x$ at the intersection frequency. Table 3.7 shows the parameters that are kept constant during this analysis.

Table 3.6      The parametric analysis of the IS-SRR transmitarray unit cell with respect to the ring width.

| Ring width | $T_x$ and $T_y$ intersection frequency | $T_x$ and $T_y$ intersection magnitude | $\angle T_y - \angle T_x$ at intersection |
|---|---|---|---|
| 0.5 mm | 8.8 GHz | −2.2 dB | 180 |
| 0.7 mm | 8.9 GHz | −4.37 dB | 220 |
| 0.9 mm | 9 GHz | −7.6 dB | 255 |
| 1.1 mm | 9.1 GHz | −11.56 dB | 278 |

Table 3.7        The constant parameters for the ring width analysis.

| Substrate thickness ($t$) | Split length ($g$) | PDMS thickness ($p$) |
|---|---|---|
| 5.5 mm | 2.05 mm | 1.75 mm |
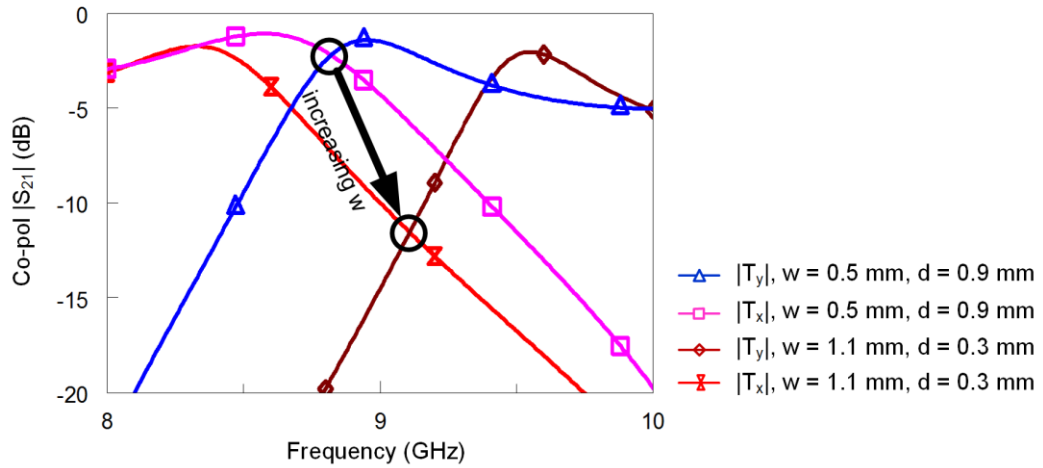


Figure 3.15     Transmission coefficient characteristics of the unit cell with respect to the change in the ring width.

It is also deduced from the table that the phase difference between $T_y$ and $T_x$ increases with the increment in the ring width, which indicates that the resonance frequencies of the orthogonal polarized waves move apart from each other. This movement is also the reason of the decrease in the magnitude of $T_y$ and $T_x$ at their intersection. The reflection coefficient characteristics for both polarizations in Figure 3.16 shows that the resonance frequency increases for $\Gamma_y$ whereas it decreases for $\Gamma_x$. It is known that, the increment in the ring width value decreases the mutual inductance between the rings whereas the decrement in the distance between the rings increases the mutual inductance and capacitance values [68]. Since the outer ring determines the resonance

for *y*-polarization, the structure can be treated as a single loop of width, *w*, and the increment in the ring width decreases the inductance value resulting in an increase in the resonance frequency. For the *x*-polarization, the decrease in *d* value is more effective on the resonances, that is, the resonance frequency decreases due to the increment in the mutual inductance and capacitance between the rings.
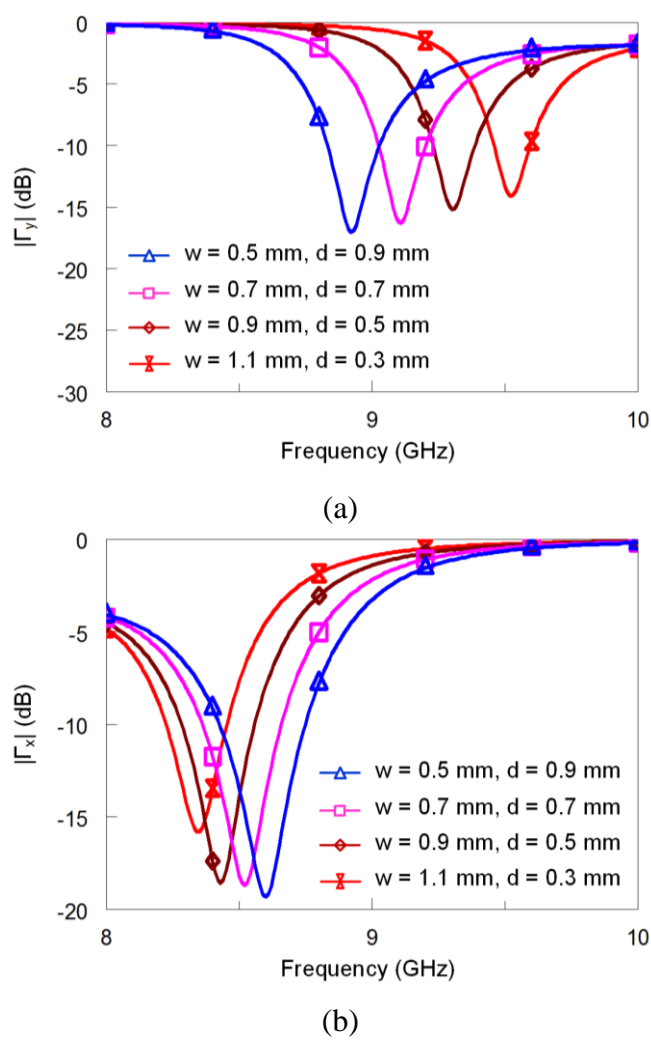


Figure 3.16    Reflection coefficient characteristics of the unit cell with respect to the change in the ring width. (a) $\Gamma_y$, (b) $\Gamma_x$.

### 3.2.1.1.4. The Radius of the Outer Ring

Table 3.8 shows the values of the intersection frequency, corresponding transmission magnitude and the phase difference between $T_y$ and $T_x$ when the radius of the outer ring, $r_o$, is changed whereas Table 3.9 shows the parameters that are kept constant during this analysis.

The change in $r_o$ also changes the distance between the rings, $d$. Increasing the radius of the outer ring decreases the intersection frequency of $T_y$ and $T_x$. The decrease in the phase difference and the increase in the magnitude of $T_y$ and $T_x$ at intersection are due to the change in the difference of the resonance frequencies for the $x$- and $y$-polarized wave modes as in the previous cases. Since the outer ring is more effective on $y$-polarized wave mode, the change in the dimension of the outer ring affects $\Gamma_y$, more than $\Gamma_x$. Figure 3.17 shows the related reflection coefficient characteristics whereas Figure 3.18 shows the change of the magnitude of $T_x$ and $T_y$ for $r_o$ at 3.8 mm and 4.8 mm.

Table 3.8    The parametric analysis of the IS-SRR transmitarray unit cell with respect to the radius of the outer ring.

| Outer radius | $T_x$ and $T_y$ intersection frequency | $T_x$ and $T_y$ intersection magnitude | $\angle T_y - \angle T_x$ at intersection |
|---|---|---|---|
| 3.8 mm | 9.85 GHz | $-22$ dB | 270 |
| 4.05 mm | 9.41 GHz | $-9.49$ dB | 255 |
| 4.3 mm | 9.09 GHz | $-4.78$ dB | 220 |
| 4.55 mm | 8.8 GHz | $-2.2$ dB | 180 |
| 4.8 mm | 8.58 GHz | $-1.13$ dB | 139 |

Table 3.9    The constant parameters for the radius of the outer ring analysis.

| Inner ring radius ($r_i$) | Substrate thickness ($t$) | Split length ($g$) | PDMS thickness ($p$) | Ring width ($w$) |
|---|---|---|---|---|
| 3.15 mm | 5.5 mm | 2.05 mm | 1.75 mm | 0.5 mm |
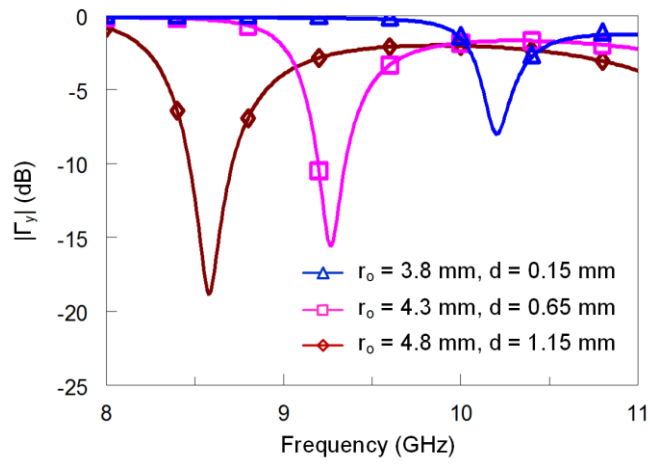


(a)
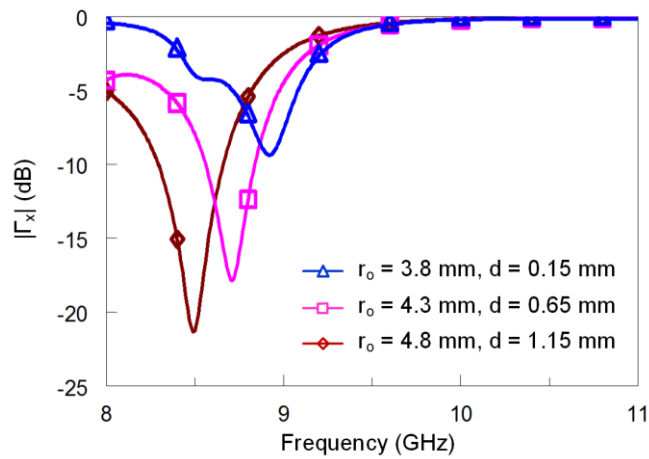


(b)

Figure 3.17    Reflection coefficient characteristics of the unit cell with respect to the change in the radius of the outer ring. (a) $\Gamma_y$, (b) $\Gamma_x$.
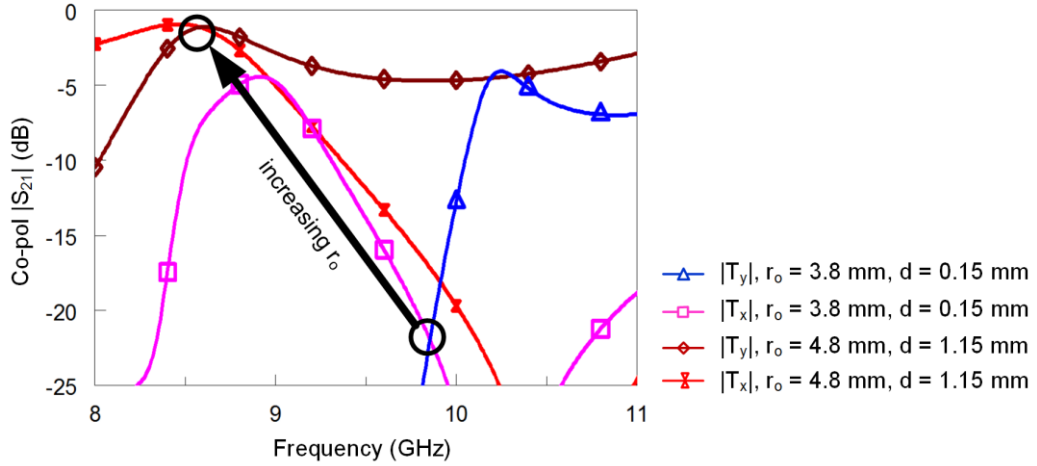
Figure 3.18    Transmission coefficient characteristics of the unit cell with respect to the change in the radius of the outer ring.

### 3.2.1.1.5. The Radius of the Inner Ring

Table 3.10 shows the values of the intersection frequency, corresponding transmission magnitude and the phase difference between $T_y$ and $T_x$ when the radius of the inner ring, $r_i$, is changed. Table 3.11 shows the parameters that are kept constant during this analysis and Figure 3.19 shows the change of the magnitude of $T_x$ and $T_y$ for $r_i$ at 3.8 mm and 4.8 mm. The change in $r_i$ also changes the distance between the rings, $d$. As the dimension of the radiator changes, a similar behavior with the previous case is observed on the intersection frequency. However, in this case, resonance frequencies for $\Gamma_x$ are affected more than $\Gamma_y$, due to both the change of the dimension of the inner ring and of the amount of coupling between the rings because of the change in $d$ value. Figure 3.20 shows the related reflection coefficient characteristics.

Table 3.10     The parametric analysis of the IS-SRR transmitarray unit cell with
respect to the radius of the inner ring.

| Inner radius | $T_x$ and $T_y$ intersection frequency | $T_x$ and $T_y$ intersection magnitude | $\angle T_y - \angle T_x$ at intersection |
|---|---|---|---|
| 2.85 mm | 10.1 GHz | $-5.38$ dB | 120 |
| 2.95 mm | 9.65 GHz | $-4.45$ dB | 124 |
| 3.05 mm | 8.99 GHz | $-1.42$ dB | 145 |
| 3.15 mm | 8.8 GHz | $-2.2$ dB | 180 |
| 3.25 mm | 8.69 GHz | $-3.85$ dB | 210 |
| 3.35 mm | 8.54 GHz | $-6.1$ dB | 237 |
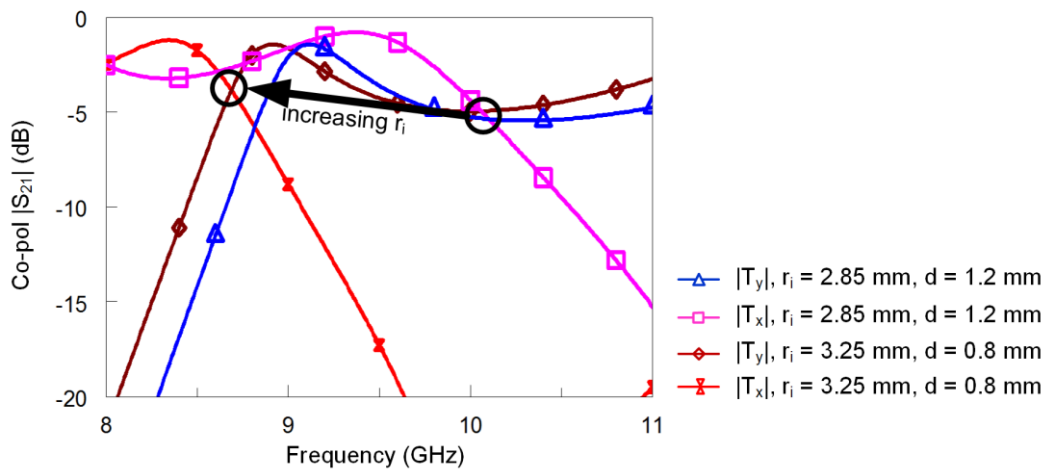


Figure 3.19     Transmission coefficient characteristics of the unit cell with respect to
the change in the radius of the inner ring.

Table 3.11    The constant parameters for the radius of the inner ring analysis.

| Outer ring radius ($r_o$) | Substrate thickness ($t$) | Split length ($g$) | PDMS thickness ($p$) | Ring width ($w$) |
|---|---|---|---|---|
| 4.55 mm | 5.5 mm | 2.05 mm | 1.75 mm | 0.5 mm |
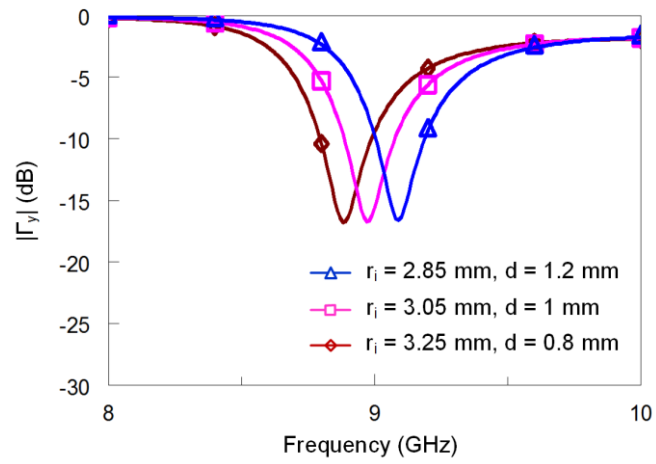


(a)
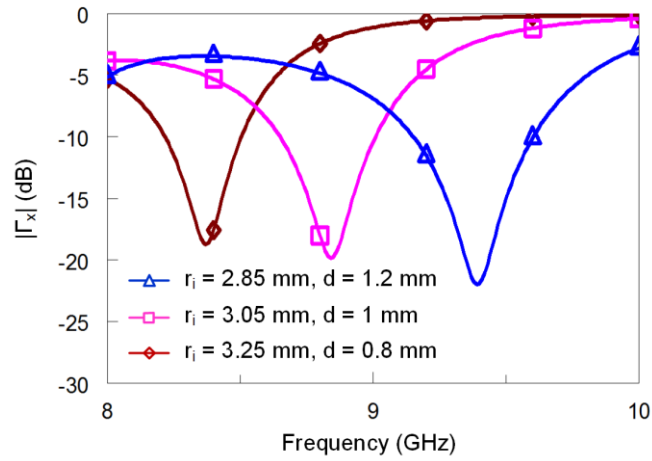


(b)

Figure 3.20    Reflection coefficient characteristics of the unit cell with respect to the change in the radius of the inner ring. (a) $\Gamma_y$, (b) $\Gamma_x$.

### 3.2.1.1.6. The PDMS Thickness

Table 3.12 shows the values of the operating frequency, corresponding transmission magnitude and the phase difference between $T_y$ and $T_x$ with respect to the change in the PDMS thickness, $p$. During this analysis, the values of the other parameters which are kept constant are given in Table 3.13. Increasing the thickness of the PDMS decreases the intersection frequency of $T_y$ and $T_x$ and the phase difference between them. The reflection coefficient characteristics for $\Gamma_x$ and $\Gamma_y$ are shown in Figure 3.21 whereas the change of the magnitude of $T_x$ and $T_y$ for $p$ at 1.75 mm and 2.75 mm is shown Figure 3.22.

Table 3.12    The parametric analysis of the IS-SRR transmitarray unit cell with respect to the PDMS thickness.

| PDMS Thickness | $T_x$ and $T_y$ intersection frequency | $T_x$ and $T_y$ intersection magnitude | $\angle T_y - \angle T_x$ at intersection |
|---|---|---|---|
| 1.5 mm | 8.82 GHz | −2.22 dB | 182 |
| 1.75 mm | 8.8 GHz | −2.2 dB | 180 |
| 2 mm | 8.74 GHz | −2.25 dB | 178 |
| 2.25 mm | 8.72 GHz | −2.23 dB | 175 |
| 2.5 mm | 8.7 GHz | −2.25 dB | 173 |
| 2.75 mm | 8.68 GHz | −2.22 dB | 170 |
| 3 mm | 8.66 GHz | −2.21 dB | 167 |

Table 3.13    The constant parameters for the PDMS thickness analysis.

| Outer ring radius ($r_o$) | Inner ring radius ($r_i$) | Ring width ($w$) | Substrate thickness ($t$) | Split length ($g$) | Distance between rings ($d$) |
|---|---|---|---|---|---|
| 4.55 mm | 3.15 mm | 0.5 mm | 5.5 mm | 2.05 mm | 0.9 mm |
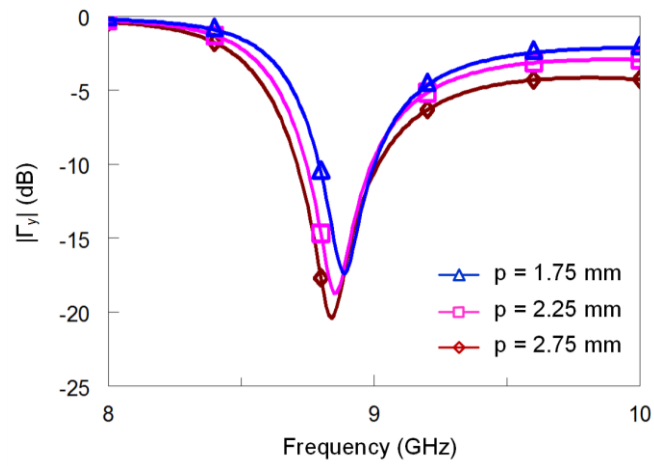


(a)
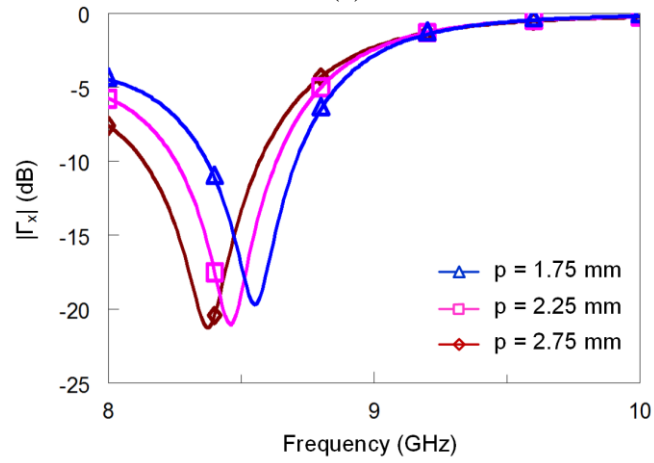


(b)

Figure 3.21    Reflection coefficient characteristics of the unit cell with respect to the change in the PDMS thickness. (a) $\Gamma_y$, (b) $\Gamma_x$.
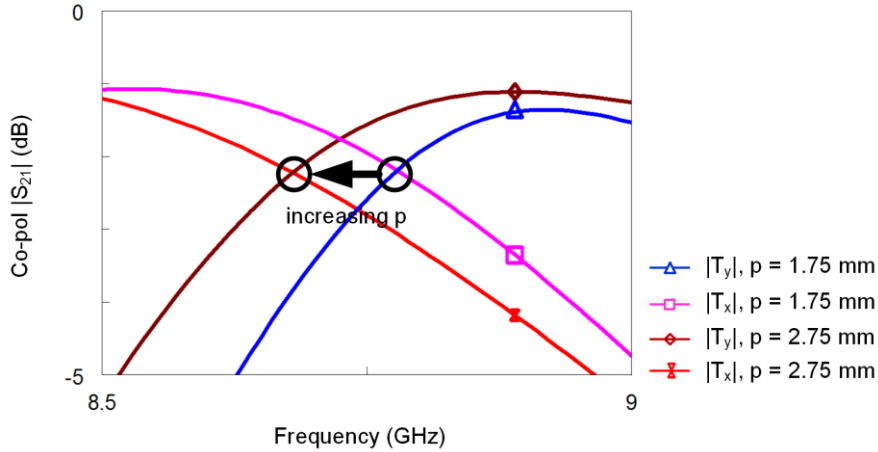
Figure 3.22    Transmission coefficient characteristics of the unit cell with respect to the change in the thickness of PDMS.

### 3.2.2. Phase Design Curve

Figure 3.23 shows the phase design curve, i.e., the phase of the transmitted wave versus angle of rotation of the split, obtained by the simulations for the parameter values in Table 3.1. The phase of the circularly polarized transmitted wave changes linearly with the rotation angle, as expected. Furthermore, the full 360° of phase range is obtained.

### 3.2.3. Transmission Magnitude

Figure 3.24 shows the magnitude of the scattered waves with respect to the frequency. For a left hand circularly polarized excitation, in the vicinity of 8.8 GHz, the cross-pol transmission component ($S_{21}^{ll}$) and right hand reflected component ($S_{11}^{rl}$) are suppressed significantly; whereas left hand reflected component ($S_{11}^{ll}$) is only 7-8 dB below co-polarized transmitted wave.
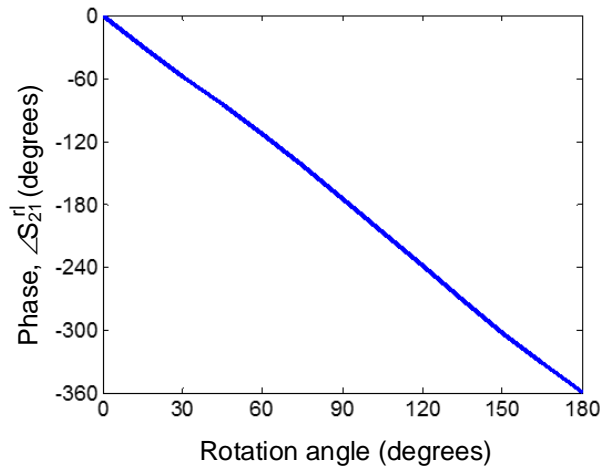
Figure 3.23     The transmission phase, the phase of $S_{21}^{rl}$, with respect to the rotation angle at 8.8 GHz.
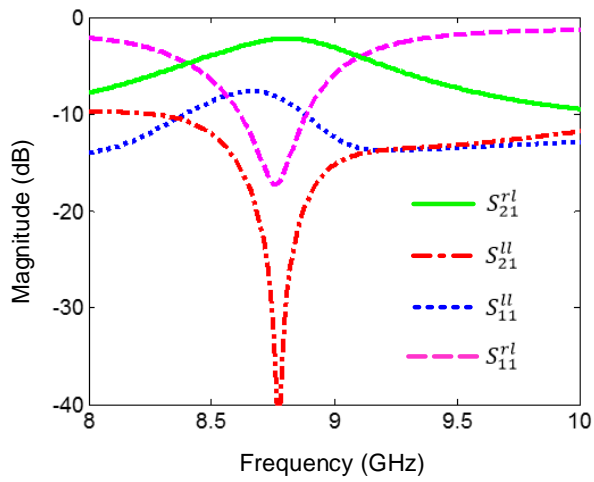


Figure 3.24     Magnitude of the scattered waves with respect to frequency.

When the magnitude variation of the scattered waves with respect to the rotation angle is examined in Figure 3.25, it can be deduced that, illuminated by a left hand circularly polarized wave, the magnitude of the cross-polarization components ($S_{21}^{ll}$, $S_{11}^{ll}$, $S_{11}^{rl}$) increases when the magnitude of the co-pol component ($S_{21}^{rl}$) decreases. Although magnitude of the left hand reflection, $S_{11}^{ll}$, increases, the magnitude of the co-pol component is satisfactorily high.
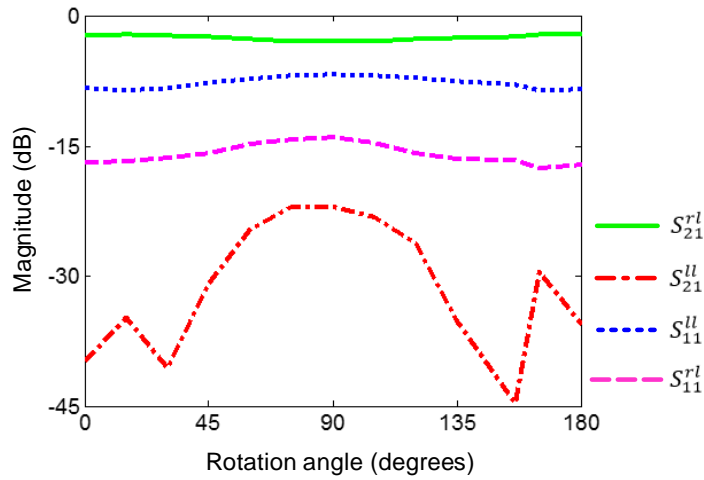


Figure 3.25    Magnitude of the scattered waves with respect to the rotation angle.

Figure 3.26 shows the magnitude of the co-pol component ($S_{21}^{rl}$) with respect to the incidence angle, the angle between the surface normal and the propagation direction, for four different rotation angles. The insertion loss is less than −3 dB up to 25° for all of the rotation angles in the analysis. It can be deduced from this graph that to attain a good radiation performance, the overall size of a transmitarray consisting of IS-SRR unit cells should be determined to provide an incidence angle less than 25° for the elements located at the edges of the transmitarray.
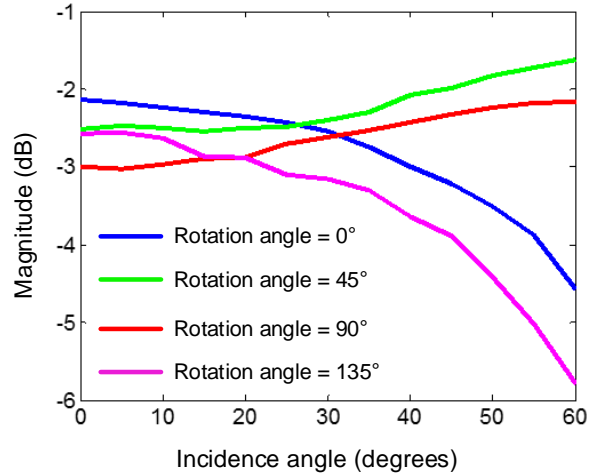
Figure 3.26    Magnitude of $S_{21}^{rl}$ with respect to the incidence angle for various rotation angles.

### 3.2.4.  Examination on the Effects of Fabrication Tolerances

In order to assess the sensitivity of the design with respect to fabrication tolerances, simulations were carried out. One of the major source of fabrication related sensitivity is the slip of the liquid location and length from the designed values, which may occur during the injection of the liquid metal. Keeping the split length and the position as the designed value for one layer, these values are parameterized for the other layer in the simulations. It is seen from Figure 3.27 that the change in the angular position has a more pronounced effect on the transmission magnitude. This is because, as the angular position of the split differs from each other between layers, the intersection magnitude of $T_{xy}$ and $T_{yx}$ increases up to $-6.5$ dB which increases the cross-pol transmission.
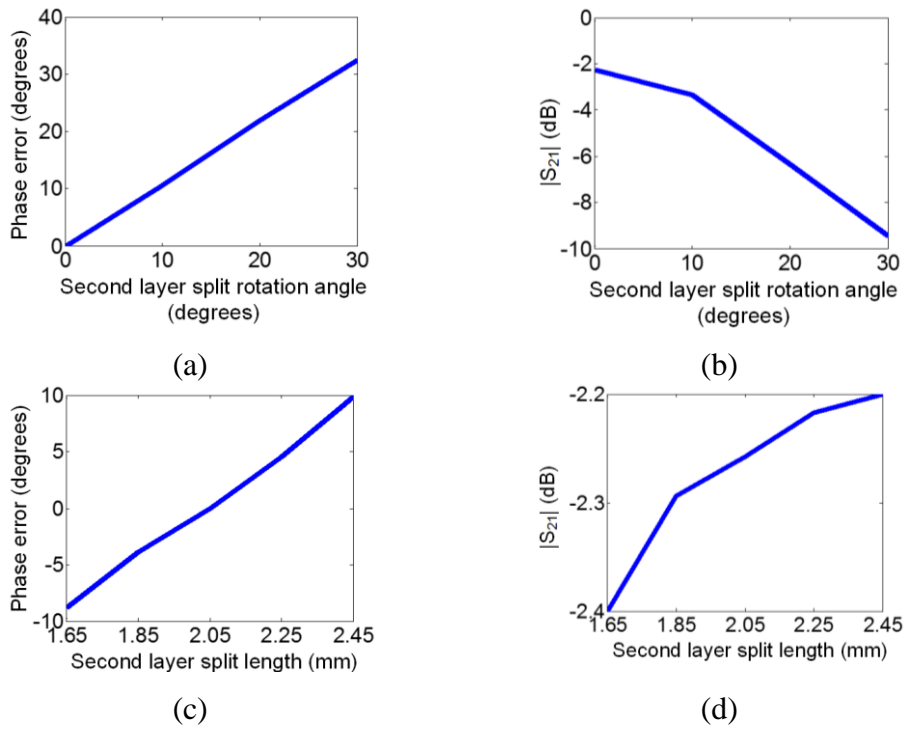
Figure 3.27    The phase and magnitude characteristics with respect to the changes in the split parameters in one layer. a) Phase error and b) transmission magnitude when the angular position of the split in the second layer changes with respect to the split in the first layer. c) Phase error and d) transmission magnitude with respect to the variation in the length of the split in the second layer.

The design is also optimized for different lengths of the split and thickness values of the glass substrate for the possibility of slip in split length that may again occur during the injection. Table 3.14 shows the values of these parameters. Considering the available glass wafers that are already acquired by fabrication facilities at METU-MEMS, the substrate thickness values are selected to be the multiples of 0.5 mm.

Table 3.14    The values of the design parameters optimized for different lengths of the split and thickness of the glass substrate.

| Substrate thickness | Split length | $T_x$ and $T_y$ intersection frequency | $T_x$ and $T_y$ intersection magnitude | $\angle T_y - \angle T_x$ |
|---|---|---|---|---|
| 6 mm | 1 mm | 8.34 GHz | $-2.33$ dB | 180 |
| 5 mm | 2.8 mm | 9.21 GHz | $-2.22$ dB | 180 |
| 4.5 mm | 3.5 mm | 9.57 GHz | $-2.25$ dB | 180 |
| 4 mm | 3.75 mm | 10.01 GHz | $-2.55$ dB | 180 |
| 3.5 mm | 4.1 mm | 10.39 GHz | $-2.72$ dB | 180 |
| 3 mm | 4.4 mm | 10.81 GHz | $-3$ dB | 180 |

### 3.2.5.  Design Guideline

In this section the design rules that should be followed to design the transmitarray unit cell developed in this thesis are presented based on the performed parametric study and design experience gained throughout this study. Designing a transmitarray unit cell employing the element rotation method requires satisfaction of the design conditions at the operating frequency. Ensuring the design conditions mainly depends on the frequency difference between the orthogonal polarized reflection and transmission coefficients. These conditions can be satisfied by taking into account the effects of the physical parameters on the change of the phase difference, operating frequency and transmission magnitude, which are described in the parametric analysis section, in Section 3.2.1.1. Therefore, once the resonances for the orthogonal polarized waves are formed, the frequency difference between these resonances can be changed by adjusting the appropriate physical parameter. Unit cell design steps are itemized and explained by applying them to a design example for the prospective designer.

**Step 1:** Determination of the size of the unit cell

In order to have the design conditions being usable, the number of the propagating modes should be ensured to match the number used in the derivation of the design conditions. The derivation of the design conditions in Chapter 2 involves *x*- and *y*-polarized wave modes. As mentioned in Section 2.2, for a unit cell smaller than half a free space wavelength, $0.5\lambda_0$, and a plane wave propagation in *z*- direction, the propagating modes are *x*- and *y*-polarized modes for normal incidence. Therefore, to have the derived conditions be valid, the size of the unit cell should be selected smaller than half a free space wavelength.

**Step 2:** Determination of fixed parameters and restrictions on the parameters

There may be other restrictions mainly arising from the fabrication processes. In our designs, minimum values of the ring width and the thickness of the PDMS layer are determined according to the specifications of the injector used to inject the liquid metal. As the opening of the injector has an inclined section and has a diameter around 0.5 mm, for a successful injection of the liquid metal into the channels, the ring width and the thickness of the PDMS layer should not be smaller than 0.5 mm and 1.5 mm, respectively. Also, as a safety margin in fabrication, the distance between the rings is designed to be higher than 0.1 mm. Furthermore, as the liquid metal is injected to the channels manually, the split length size should not be very small to prevent the channels filled with the liquid metal.

**Step 3:** Determination of initial size of the outer and inner rings

As mentioned in Section 3.2.1.1.1, the outer ring is more effective on the resonant frequency in the examined frequency range for $\Gamma_y$. Thus, determination of the outer ring parameters can be a starting point in the design of an IS-SRR transmitarray unit cell. Taking the inner ring slightly smaller than the outer ring, resonances can be formed for both orthogonal polarized waves. To assign the size of the outer ring in terms of wavelength, a rough estimation of the effective permittivity can be done. For a structure in Figure 3.28 where the thicknesses of the PDMS layer and the glass layer

are 1.75 mm and 5 mm, respectively, the effective permittivity of the structure can be roughly estimated as

$$\varepsilon_{eff} = \frac{\varepsilon_{pdms} + \varepsilon_{glass}}{2} \qquad (3.1)$$

and the guided wavelength is,

$$\lambda_g = \frac{\lambda_0}{\sqrt{\varepsilon_{eff}}} . \qquad (3.2)$$
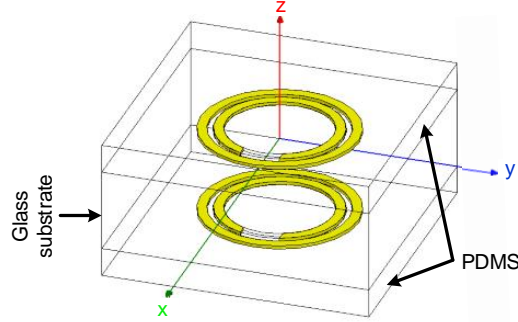


Figure 3.28    Geometry of the IS-SRR unit cell.

When the perimeter of the outer ring is taken as approximately $1.5\lambda_g$, a resonance occurs in the vicinity of the operating frequency. For a sample design aimed to operate at 9.5 GHz; taking the radius of the outer ring as 4 mm and ring width as 0.5 mm, satisfying a ring perimeter of $1.5\lambda_g$, gives a resonance at 9.45 GHz for a unit cell size of 13.5 mm × 13.5 mm which is approximately $0.43\lambda_0$ at 9.5 GHz. It should be noted that, in our unit cell designs in this thesis, the unit cell size is determined by the dimensions of the WR-90 waveguide and fixed at 11.43 mm × 10.16 mm. Taking the inner ring radius as 3.2 mm with a split length of 2 mm, the characteristics in Figure

3.29 are obtained. From these figures, it is seen that the phase difference between $T_y$ and $T_x$, $\angle T_y - \angle T_x$, is 220° (i.e., phase difference between $T_x$ and $T_y$, $\angle T_x - \angle T_y$, is 140° as in the figure) and the operating frequency of the design is 9.4 GHz.



(a)

(b)

(c)
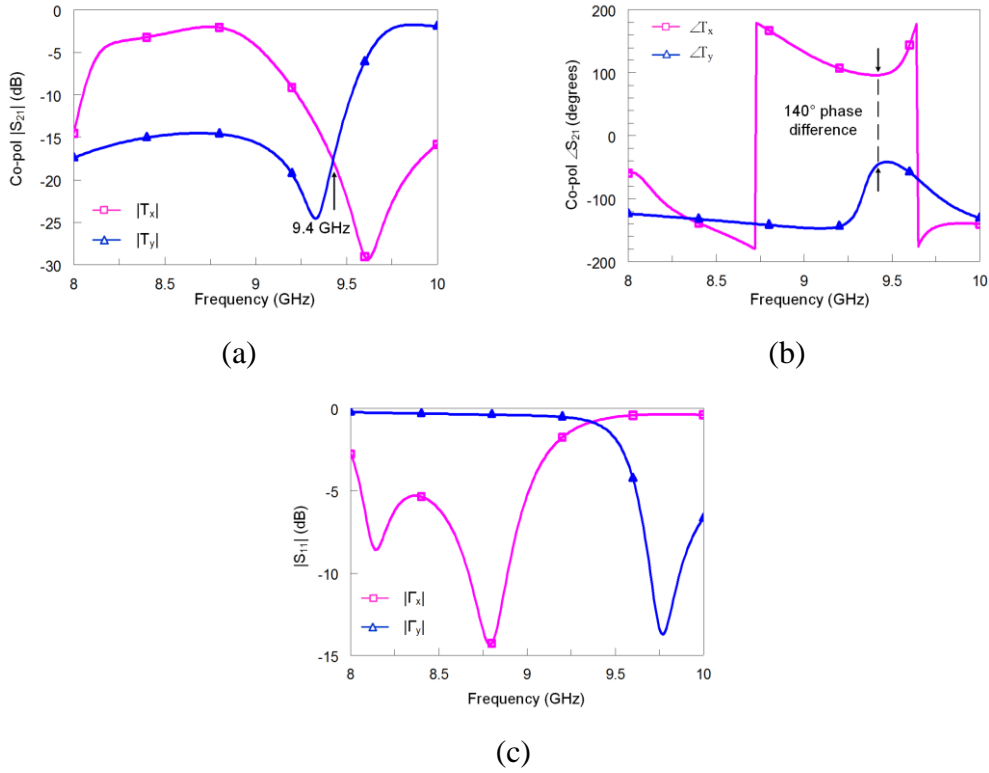
Figure 3.29     Simulated characteristics of the IS-SRR transmitarray unit cell for outer ring radius of 4 mm, inner ring radius of 3.2 mm, ring width of 0.5 mm and split length of 2 mm. (a) Magnitude of the co-pol transmission coefficients, (b) phase of the co-pol transmission coefficients, (c) magnitude of the reflection coefficients.

These characteristics are sufficient to implement the results of the parametric analysis in Section 3.2.1.1.

**Step 4:** Tuning by the most effective parameters such as radii of rings

To satisfy the design conditions, the phase difference between $T_y$ and $T_x$ should be decreased to 180° and the operating frequency should be increased to 9.5 GHz. As analyzed in Section 3.2.1.1.5, decreasing the radius of the outer ring makes the resonance frequencies for $\Gamma_x$ and $\Gamma_y$ approach each other by increasing the resonance frequency for $\Gamma_x$. When the inner ring radius is reduced to 3.05 mm, the operating frequency is increased to 9.56 GHz and the phase difference between $T_y$ and $T_x$ is reduced to 200° (i.e., phase difference between $T_x$ and $T_y$, $\angle T_x - \angle T_y$, is 160°), as shown in Figure 3.30.



(a)                                        (b)

(c)
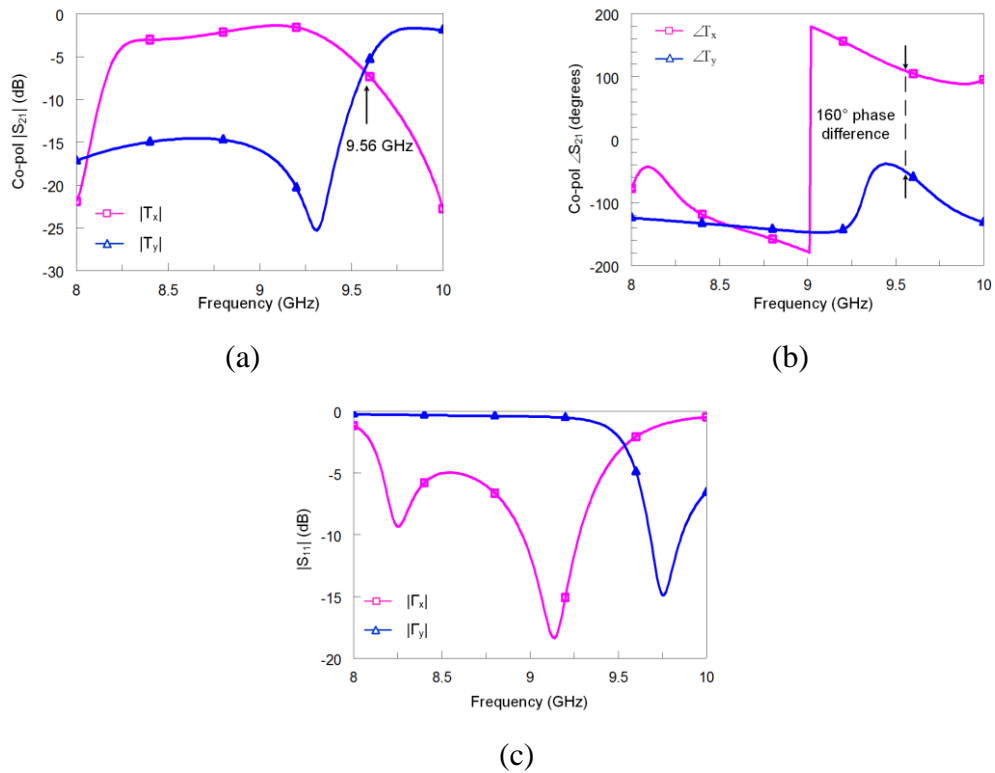
Figure 3.30     Simulated characteristics of the IS-SRR transmitarray unit cell for outer ring radius of 4 mm, inner ring radius of 3.05 mm, ring width of 0.5 mm and split length of 2 mm. (a) Magnitude of the co-pol transmission coefficients, (b) phase of the co-pol transmission coefficients, (c) magnitude of the reflection coefficients.

Decreasing the radius of the outer ring decreases the phase difference between $T_y$ and $T_x$ and the operating frequency as presented in Section 3.2.1.1.4. Following these steps, the design conditions are satisfied at 9.5 GHz for the radius of the outer and inner rings of 4.1 mm and 3.03 mm, respectively. For these parameter values, the magnitude of $T_y$ and $T_x$ is -4.37 dB at 9.5 GHz, as shown in Figure 3.31. Also, at the design frequency, the magnitudes of $T_{xy}$ and $T_{yx}$ should be checked. It is seen that these characteristics are below $-50$ dB at the design frequency.



(a)

(b)

(c)

(d)
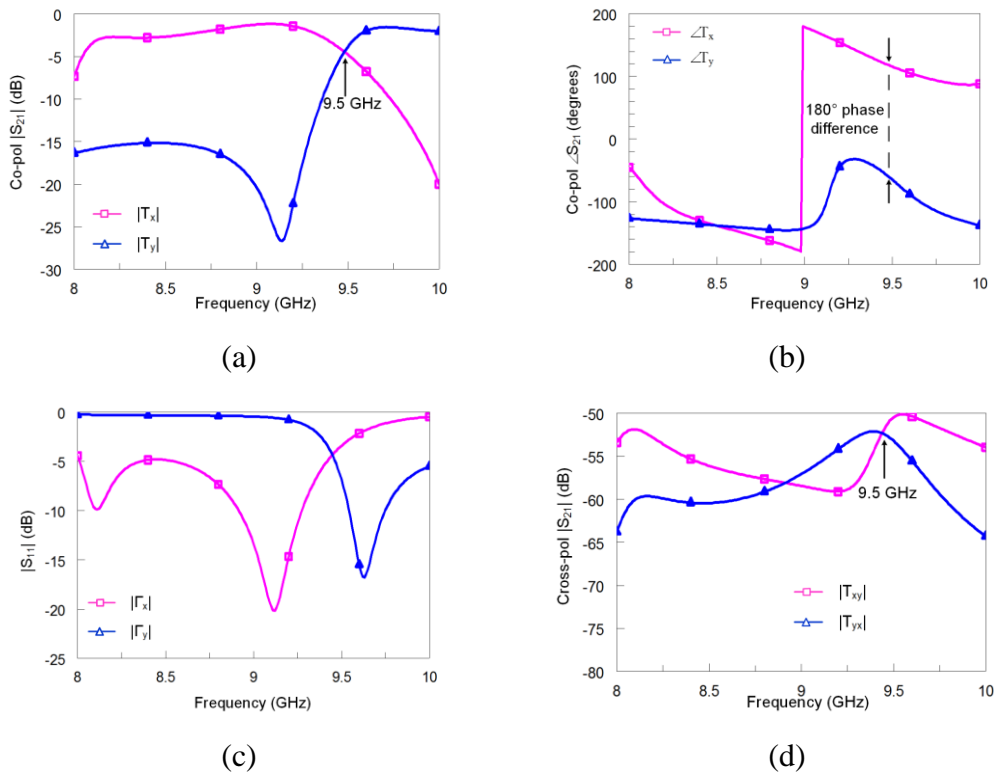
Figure 3.31    Simulated characteristics of the IS-SRR transmitarray unit cell for outer ring radius of 4.1 mm, inner ring radius of 3.03 mm, ring width of 0.5 mm and split length of 2 mm. (a) Magnitude of the co-pol transmission coefficients, (b) phase of the co-pol transmission coefficients, (c) magnitude of the reflection coefficients, (d) magnitude of the cross-pol transmission coefficients.

**Step 5:** Fine tuning with other parameters to reduce insertion loss (if necessary)

The 180° of phase difference between $T_y$ and $T_x$ at the operating frequency can be obtained for many parameter values. Therefore, solutions satisfying the design conditions with better transmission magnitude should be checked. The parameter values should be changed by considering the effects on the operating frequency and phase difference between $T_y$ and $T_x$. From Section 3.2.1.1, it is known that, increasing the radius of the outer ring decreases the operating frequency and phase difference between $T_y$ and $T_x$, increasing the radius of the inner ring decreases the operating frequency and increases the phase difference between $T_y$ and $T_x$ whereas increasing the split length increases the operating frequency and decreases the phase difference between $T_y$ and $T_x$. For the outer and inner rings radii of 4.25 mm and 3.1 mm and split length of 2.8 mm, 150° of phase difference is achieved at 9.46 GHz with a transmission magnitude of −2.25 dB. Increasing the width of the rings as explained in Section 3.2.1.1.3, increases the phase difference between $T_y$ and $T_x$ without increasing the operating frequency significantly. Increasing the width of the rings to 0.6 mm, design conditions are obtained at 9.5 GHz with a transmission magnitude of −3.8 dB. Both set of parameters satisfying the design conditions are given in Table 3.15. From this table, an incremental relation between the values of parameters on increasing the transmission magnitude of $T_y$ and $T_x$ at the operating frequency is observed. Following this incremental ratio of the parameter values, different solutions can be obtained as shown in Table 3.16.

Table 3.15     The values of the design parameters satisfying the design conditions at 9.5 GHz.

| Outer ring radius | Inner ring radius | Split length | Ring width | $T_x$ and $T_y$ intersection magnitude |
|---|---|---|---|---|
| 4.1 mm | 3.03 mm | 2 mm | 0.5 mm | −4.37 dB |
| 4.25 mm | 3.1 mm | 2.8 mm | 0.6 mm | −3.8 dB |

Table 3.16     Different set of values of the design parameters satisfying the design conditions at 9.5 GHz.

| Outer ring radius | Inner ring radius | Split length | Ring width | $T_x$ and $T_y$ intersection magnitude |
|---|---|---|---|---|
| 4.61 mm | 3.31 mm | 3.5 mm | 0.72 mm | −3.35 dB |
| 4.85 mm | 3.48 mm | 4.4 mm | 0.8 mm | −3.02 dB |

If there is no constraint on the substrate thickness or unit cell size, these parameters can also be included in the analysis. Changing one parameter value at each step, the operating frequency, phase difference and transmission magnitude values are evaluated and the operating frequency and the phase difference values are tuned to satisfy the design conditions by the methodology described above and in Section 3.2.1. Applying this approach, design conditions are satisfied with a transmission magnitude of −2.3 dB for the glass substrate thickness of 4.5 mm and unit cell size of 11.5 mm × 11.5 mm. The values of the other parameters in the design are given in Table 3.17 and the characteristics are shown in Figure 3.32. It is considered that the reduction in the unit cell size increases the ratio of the radiator area to the unit cell size and affects the transmission magnitude level.

Table 3.17     Values of the design parameters satisfying the design conditions at 9.5 GHz for glass substrate thickness of 4.5 mm and unit cell size of 11.5 mm × 11.5 mm.

| Outer ring radius | Inner ring radius | Split length | Ring width | $T_x$ and $T_y$ intersection magnitude |
|---|---|---|---|---|
| 5.04 mm | 3.44 mm | 4.4 mm | 0.68 mm | −2.3 dB |
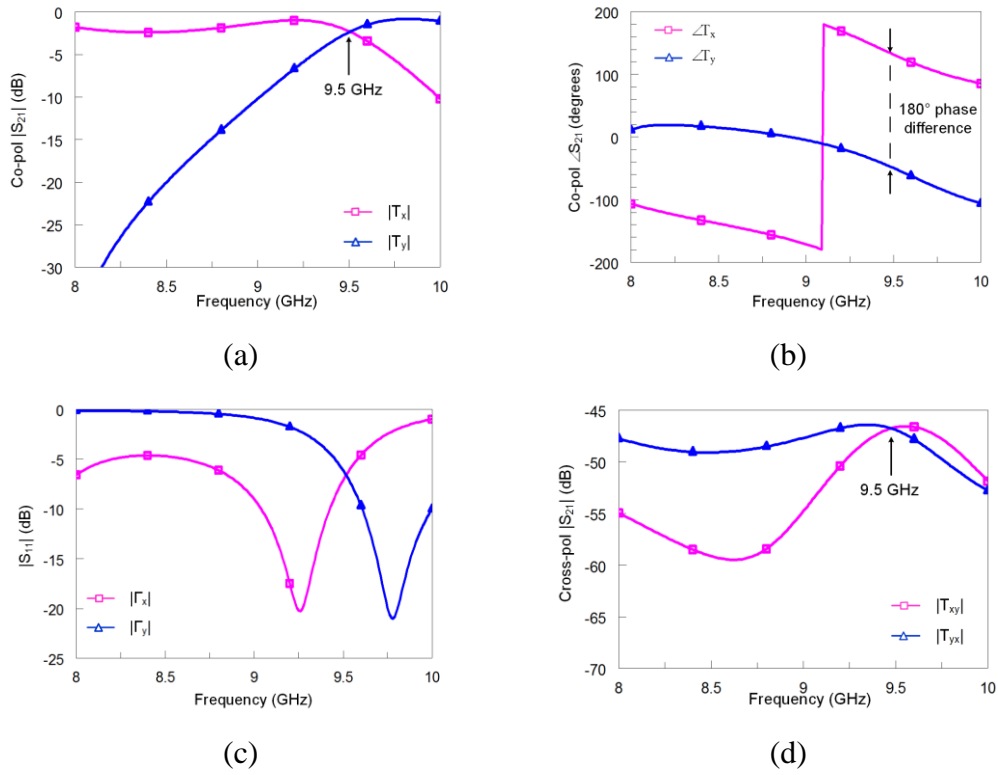
Figure 3.32    Simulated characteristics of the IS-SRR transmitarray unit cell for substrate thickness of 4.5 mm, unit cell size of 11.5 mm × 11.5 mm, outer ring radius of 5.04 mm, inner ring radius of 3.44 mm, ring width of 0.68 mm and split length of 4.4 mm. (a) Magnitude of the co-pol transmission coefficients, (b) phase of the co-pol transmission coefficients, (c) magnitude of the reflection coefficients.

# CHAPTER 4

# OBSERVATIONS ON THE EFFECT OF GEOMETRICAL SYMMETRY ON THE INSERTION LOSS

## 4.1.    Introduction

In this chapter, the variation in the insertion loss of the CSRR and SRR-based transmitarray unit cells is examined with respect to the rotation angle, which is an issue that has not been investigated in the literature in this context, so far. Insertion loss of each element is a parameter that the variations on this magnitude may affect the overall gain and efficiency of the antenna. Therefore, determining the factors affecting this parameter and proposing a solution to alleviate the variations is important in the design stage of the unit cell.

It is shown by simulations that the insertion loss variation with respect to the rotation angle depends on the axial symmetry of the element in the unit cell and the structural symmetry has effect on decreasing the value of the variation. In the unit cell designs, Floquet port excitation and periodic boundary conditions in Ansys HFSS® are used. As the study involves with the examination on the insertion loss with respect to the rotation angle rather than designing a producible and measurable transmitarray unit cell with a microfluidics approach, in the simulations, PDMS layer does not exist and the metal layers are taken as perfect electric conductors.

## 4.2. Insertion Loss Variation in the Element Rotation Method

The circularly polarized S-parameters after satisfying the mentioned conditions, (2.10), (2.13), (2.16), and (2.19), demonstrate that the phase of the transmitted wave changes two times the rotation angle without changing the magnitude. However, full-wave EM simulations indicate that the magnitude changes with the change in the rotation angle. This is mainly because the amount of the existing electromagnetic coupling between the elements changes with the rotation angle [23]. Since this coupling affects the overall array characteristics [24], it is important to determine the parameters reducing the adverse effects of it on the insertion loss and make the designs by taking into account these parameters.

It should also be noted that the element rotation method is based on the rotation of the entire structure i.e., the lattice, around its surface normal. However, in an array, the edges of the unit cell generate a boundary that does not rotate with the rotation of the array element as shown in Figure 4.1. Therefore, even all the components of the radiators rotate, the array and the unit cell boundaries are stationary which has an effect on the magnitude of radiation due to the change of the geometry of the structure resulting in change in the element and array factor. From the illustration in Figure 4.1 (b) it can be deduced that the inter-element geometry changes as the element is rotated 45° counter clockwise. The position of the split, its distance to the edges of its unit cell and its distance to the elements in the other unit cells change with respect to the geometry in Figure 4.1 (a).
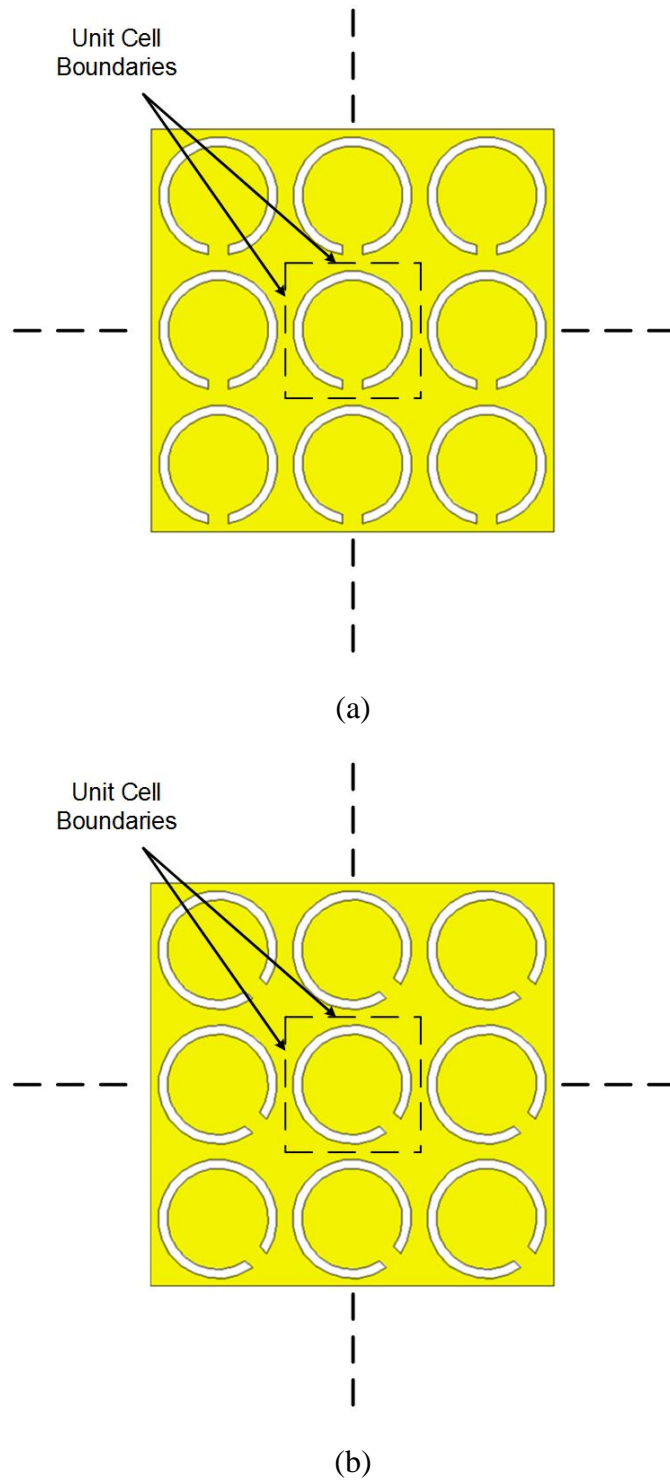
Figure 4.1    (a) Top view of an array formed by repeating identical unit cells at $\psi = 0°$. (b) Top view of the same array at $\psi = 45°$.

### 4.2.1. CSRR Designs

Figure 4.2 shows the schematics of the examined CSRR unit cells which are, nested CSRR (N-CSRR), single ring double split CSRR (DS-CSRR), and single ring single split CSRR (SS-CSRR). The size of the unit cells is 10.16 mm × 10.16 mm, the substrate is glass having thickness of 6 mm and the operating frequency is 9.9 GHz in all structures. The dimensions of the other parameters of the structures given in Table 4.1. When the transmission magnitudes of the unit cells at their operating frequencies with respect to the rotation angle in Figure 4.3 are observed, it is seen that the transmission behaviors of the structures are similar and the magnitude is varying with the change in the rotation angle. However, the insertion loss is lower and the variation in the insertion loss is less for the symmetrical structure, DS-CSRR.

Table 4.1    Dimensions of the CSRR unit cells.

|                   | SS-CSRR  | DS-CSRR   | N-CSRR                |
|-------------------|----------|-----------|-----------------------|
| Split length (mm) | 1        | 0.26      | 3.3 (both splits)     |
| Ring width (mm)   | 4 – 3.38 | 4.3 – 3.3 | 4.2 – 3.75 (outer ring) |
|                   |          |           | 3 – 2.55 (inner ring) |
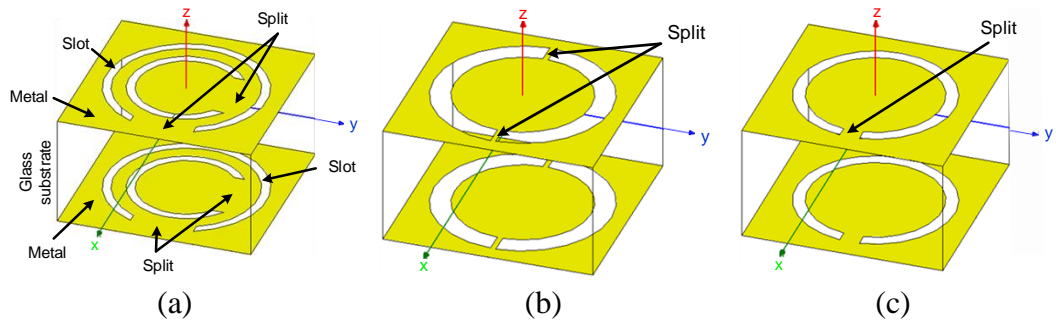
Figure 4.2    Schematics of the CSRR unit cells. (a) The nested CSRR (N-CSRR). (b) Single ring double split CSRR (DS-CSRR). (c) Single ring single split CSRR (SS-CSRR).
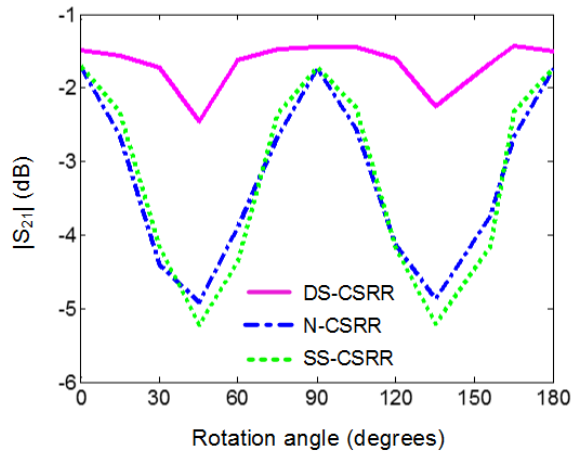


Figure 4.3    Circularly polarized transmission coefficients of the CSRR unit cells.

## 4.2.1.1.    S-parameters analysis of CSRR Designs

To extract the relationship between the symmetrical geometry and the insertion loss level, S-parameters and the rotated S-parameters of the structures are examined and

compared. The parameters for DS-CSRR and SS-CSRR are given and discussed below.

Table 4.2 and Table 4.3 present the S-parameters of DS-CSRR obtained by simulating the unit cells at $\psi = 0°$ and $\psi = 45°$, respectively whereas Table 4.5 and Table 4.6 present those for SS-CSRR. Table 4.4 shows the S-parameters obtained by applying (2.2) at $\psi = 45°$ to the S-parameters in Table 4.2. Therefore, both Table 4.3 and Table 4.4 show the *S*-parameters at $\psi = 45°$, however, Table 4.3 is obtained directly by the simulations whereas Table 4.4 is obtained by analytical manipulation. Similar analysis is carried out for SS-CSRR where the results are provided in Table 4.5, Table 4.6, and Table 4.7, respectively.

It is known that, for a structure symmetrical with respect to all three principal planes, the cross-polarized terms in the scattering matrix are zero [7]. These parameters are emphasized in the scattering matrix below.

$$
\begin{bmatrix} b_1^x \\ b_1^y \\ b_2^x \\ b_2^y \end{bmatrix} = \begin{bmatrix} s_{11}^{xx} & \boxed{s_{11}^{xy}} & s_{12}^{xx} & \boxed{s_{12}^{xy}} \\ \boxed{s_{11}^{yx}} & s_{11}^{yy} & \boxed{s_{12}^{yx}} & s_{12}^{yy} \\ s_{21}^{xx} & \boxed{s_{21}^{xy}} & s_{22}^{xx} & \boxed{s_{22}^{xy}} \\ \boxed{s_{21}^{yx}} & s_{21}^{yy} & \boxed{s_{22}^{yx}} & s_{22}^{yy} \end{bmatrix} \begin{bmatrix} a_1^x \\ a_1^y \\ a_2^x \\ a_2^y \end{bmatrix} \tag{3.1}
$$

It is seen from Table 4.2 that, the cross-polarized terms are close to zero for DS-CSRR, which is a symmetrical structure. It is also observed that the S-parameters in Table 4.3 are more similar in magnitude to those of Table 4.4 for the DS-CSRR compared to those of SS-CSRR as summarized in Table 4.6 and Table 4.7. That is, when the structures are rotated, the magnitudes of the S-parameters of the symmetrical structure is changing less with respect to those of the unsymmetrical structure. The reason of this situation is not evident from analytical expressions. Because, the value of the linearly polarized S-parameters does not change when the structure is rotated, as seen in the formulations provided in (2.10), (2.13), (2.16), and (2.19).

Table 4.2    Simulated S-parameters, $S_\psi^{LP}$, at $\psi = 0°$ for DS-CSRR.

| | | | |
|---|---|---|---|
| −0.1750 + 0.0247j | −0.0003 − 0.0005j | 0.8117 − 0.2390j | 0.0003 + 0.004j |
| −0.0003 − 0.0005j | −0.1604 − 0.4395j | −0.0003 − 0.0004j | −0.8155 + 0.2423j |
| 0.8117 − 0.2390j | −0.0003 − 0.004j | −0.1546 − 0.0304j | 0.0003 + 0.0004j |
| 0.0003 + 0.0004j | −0.8155 + 0.2423j | 0.0003 + 0.0004j | −0.1620 − 0.4390j |

Table 4.3    Simulated S-parameters, $S_\psi^{LP}$, at $\psi = 45°$ for DS-CSRR.

| | | | |
|---|---|---|---|
| −0.2238 − 0.0356j | 0.0312 − 0.4267j | −0.0310 + 0.2309j | −0.7526 + 0.0365j |
| 0.0312 − 0.4267j | −0.2242 −0.0448j | −0.7521 + 0.0439j | −0.0336 + 0.2311j |
| −0.0310 + 0.2309j | −0.7521 + 0.0439j | −0.2288 −0.0448j | 0.0366 − 0.4255j |
| −0.7526 + 0.0365j | −0.0336 + 0.2311j | 0.0366 − 0.4255j | −0.2282 −0.0386j |

Table 4.4    Analytically evaluated S-parameters for DS-CSRR at $\psi = 45°$ using the results in Table 4.2.

| | | | |
|---|---|---|---|
| −0.1680 −0.2326j | 0.0073 − 0.2074j | −0.0019 + 0.0017j | −0.8134 + 0.2411j |
| 0.0073 − 0.2074j | −0.1674 − 0.2317j | −0.8139 + 0.2402j | −0.0019 + 0.0017j |
| −0.0019 + 0.0017j | −0.8139 + 0.2402j | −0.1580 − 0.2343j | −0.0037 − 0.2043j |
| −0.8134 + 0.2411j | −0.0019 + 0.0017j | −0.0037 − 0.2043j | −0.1586 − 0.2352j |

Table 4.5    Simulated S-parameters, $S_\psi^{LP}$, at $\psi = 0°$ for SS-CSRR.

| | | | |
|---|---|---|---|
| −0.2076 − 0.0659j | −0.0063 − 0.0017j | 0.7517 − 0.2903j | 0.0046 + 0.0017j |
| −0.0063 − 0.0017j | −0.2253 − 0.4851j | −0.0070 − 0.0041j | −0.7513 + 0.2918j |
| 0.7517 − 0.2903j | −0.0070 − 0.0041j | −0.2311 − 0.0574j | 0.0052 + 0.0033j |
| 0.0046 + 0.0017j | −0.7513 + 0.2918j | 0.0052 + 0.0033j | −0.2272 − 0.4844j |

Table 4.6    Simulated S-parameters, $S_\psi^{LP}$, at $\psi = 45°$ for SS-CSRR.

| | | | |
|---|---|---|---|
| −0.4588 − 0.0145j | 0.1744 − 0.5052j | −0.1742 + 0.3191j | −0.5196 + 0.0072j |
| 0.1744 − 0.5052j | −0.4581 − 0.0167j | −0.5213 + 0.0125j | −0.1709 + 0.3192j |
| −0.1742 + 0.3191j | −0.5213 + 0.0125j | −0.4596 − 0.0211j | 0.1752 − 0.5032j |
| −0.5196 + 0.0072j | −0.1709 + 0.3192j | 0.1752 − 0.5032j | −0.4622 − 0.0124j |

Table 4.7    Analytically evaluated S-parameters for SS-CSRR at $\psi = 45°$ using the results in Table 4.5.

| | | | |
|---|---|---|---|
| −0.2227 − 0.2772j | −0.0088 − 0.2096j | −0.0010 − 0.0004j | −0.7457 + 0.2939j |
| −0.0088 − 0.2096j | −0.2102 − 0.2738j | −0.7573 + 0.2881j | 0.0014 + 0.0019i |
| −0.0010 − 0.0004j | −0.7573 + 0.2881j | −0.2239 − 0.2676j | 0.0019 − 0.2135j |
| −0.7457 + 0.2939j | 0.0014 + 0.0019i | 0.0019 − 0.2135j | −0.2344 − 0.2741j |

## 4.2.1.2. Field analysis of CSRR Designs

A field analysis is carried out on the designs to show the relation between the symmetry and the magnitude of the *S*-parameters. Excited by *x*- and *y*-polarized incident waves, the magnetic surface current density distribution ($M_s$) of the DS-CSRR at 9.9 GHz, in Figure 4.4, shows that for both polarizations, $M_s$ is symmetrical at $\psi = 0°$ and the symmetrical distribution of $M_s$ is not affected from rotation.

Figure 4.5 shows the $M_s$ for the SS-CSRR at 9.9 GHz. From Figure 4.5 (a) and (b) it is observed that, since the split disturbs the symmetry in *yz*- plane, the distribution is not symmetrical for *x*-polarized excitation whereas it is symmetrical for *y*-polarized excitation at $\psi = 0°$. When the structure is rotated at $\psi = 45°$, in Figure 4.5 (c) and (d), the distribution is denser at one arm of the ring distinctively which increases the cross-polarized radiation. As can be seen from Figure 4.4 and Figure 4.5 that the $M_s$ symmetry on the SS-CSRR is more disturbed due to the rotation than that on the DS-CSRR. This increases the cross-polarized terms in the *S*-matrix and cross-polarized radiation, which in turn affect the transmission characteristics of the element. This can also explain the less similarity in magnitude in the S-parameters between Table 4.6 and Table 4.7.

Figure 4.4    Magnetic surface current density distributions for the DS-CSRR. a) For *x*-polarized wave at $\psi = 0°$. b) For *y*-polarized wave at $\psi = 0°$. c) For *x*-polarized wave at $\psi = 45°$. d) For *y*-polarized wave at $\psi = 45°$.
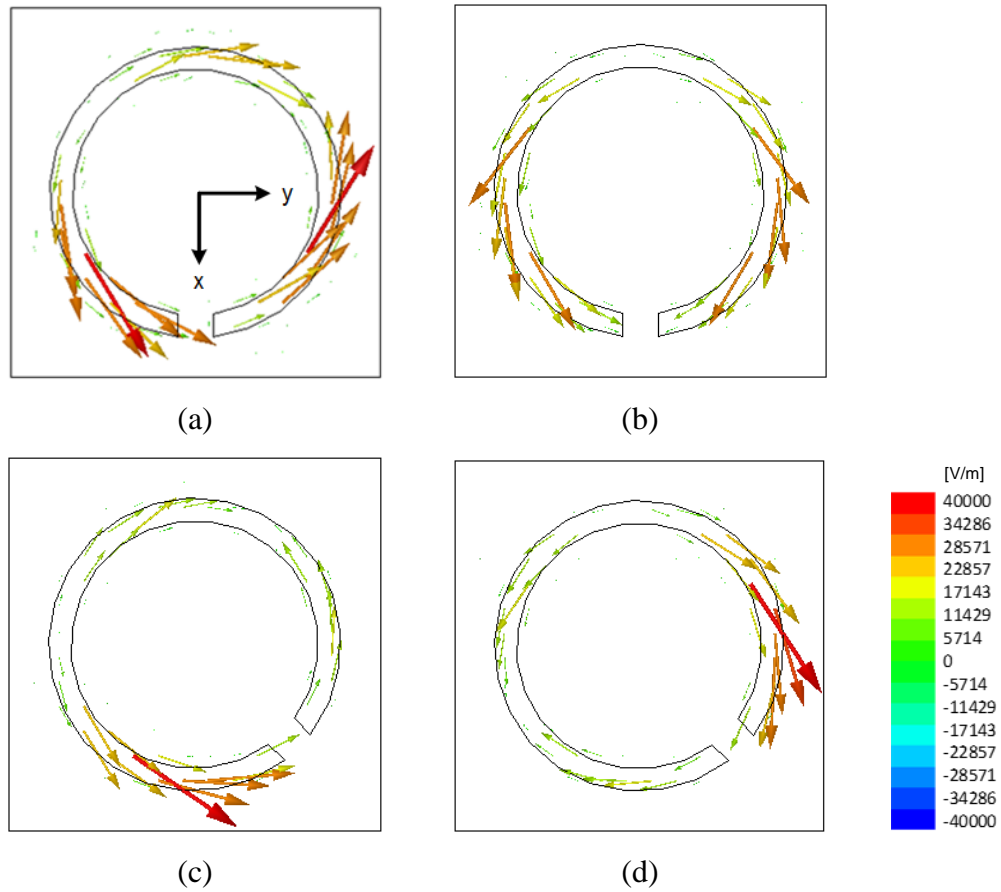
Figure 4.5    Magnetic surface current density distributions for the SS-CSRR. a) For *x*-polarized wave at $\psi = 0°$. b) For *y*-polarized wave at $\psi = 0°$. c) For *x*-polarized wave at $\psi = 45°$. d) For *y*-polarized wave at $\psi = 45°$.

## 4.2.2. SRR Designs

The effect of rotation is also examined for single split SRR structures (IS-SRR and OS-SRR) whose schematics are shown in Figure 4.6 (a) and (b). The split on each design disturbs the symmetrical geometry on *yz*-plane. As in the CSRR designs, the conditions for linear phase shifting are satisfied at 9.9 GHz for the substrate thickness of 6 mm. Other parameters of the structures are given in Table 4.8. When the

transmission magnitudes of the unit cells in Figure 4.7 are observed, although both structures are unsymmetrical for the same plane, it is seen that the IS-SRR has much less insertion loss variation with respect to the rotation angle. In order to clarify this situation, electric surface current density distribution (*Js*) over the rings is examined.



(a)                                        (b)
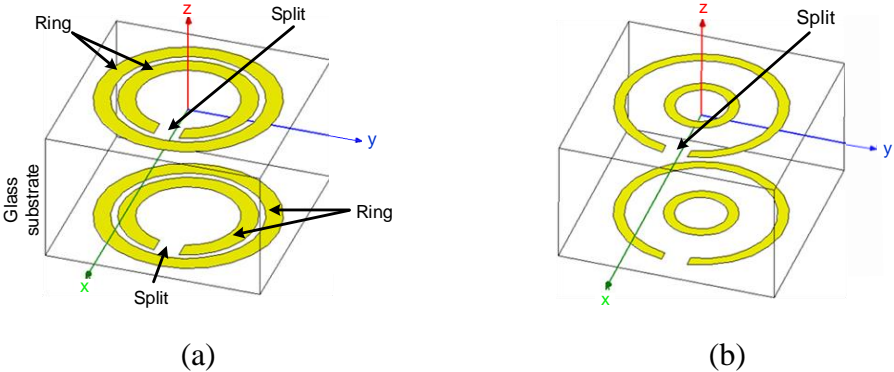
Figure 4.6        Schematics of the SRR unit cells. (a) IS-SRR, (b) OS-SRR.
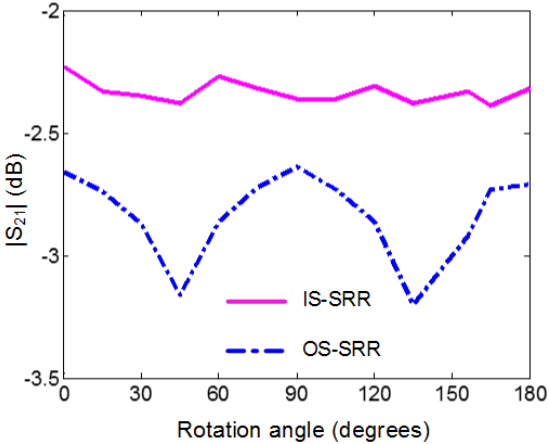


Figure 4.7        Circularly polarized transmission coefficients of the SRR unit cells.

Table 4.8        Dimensions of the SRR unit cells.

| | IS-SRR | OS-SRR |
|---|---|---|
| Split length (mm) | 1.2 | 1.2 |
| Ring width (mm) | 4.29 – 3.49 (outer ring) | 3.95 – 3.45 (outer ring) |
| | 3.17 – 2.37 (inner ring) | 1.7 – 1.2 (inner ring) |

The $J_s$ diagrams for OS-SRR, in Figure 4.8, show that for both polarizations the resonance is mainly determined from the outer ring due to a strong current flow on that ring. Therefore, the disturbance on the current distribution on the outer ring affects the radiation and the transmission magnitude. When the OS-SRR is rotated to $\psi = 45°$, it is seen in Figure 4.8 (c) and (d) that the cross-polarization increases which in turn increases the insertion loss.

When the $J_s$ diagrams for IS-SRR in Figure 4.9 (a) and (b) is examined, it is observed that for $x$-polarized excitation, the outer ring and the inner ring together generate the resonance whereas for $y$-polarized excitation, the resonance is mainly determined from the outer ring due to a stronger current flow on that ring. As the rings are closer to each other, the coupling between them is stronger. When the rings are rotated, the symmetrical distribution on the inner ring is deteriorated which in turn affects the distribution on the outer ring due to coupling. This situation is less pronounced for $y$-polarized excitation as the outer ring is dominant on the determination of the resonance for that polarization. Therefore, the current distribution over the rings is more uniform for that polarization which provides less insertion loss variation. Actually, the less variation of the insertion loss for IS-SRR is mainly due to two reasons: The split does not exist on the outer ring where the current distribution is denser for one of the polarizations, i.e., the outer ring is symmetrical to the orthogonal planes, and the split exists closer to the center of the unit cell which decreases the change in the amount of electromagnetic coupling with the rotation angle.
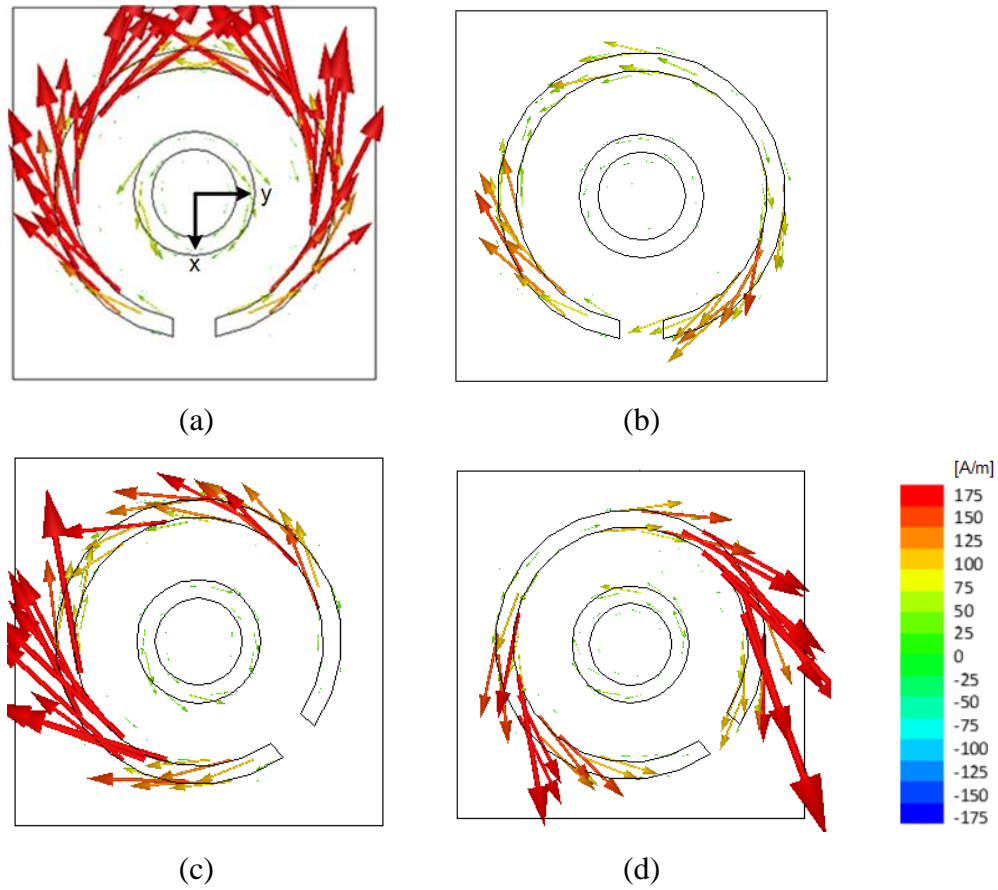
Figure 4.8      Electric surface current density distributions for the OS-SRR. a) For *x*-polarized wave at $\psi = 0°$. b) For *y*-polarized wave at $\psi = 0°$. c) For *x*-polarized wave at $\psi = 45°$. d) For *y*-polarized wave at $\psi = 45°$.
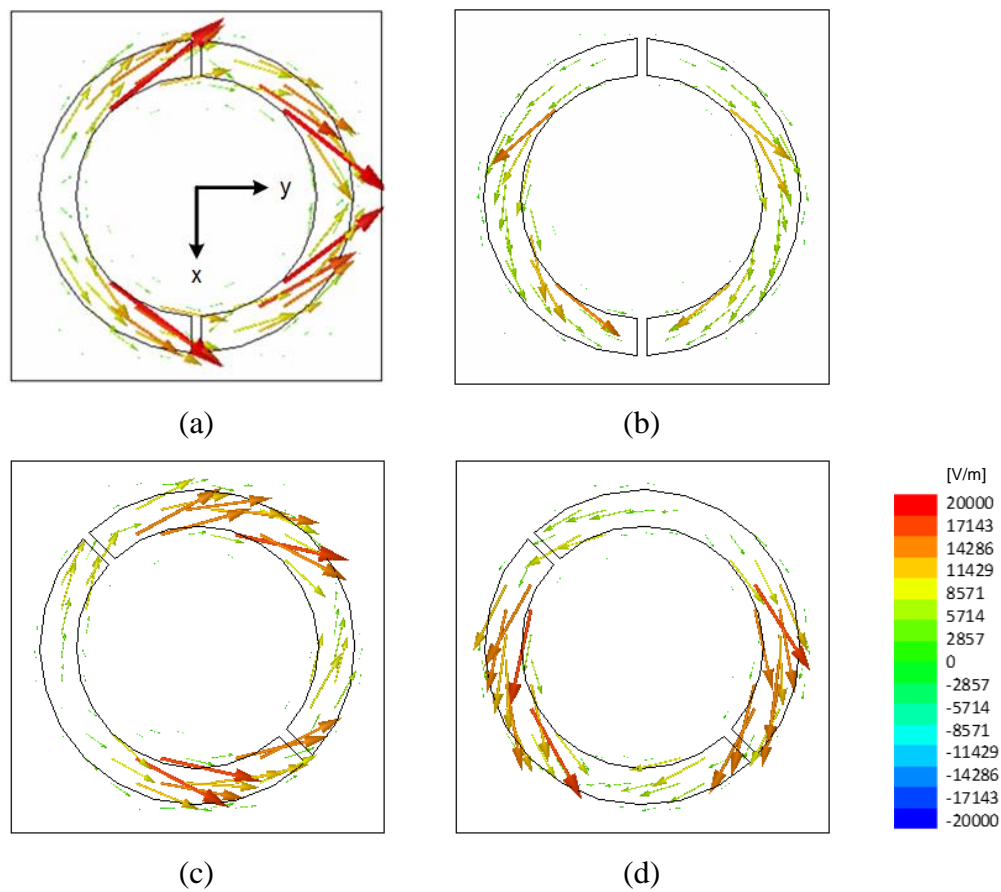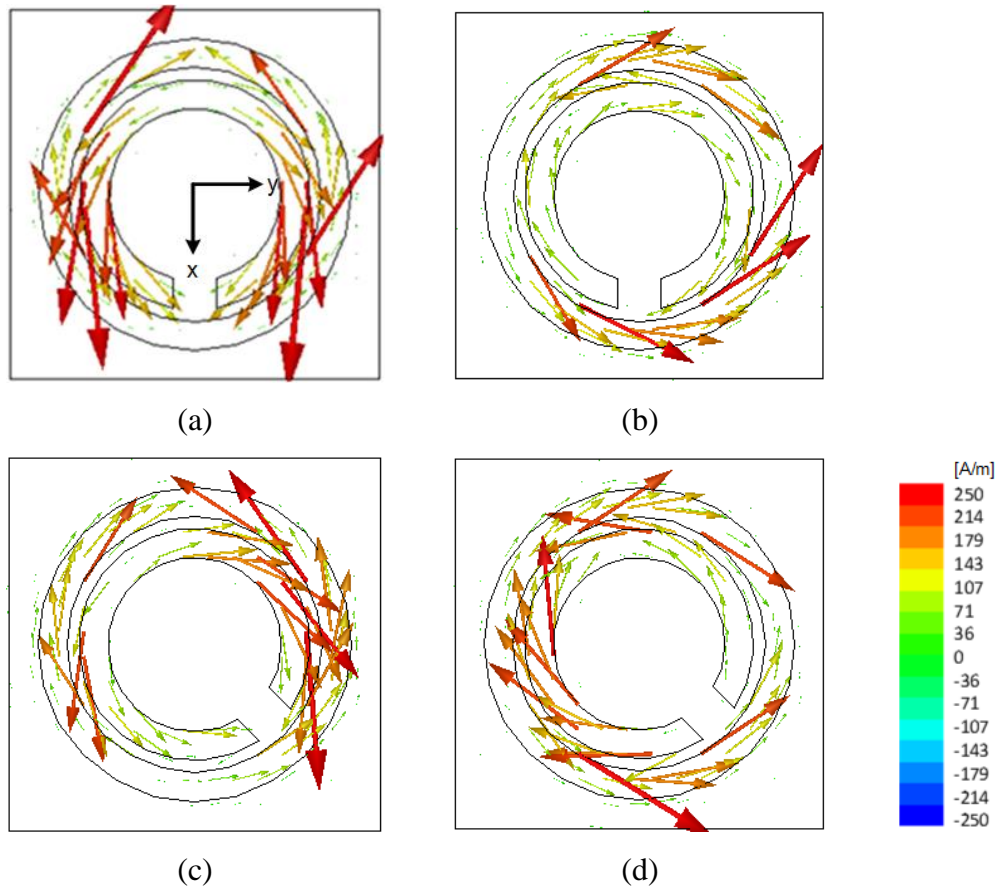
Figure 4.9    Electric surface current density distributions for the IS-SRR. a) For *x*-polarized wave at $\psi = 0°$. b) For *y*-polarized wave at $\psi = 0°$. c) For *x*-polarized wave at $\psi = 45°$. d) For *y*-polarized wave at $\psi = 45°$.

It is also seen from Figure 4.7 that besides the greater variation, the insertion loss of OS-SRR structure is greater than that of the IS-SRR even for $\psi = 0°$. Similar observation is made from the SRR unit cells designed with different parameter values shown in Table 4.9. Figure 4.10 shows the related transmission coefficient characteristics. As previously mentioned, the insertion loss is mainly determined from the frequency difference between the resonances of the orthogonal polarized waves. When the design conditions are satisfied, as the distance between the inner and the outer rings are more for the OS-SRR, the resonances for the orthogonal polarized

waves are more apart from each other which causes $T_x$ and $T_y$ intersect at a greater insertion loss.

Table 4.9      Dimensions of the SRR unit cells.

| | IS-SRR | OS-SRR |
|---|---|---|
| Operating Frequency (GHz) | 8.37 | 8.96 |
| Split length (mm) | 0.5 | 0.25 |
| Ring width (mm) | 4.8 – 4.08 (outer ring) | 4.27 – 3.77 (outer ring) |
| | 3.54 – 2.82 (inner ring) | 2.85 – 2.35 (inner ring) |
| Substrate thickness (mm) | 6.4 | 2.65 |
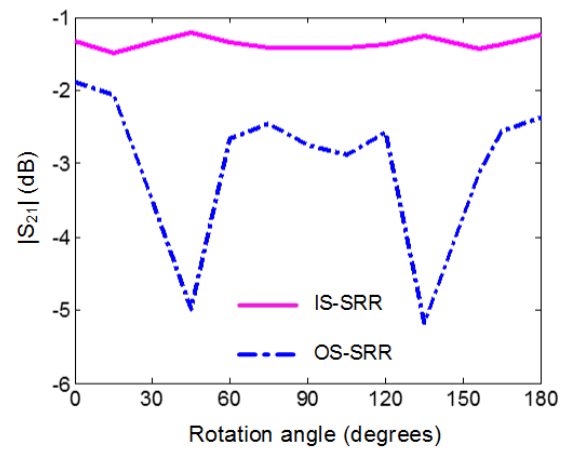


Figure 4.10      Circularly polarized transmission coefficients of the SRR unit cells.

## 4.3. Conclusion

The symmetrical geometry has effects on the insertion loss with respect to the rotation angle and this situation is demonstrated for CSRR and SRR-based transmitarray unit cells. The unsymmetrical geometry increases the cross-polarized scattering, which in turn increases the insertion loss variation with respect to the rotation. For unsymmetrical SRR structures, if the resonance is mainly provided by the symmetrical part of a unit cell, element rotation does not adversely affect the insertion loss at that frequency. Although this point is demonstrated only for some SRR-based transmitarrays, it is considered that this approach can be generalized for all structures in the implementation of the element rotation method. This study can be useful in determining the scan blindness conditions due to the increase on the insertion loss, at the design stage of the unit cell and proposes a methodology to increase the transmission magnitude for CSRR and SRR-based transmitarray unit cells.

# CHAPTER V

# FABRICATION AND MEASUREMENT

## 5.1.    Introduction

This chapter presents the fabrication process used to manufacture the designed unit cell structures, the measurement results, and the comparison between the simulation and measurement results. The fabrication processes have been completed in the clean room located at the Department of Electrical and Electronics Engineering at METU[1].

## 5.2.    Fabrication

### 5.2.1.  Process Flow

Figure 5.1 shows the fabrication process of the microfluidic transmitarray unit cell. The microfluidic channels are formed by utilizing soft lithography techniques by using a DRIE-etched (deep reactive ion etching) silicon mold wafer for shaping the PDMS (Figure 5.1 (a, b)).  In order to alleviate the adhesion of PDMS to the DRIE-etched

---

[1] The researchers involved in the fabrication processes are Dr. Özge Zorlu and Nasim Seyedpour Esmaeilzad.

silicon mold wafer, a release layer as a mixture of a detergent and ethanol in a ratio of 1:10 is spread on the mold layer. PDMS is prepared by stirring an elastomer and a curing agent, in a ratio of 10:1, approximately 20 minutes. PDMS is poured on the mold wafer and cured at room temperature for 48 hours. After peeling off the PDMS layer from the mold wafer, PDMS pieces are bonded on glass pieces (Figure 5.1 (c)). Prior to bonding process, glass samples are cleaned in acetone. PDMS-glass bonding is performed by applying oxygen plasma to the PDMS piece for 20 s at 30 mT pressure. Then, the bond is sealed by baking the bonded pieces on a hot plate at 120°C for 20 minutes. The liquid metal [64], is injected into the channel in order to form the outer ring and the inner split ring of the single layer structure (Figure 5.1 (d)).
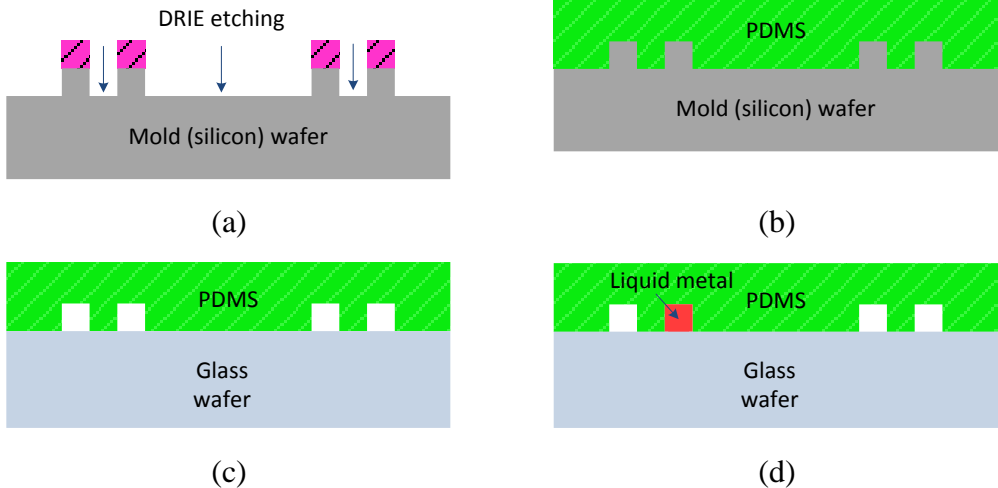


Figure 5.1    Fabrication process flow: (a) mold wafer preparation via DRIE process, (b) PDMS coating, curing, and peeling off, (c) PDMS-to-glass bonding process, and (d) Liquid metal injection.

The fabrication of CSRR unit cells is similar but there are additional process steps. As there is a metal layer on CSRR structures, this antenna metal is patterned on a glass

wafer as shown in Figure 5.2 (a) – (c) and the peeled of PDMS from the mold wafer is bonded to this metal patterned glass wafer Figure 5.2 (d).
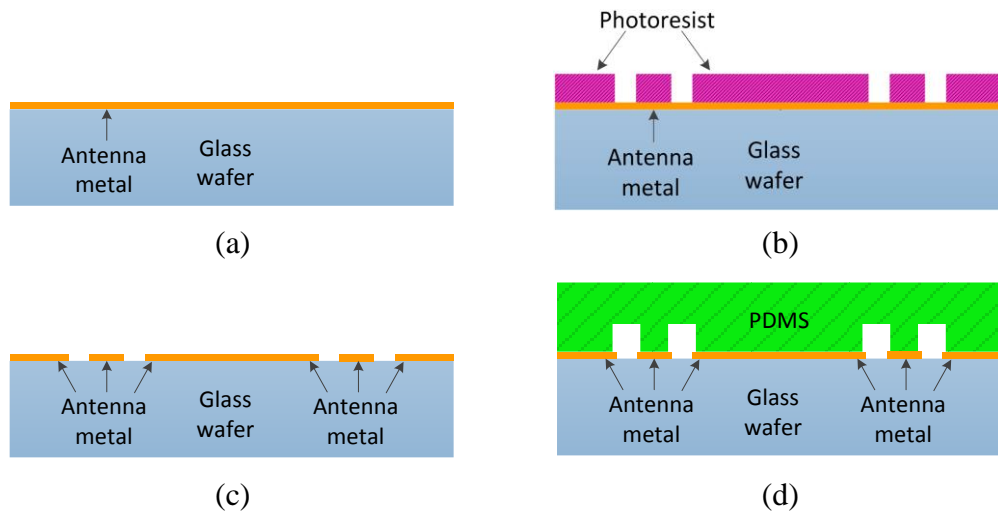


Figure 5.2      Additional steps in the fabrication process for CSRR structures: (a) – (c) metal patternization on glass wafer, (d) PDMS-to-metal bonding process.

The layout drawings are accomplished in the Cadence Layout Virtuoso™ tool environment. The layout drawings of the single layer of the SRR and CSRR unit cells are given in Figure 5.3 with the close up views shoving the metal extensions and zigzag type channels. As the dimension of one unit cell is half of that of WR-90 waveguide, two unit cells are adjacent in the layout in order to be able to fit into the waveguide.

## 5.2.2.  Fabricated Unit Cell

For the demonstration of the concept and the rotation of the split around the inner ring, six double layer IS-SRR unit cells having different split positions corresponding to the rotation angle of 0° - 10° - 20° - 30° - 80° - 90° are fabricated and measured. Figure

5.4 (a) shows the photograph of top layer of the fabricated unit cell for the rotation angle of 20°. Figure 5.4 (b) shows one of the six fabricated double layer transmitarray unit cells.



(a)

(b)  (c)

(d)  (e)
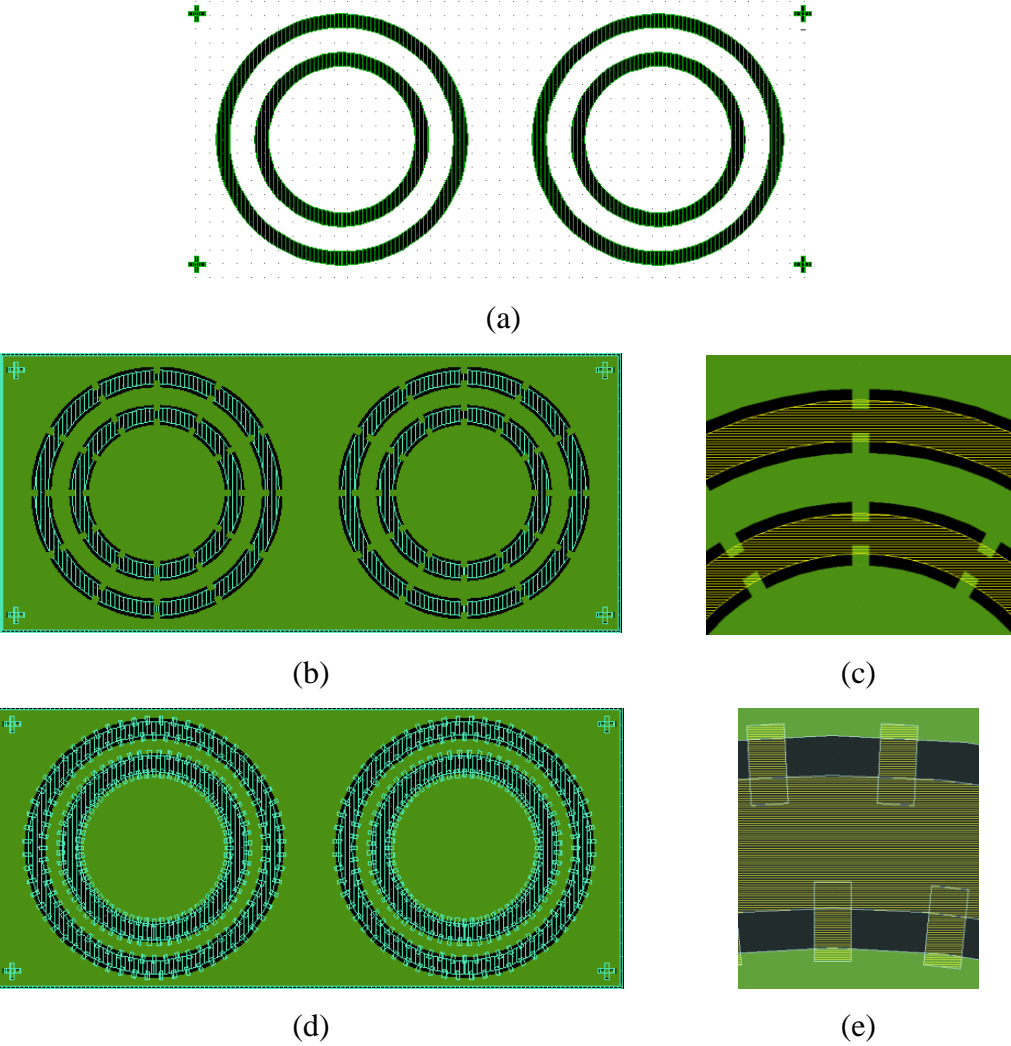
Figure 5.3    Layout drawings of the (a) SRR transmitarray unit cell, (b) CSRR transmitarray unit cell with metal extensions, (c) close up view of the metal extensions, (d) CSRR transmitarray unit cell with zigzag type channels, (e) close up view of the zigzag type channels.

(a)



(b)
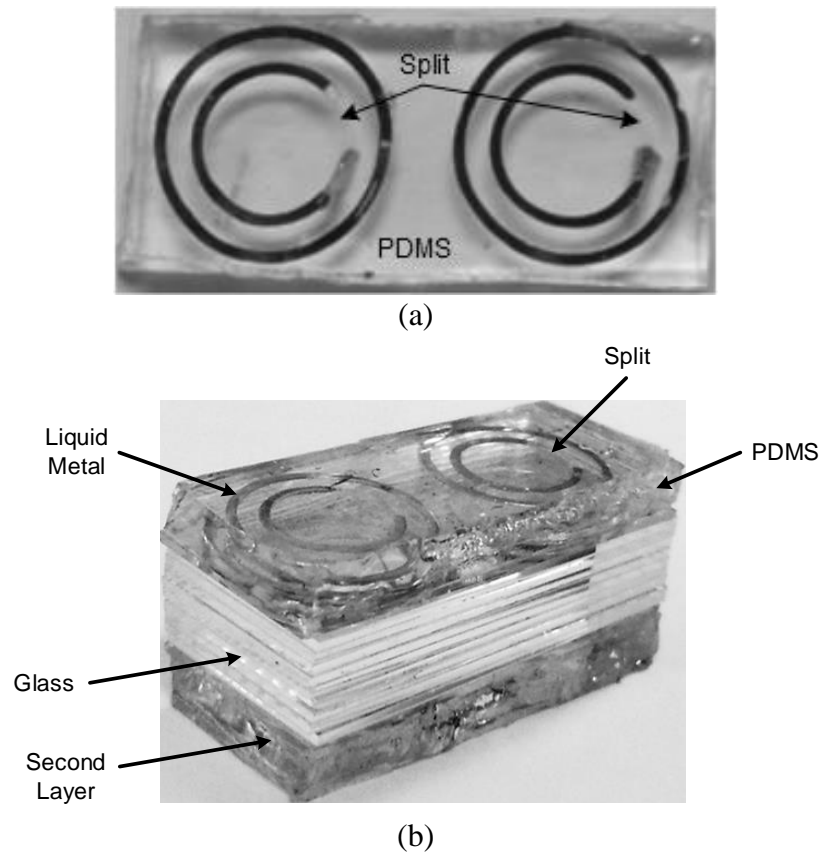
Figure 5.4    (a) Top layer of the fabricated double layer transmitarray unit cells for the rotation angle of 20°. (b) The double layer transmitarray unit cell with dimensions 22.86 mm × 10.16 mm × 9 mm.

## 5.3.    Measurement

### 5.3.1.  Measurement Setup

The fabricated unit cells are measured by using the waveguide simulator method with WR-90 waveguide [65]. The waveguide setup is given in Figure 5.5. The measurements of the unit cell are carried out using Agilent E5071C 300 kHz – 14 GHz network analyzer. Test port cables are connected to the Americon 3000-6254, 8.2 –

12.4 GHz adapters via BNC connectors. TRL (Thru, Reflect, Line) calibration is employed in order to move the measurement planes to the unit cell plane, which is placed into a WR-90 waveguide piece. 41.7 ps offset delay is used as the thru standard of during the calibration.

It should be noted that the sample is excited by a single linearly polarized wave $TE_{10}$ mode, since the components for circular polarization excitation as given in [73] are not available in our laboratory. To verify the measurement results, in the simulation environment, two adjacent unit cells are placed inside a waveguide with boundaries being perfect electric conductor and excited with the fundamental mode modeling the WR-90 environment.

It should also be noted that linear phase shifting cannot be observed from the linearly polarized measurements. Even a second set of cells with a 90° of split positioning difference are produced to combine two linearly polarized measurements, a circularly polarized performance cannot be obtained. This is mainly due to the dependency of the circularly-polarized S-parameters on the linearly-polarized cross-pol reflection and transmission components.

As mentioned in Chapter 2, the relation between the incident, $a$, and scattered, $b$, wave modes can be written in terms of S-parameters as

$$
\begin{bmatrix} b_1^x \\ b_1^y \\ b_2^x \\ b_2^y \end{bmatrix} = \begin{bmatrix} s_{11}^{xx} & s_{11}^{xy} & s_{12}^{xx} & s_{12}^{xy} \\ s_{11}^{yx} & s_{11}^{yy} & s_{12}^{yx} & s_{12}^{yy} \\ s_{21}^{xx} & s_{21}^{xy} & s_{22}^{xx} & s_{22}^{xy} \\ s_{21}^{yx} & s_{21}^{yy} & s_{22}^{yx} & s_{22}^{yy} \end{bmatrix} \begin{bmatrix} a_1^x \\ a_1^y \\ a_2^x \\ a_2^y \end{bmatrix} \tag{5.1}
$$

where the subscripts and superscripts of $a$ and $b$ represent the number of the Floquet port and the direction of polarization, respectively.

In this scattering matrix, the terms with dissimilar superscripts (i.e., $s_{11}^{xy}$, or $s_{12}^{xy}$) cannot be obtained by single linear-polarized measurement setup. Only 8 of 16 components in the S-matrix are obtained from linearly polarized measurements so that, it is not possible to obtain the circularly-polarized S-parameters in (2.7) – (2.22) and observe the phase shifting.

### 5.3.2. PDMS Characteristics

In order to determine the permittivity and dielectric loss tangent of the prepared PDMS, a sample having thickness of 1.7 mm is placed in the waveguide and its reflection and transmission coefficient characteristics are measured. Curve fitting using simulations is applied to extract the desired parameters. The simulation and measurement results are matched by varying the permittivity and dielectric loss tangent values of a material having the same thickness value and placed inside a waveguide shaped object with boundaries being perfect electric conductor in the simulation environment. The measurement results together with the simulation results are given in Figure 5.6. The measurement results shows a good agreement with the simulation results when the parameters for PDMS is set to be $\varepsilon_r$ = 2.77 and *tan δ* = 0.0127. These values are used in PDMS properties both in designing the unit cell structures and in the simulations done for the comparison with the measurements.

Network
Analyzer

Test port cables

BNC connectors

Adapters

WR-90 waveguide
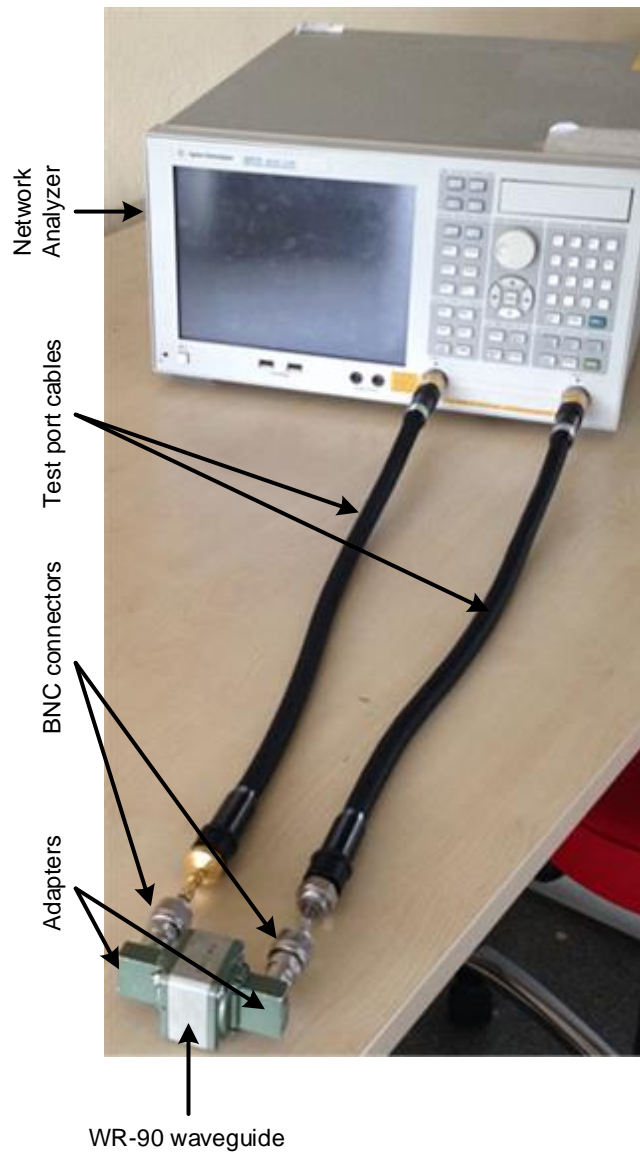
Figure 5.5        The measurement setup.
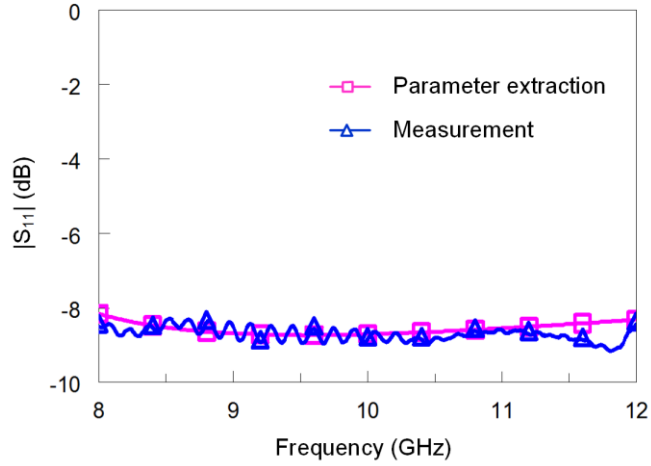
(a)
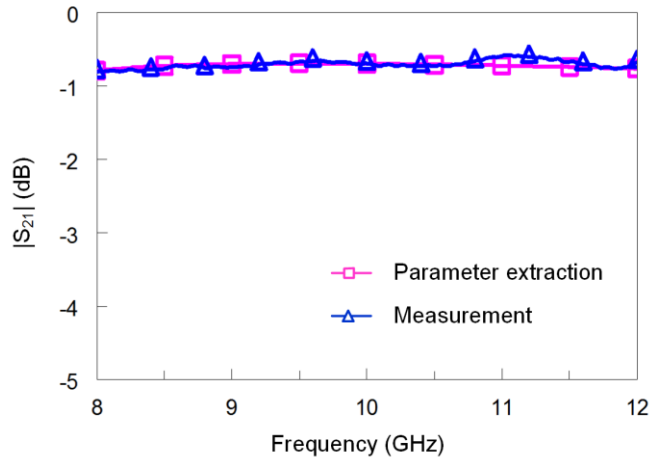


(b)

Figure 5.6    Comparison of the measurement and simulation results of the PDMS sample. (a) Reflection, (b) transmission coefficient characteristics.

### 5.3.3.  Measurement of the Fabricated Unit Cells

Figure 5.7 (a) shows one of the measured double layer samples in the WR-90 waveguide. Double layer is formed by stacking two single layer structures back to back (glass sides facing each other) with 9 other glass pieces in between, each having 0.5

mm thickness. Figure 5.7 (b) shows the measurement environment including the sample in the waveguide.
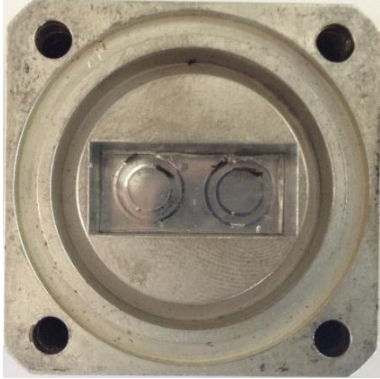


(a)



(b)

Figure 5.7     (a) One of the measured double layer samples in the WR-90 waveguide. (b) The measurement environment including the sample in the waveguide.

Figure 5.8 (a) – (l) presents the comparison of the measured and simulated transmission coefficient characteristics and the insertion phase at 8-10 GHz. It is seen that there is a reasonable agreement between the simulations and measurements. Since the liquid metal is injected inside the channels manually in these measurements, the angular positions of the splits of each IS-SRR structure may slightly differ from each

other. This situation is analyzed in Section 3.2.4 and it is demonstrated that the angular position of the split affects the insertion loss value which mainly causes the mismatch between the measurement and simulation characteristics shown in the figure below.
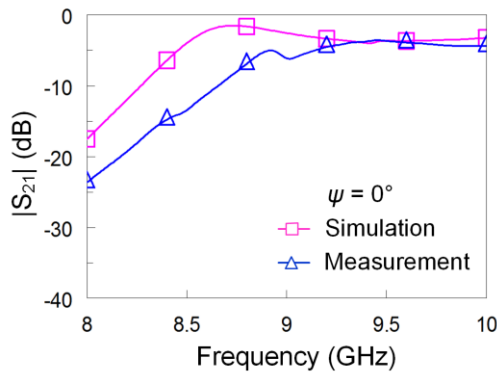


(a)
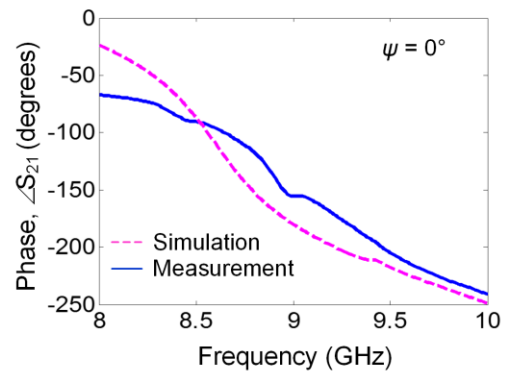
(b)
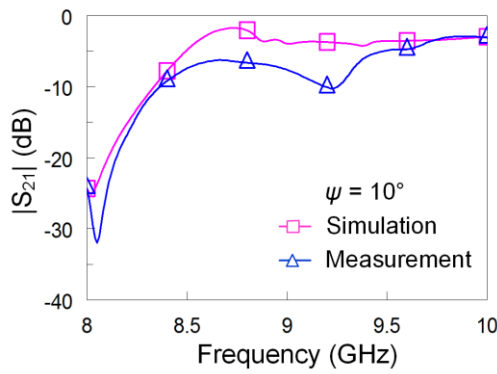
(c)
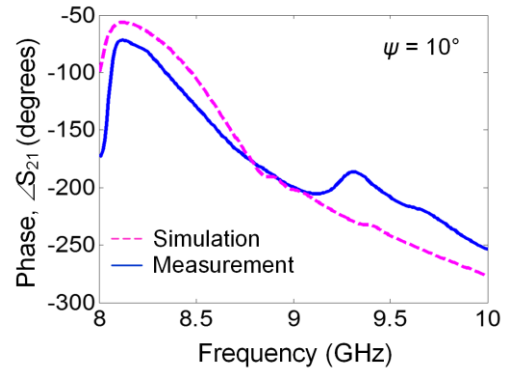
(d)
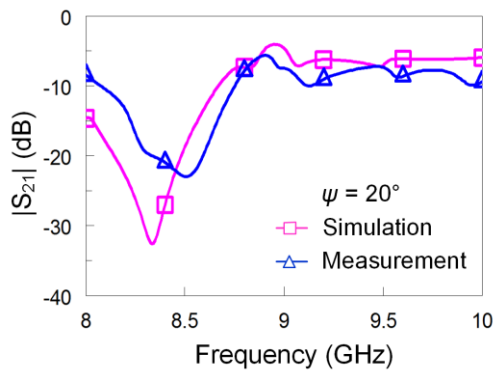
(e)
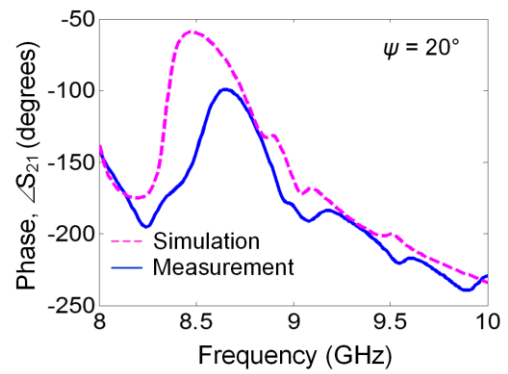
(f)
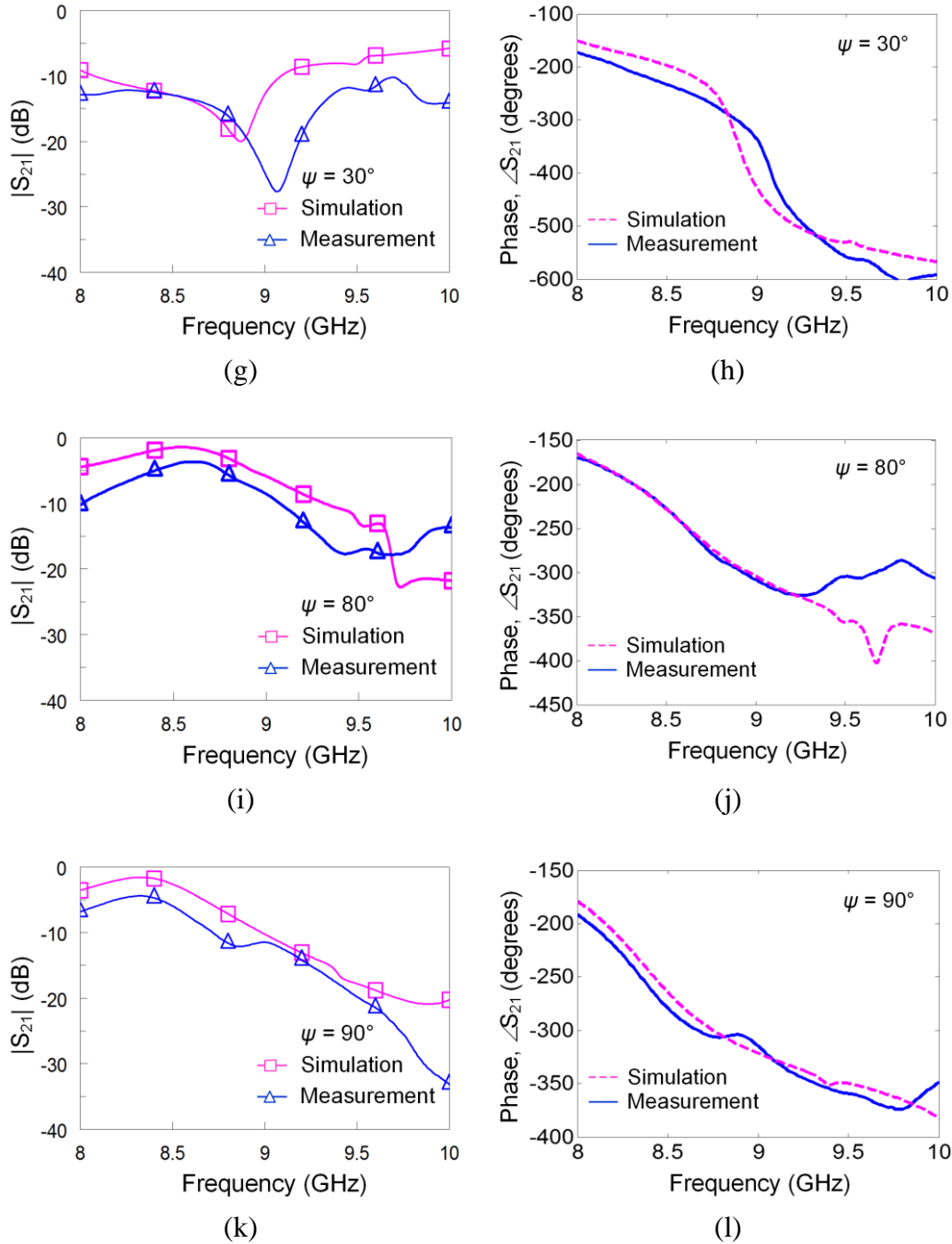
Figure 5.8    (a) – (l) Comparison of the measurement and simulation results for the transmission coefficient characteristics and insertion phase of the fabricated double layer transmitarray unit cells rotated at 0° - 10° - 20° - 30° - 80° - 90°. The corresponding rotation angle, ψ, for each figure is indicated at the inset in the figures.

It can be noticed from Figure 5.8 that phases of the measured and simulated $S_{21}$ are very close to each other at the design frequency. It should also be noted that, as mentioned before, the use of linearly polarized excitation instead of circularly polarized one that the element rotation method requires, prevents the observation of linear phase shifting corresponding to the change in the rotation angle. However, the agreement between the simulations and measurements even for linearly polarized excitation gives a robust idea about the proper operation of the design.

It can also be observed from plots in Figure 5.8 that, the insertion loss value at the design frequency is varying with the rotation angle. This variation is due to the fact that the measurement and simulation results shown in the plots are obtained for the unit cell under the linear polarized incidence. This situation can be explained as follows:

The relation between the incident and scattered waves for single polarized excitation is

$$\begin{bmatrix} b_1 \\ b_2 \end{bmatrix} = \begin{bmatrix} S_{11} & S_{12} \\ S_{21} & S_{22} \end{bmatrix} \begin{bmatrix} a_1 \\ a_2 \end{bmatrix} \tag{5.2}$$

where *a* and *b* represent the incident and scattered waves and the subscripts of *a* and *b* represent the port numbers. When the element is rotated, the rotated scattering matrix is,

$$S_\psi^{XY} = [R_\psi^{XY}]^{-1} [S^{XY}] [R_\psi^{XY}] \tag{5.3}$$

where the rotation matrix for a two port system is defined as,

$$R_\psi^{XY} = \begin{bmatrix} \cos \psi & \sin \psi \\ -\sin \psi & \cos \psi \end{bmatrix}. \tag{5.4}$$

From the rotated S-matrix, we can obtain the transmission coefficient, by taking $s_{12} = s_{21}$, as,

$$S_{\psi 21}^{XY} = s_{21} - 2s_{21} \sin^2 \psi + \frac{s_{11} - s_{22}}{2} \sin 2\psi \tag{5.5}$$

Since $s_{11} = s_{22}$ for a double layer structure with identical layers,

$$S_{\psi 21}^{XY} = s_{21} - 2s_{21} \sin^2 \psi \tag{5.6}$$

or

$$S_{\psi 21}^{XY} = s_{21} \cos 2\psi \tag{5.7}$$

From (5.7), it can be deduced that the magnitude of the transmission coefficient changes with the rotation angle for a linear polarized measurement. Therefore, the insertion loss is increasing when the rotation angle increases up to 45°, and decreasing with further increment in the rotation angle. The amplitude taper of the TE$_{10}$ incidence has also an effect on the value of the insertion loss as the rotation angle changes. Besides, the incidence angle of TE$_{10}$ excitation is 42° for a WR-90 waveguide at 8.8 GHz, which also has an effect on the insertion loss level as demonstrated in Figure 3.26 for a circularly polarized wave, $S_{21}^{rl}$.

It can also be deduced from the plots that, at the design frequency, the difference in the insertion phase is less significant than the difference in the transmission magnitude for the simulation and measurement results for the corresponding rotation angles. As analyzed in Section 3.2.4 that the insertion phase is less sensitive to misalignment than the magnitude. This situation is also related to the above derivation about the linearly polarized excitation. The change in the angular positions of the splits between the layers due to the fabrication errors affects the magnitude of the linearly polarized components ($T_x$ and $T_y$).

The measurement results show that the structure can be employed as a unit cell of a transmitarray. In the realization of the full transmitarray, a non-conductive microfluidic feed network without deteriorating the electromagnetic characteristics of the structure can be implemented as shown in Figure 5.9 (a). This network can be used to insert the liquid metal into the channel and to provide the control of the split position by utilizing micropumps attached to the ports, shown in Figure 5.9 (b), at the ends of the channels by tubes. The location of the conductive fluid can be dynamically adjusted by applying air pressure or by moving the liquid metal droplets inside a fluidic medium showing dielectric properties with micropumps.

Although the ports in Figure 5.9 are shown to pull the air from the channels, microsamples of GaInSn compounds are oxidized very rapidly when contacted with air, which prevents its movement as a whole droplet. In the proposed design, the oxidation is a problem affecting the movement of the liquid metal along the channel. When air is injected from an injector to enable the movement it is seen that the liquid metal does not move as a whole droplet whereas it leaves traces behind. The movement of the liquid metal droplets can be provided by filling the channels by a solution preventing the oxidation of the liquid metal, such as liquid Teflon [57]. In this case, the split ring can be realized by filling the microfluidic channel by a small amount of dielectric fluid to act as the gap region in the split ring and large amount of liquid metal to act as the metallic ring.

For pulling the air in
the channels

For injecting the
liquid metal

Micropump network

Tubes

(a)



Ports for injecting
the liquid metal

Microfluidic
channels

Ports for pulling the
air in the channels
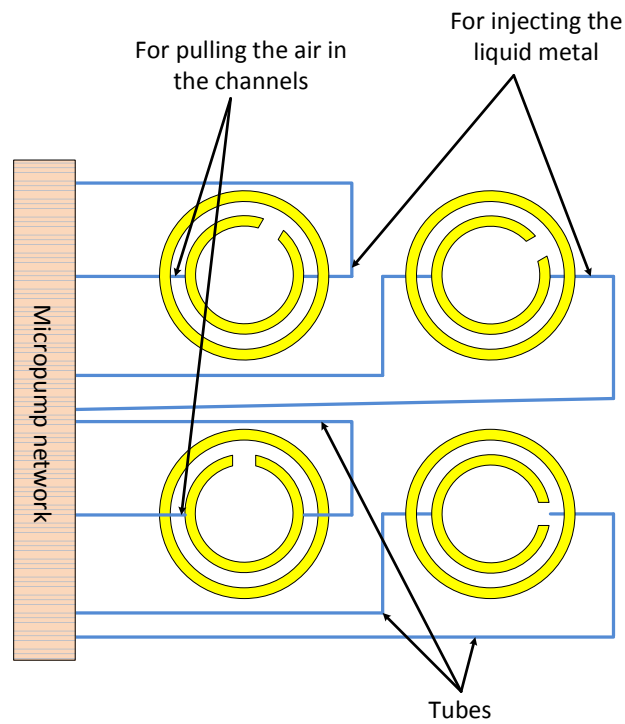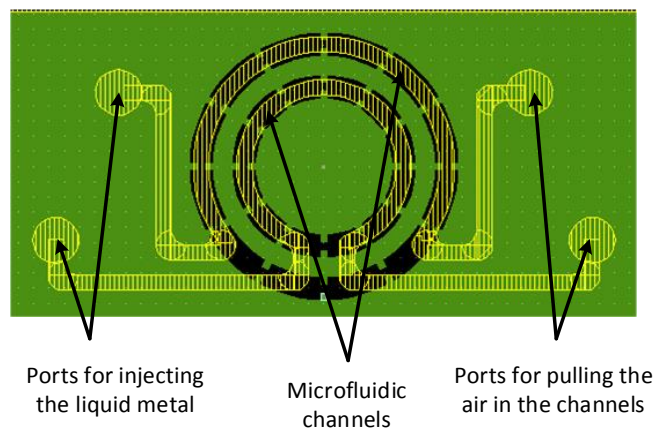
(b)

Figure 5.9 (a) A non-conductive microfluidic feed network injecting liquid metal and controlling the position of the splits to realize a transmitarray. (b) Layout of a unit cell with ports attached for the integration of micropumps to inject the liquid metal and pull the air from the channels.

# CHAPTER VI

# CONCLUSION AND FUTURE WORKS

## 6.1.    Conclusions

In this thesis, novel microfluidic based reconfigurable transmitarray unit cells employing the element rotation method is presented. The unit cells consist of double layer split rings implemented as microfluidic channels inside the PDMS layer. An alloy of 68.5% Ga, 21.5% In, and 10% Sn is injected as liquid metal in the channels forming the conductive parts in the structure. The split region is the empty region in the channel filled with the liquid metal in SRR type structures whereas it is formed by the liquid metal in CSRR type structures. The rotation of the unit cell is provided by the movement of the liquid metal around the rings. The control of the phase of the transmitted wave is accomplished by this rotation providing linear and continuous phase shifting in 0°–360° range.

A generalized formulation for the implementation of the element rotation method is derived. From this derivation, the necessary conditions for achieving linear phase shift is determined and the design is optimized at 8.8 GHz to satisfy these conditions. This optimization methodology is based on changing the characteristic impedance of the unit cell for the orthogonal polarized wave modes to achieve different resonance frequencies for those wave modes. This difference in the resonance frequencies is used in adjusting the necessary phase difference. The phase difference is adjusted by parametric analysis and the effect of the parameters on the resonances and phase

difference are presented by taking into account a circuit model perspective. The designed unit cells are fabricated in the facilities of METU. The characterization of the fabricated unit cells are carried out by using the waveguide simulator method. The simulation and measurement results show a fair agreement.

The advantages of the proposed method and the unit cell over the current technology can be summarized as follows:

- The major advantage is 0°–360° continuous and linear phase shifting capability, without using any additional phase shifting mechanism and without increasing the size of the unit cell.

- Another advantage of the proposed reconfigurable unit cell structure is that each unit cell can be controlled by a pair of tubes connected to a micropump whereas, in the realization of 2D beam steering transmitarrays by switches, varactors and phase shifters, each such component of each unit cell should be controlled individually which may require even more complicated biasing network.

- The design can be easily scaled to different frequency bands since the structure and the channels are manufactured by using micromachining techniques that enable the high precision fabrication capability required for high frequency applications.

- The use of microfabrication techniques and the utilization of passive materials in the structure allow the implementation of cost-effective antenna arrays.

- A microfluidically enabled transmitarray is suitable for high power microwave applications since the method uses passive materials with linear RF characteristics.

Another contribution of the thesis is the demonstration of the effect of the geometrical symmetry on the insertion loss for CSRR and SRR-based transmitarray unit cells. The symmetrical geometry decreases the cross-polarized scattering, which in turn decreases the insertion loss variation with respect to the rotation. It is also shown for unsymmetrical SRR structures that if the resonance is mainly provided by the symmetrical part of a unit cell, element rotation does not adversely affect the insertion loss at that frequency. This contribution is useful in determining the scan blindness conditions due to the increase on the insertion loss at the design stage of the unit cell. It also proposes a methodology to increase the transmission magnitude for SRR and CSRR-based transmitarray unit cells.

## 6.2.    Future Works

This thesis study shows that the microfluidics is suitable for the implementation of the element rotation method in transmitarrays. As the use of microfluidics in antenna engineering applications is quite new, there exists a huge amount of subjects to be investigated in this area. The possible investigation fields related to the context of this thesis can be summarized as follows:

- The manual insertion of the liquid metal into the channels may cause misalignments of the splits both in position and length resulting in a slight phase difference between the measured and transmitted fields. The use of micropumps with high precision control can solve this problem.

- The experience gained in the design, fabrication, and measurement of the microfluidic based transmitarray unit cell and the satisfactory results show that the methodology can be applied to design and fabricate a reconfigurable transmitarray. The beam of the transmitarray can be steered in 2D when the

location of the conductive fluid for each element in the array is controlled dynamically.

- In the realization of the transmitarray, a non-conductive microfluidic feed network and micropumps can be used to inject and control the position of the liquid metal as suggested in Chapter 5.

- To prevent the oxidation problem of microsamples of GaInSn compounds, liquid Teflon solution can be used inside the channels instead of air as to form the splits as mentioned in Chapter 5.

- The proposed methodology can be easily implemented on reflectarray structures and a microfluidic based reconfigurable reflectarray implementing the element rotation method as phase control mechanism can be designed, fabricated and measured.

As a result, implementing microfluidics in antenna engineering offers opportunities alleviating the limitations of other approaches. Being a new research area, the achievements on this area will lead investigations on new researches and development of novel techniques. With this thesis, the microfluidic based antenna applications are initialized in Turkey and it is believed that this thesis will be encouraging for the studies on this promising technology.

# REFERENCES

[1]     J. Huang and J. A. Encinar, Reflectarray Antennas. Hoboken, NJ: Wiley, 2008.

[2]     A. Abbaspour-Tamijani, K. Sarabandi, and G.M. Rebeiz, "A millimetre-wave bandpass filter-lens array," *IET Microwaves, Antennas & Propagation*, vol.1, no.2, pp.388-395, April 2007.

[3]     C. Chih-Chieh and A. Abbaspour-Tamijani, "Study of 2-bit antenna–filter–antenna elements for reconfigurable millimeter-wave lens arrays," *IEEE Trans. Microwave Theory and Tech.*, vol.54, no.12, pp.4498-4506, Dec. 2006.

[4]     D. M. Pozar, "Flat lens antenna concept using aperture coupled microstrip patches," *Electron. Lett.*, vol. 32, no. 23, pp. 2109-2111, Nov. 1996.

[5]     B. A. Munk, Frequency Selective Surfaces—Theory and Design. New York: Wiley, 2000.

[6]     J.Y. Lau and S.V. Hum, "Reconfigurable transmitarray design approaches for beamforming applications," *IEEE Trans. Antennas Propag.*, vol.60, no.12, pp.5679-5689, Dec. 2012.

[7]     R. H. Phillion and M. Okoniewski, "Lenses for circular polarization using planar arrays of rotated passive elements," *IEEE Trans. Antennas Propag.*, vol.59, no.4, pp.1217-1227, April 2011.

[8]     D. McGrath, "Planar three-dimensional constrained lenses," *IEEE Trans. Antennas Propag.*, Vol. 34, pp. 46-50, Jan. 1986.

[9]     C.G.M. Ryan, M.R. Chaharmir, J. Shaker, J.R. Bray, Y.M.M. Antar, and A. Ittipiboon, "A wideband transmitarray using dual-resonant double square rings," *IEEE Trans. Antennas Propag.*, vol.58, no.5, pp.1486-1493, May 2010.

[10]     P. Torre and M. Sierra-Castaner, "Design and prototype of a 12GHz transmitarray," *Microwave and Technology Letters*, Vol. 49, No.12, pp. 3020-3026, Dec. 2007.

[11]     H. Kaouach, L. Dussopt, R. Sauleau, and T. Koleck, "Design and demonstration of an X-band transmit-array," *3ʳᵈ European Conference on Antennas and Propagation (EuCAP)*, pp.1191-1195, 23-27 March 2009.

[12]     M.B. Perotoni, S. Rondineau, R. Lee, D. Consonni, and Z. Popovic, "X-band discrete lens array for a satellite communication ground station antenna," *SBMO/IEEE MTT-S International Conference on Microwave and Optoelectronics*, pp. 197- 200, 25-28 July 2005.

[13]     J. Mazotta, L.-Y. Chen, and J.-C. Chiao, "Reconfigurable transmission-type beamformer," *IEEE MTT-S International Microwave Symposium Digest*, vol.1, pp.585-588, 2000.

[14]     A. Clemente, L. Dussopt, R. Sauleau, P. Potier, and P. Pouliguen, "Wideband 400-element electronically reconfigurable transmitarray in X band," *IEEE Trans. Antennas Propag.*, vol.61, no.10, pp.5017-5027, Oct. 2013.

[15]     C. Chih-Chieh, B. Lakshminarayanan, and A. Abbaspour-Tamijani, "A programmable lens-array antenna with monolithically integrated MEMS switches," *IEEE Trans. Microwave Theory and Tech.*, vol.57, no.8, pp.1874-1884, Aug. 2009.

[16]     J.Y. Lau and S.V. Hum, "A planar reconfigurable aperture with lens and reflectarray modes of operation," *IEEE Trans. Microwave Theory Tech.*, vol.58, no.12, pp.3547-3555, Dec. 2010.

[17]     M. Sazegar, Z. Yuliang, C. Kohler, H. Maune, M. Nikfalazar, J.R. Binder, R. Jakoby, "Beam steering transmitarray using tunable frequency selective surface with integrated ferroelectric varactors," *IEEE Trans. Antennas Propag.*, vol.60, no.12, pp.5690-5699, Dec. 2012.

[18]     P. Padilla, A. Muñoz-Acevedo, M. Sierra-Castañer, and M. Sierra-Pérez, "Electronically reconfigurable transmitarray at Ku band for microwave

applications," *IEEE Trans. Antennas Propag.*, vol.58, no.8, pp.2571-2579, Aug. 2010.

[19]    J.Y. Lau and S.V. Hum, "A wideband reconfigurable transmitarray element," *IEEE Trans. Antennas Propag.*, vol.60, no.3, pp.1303-1311, Mar. 2012.

[20]    M. Euler and V. F. Fusco, "Frequency selective surface using nested split ring slot elements as a lens with mechanically reconfigurable beam steering capability," *IEEE Trans. Antennas Propag.*, vol.58, no.10, pp.3417-3421, Oct. 2010.

[21]    J. Huang and R. J. Pogorzelski, "A Ka-band microstrip reflectarray with elements having variable rotation angles," *IEEE Trans. Antennas Propag.*, vol.46, no.5, pp.650-656, May 1998.

[22]    R. H. Phillion and M. Okoniewski, "Improving the phase resolution of a micromotor-actuated phased reflectarray," *Microsystems and Nanoelectronics Research Conference (MNRC)*, pp. 169–172, 2008.

[23]    C. Guclu, J. Perruisseau-Carrier, and O. Aydin Civi, "Proof of concept of a dual-band circularly-polarized RF MEMS beam-switching reflectarray," *IEEE Trans. Antennas Propag*, vol.60, no.11, pp. 5451-5455, Nov. 2012.

[24]    A. E. Martynyuk, J. I. Martinez Lopez, and N. A. Martynyuk, "Spiraphase-type reflectarrays based on loaded ring slot resonators," *IEEE Trans. Antennas Propag.*, vol.52, no.1, pp. 142–153, 2004.

[25]    M.E. Bialkowski and H.J. Song, "A Ku-band active transmit-array module with a horn or patch array as a signal launching/receiving device," *IEEE Trans. Antennas Propag.*, vol.49, no.4, pp.535-541, Apr. 2001.

[26]    F.-C.E. Tsai and M.E. Bialkowski, "Investigations into the design of a spatial power combiner employing a planar transmitarray of stacked patch antennas," *15th International Conference on Microwaves, Radar and Wireless Communications (MIKON-2004)*, vol.2, pp. 509- 512, 17-19 May 2004.

[27]  H.L. Sun and W.X. Zhang, "Design of broadband element of transmit-array with polarization transform," *International Workshop on Antenna Technology: Small and Smart Antennas Metamaterials and Applications (IWAT '07),* pp.287-290, 21-23 March 2007.

[28]  G.M. Whitesides, "The origins and the future of microfluidics", *Nature*, vol.442, pp.368-373, Jul. 2006.

[29]  K. Bonghwan, "Electrostatically driven micropump with peristaltically moving membrane," *IET Micro & Nano Letters*, vol.8, no.10, pp.654-658, Oct. 2013.

[30]  P. Galambos, J. Lantz, M.S. Baker, J. McClain, G.R. Bogart, and R.J. Simonson, "Active MEMS valves for flow control in a high-pressure micro-gas-analyzer," *Journal of Microelectromechanical Systems*, vol.20, no.5, pp.1150-1162, Oct. 2011.

[31]  M.J. de Boer, R.W. Tjerkstra, J.W. Berenschot, H.V. Jansen, G.J. Burger, J.G.E. Gardeniers, M. Elwenspoek, and A. Van den Berg, "Micromachining of buried micro channels in silicon," *Journal of Microelectromechanical Systems*, vol.9, no.1, pp.94,103, Mar. 2000.

[32]  H. Qiaohong, L. Hua, C. Shuang, and C. Hengwu, "Fabrication of full glass chips with hybrid micro- and nanochannels and their application to protein concentration," *IEEE International Conference on Nano/Molecular Medicine and Engineering (NANOMED)*, pp.44,47, 18-21 Oct. 2009.

[33]  J. Youngsman, B. Marx, M. Schimpf, S. Wolter, J. Glass, and A. Moll, "Low temperature co-fired ceramics for micro-fluidics," *56th Electronic Components and Technology Conference Proceedings*, pp.699-704. 2006

[34]  E.J. Geiger, A.P. Pisano, and F. Svec, "A polymer-based microfluidic platform featuring on-chip actuated hydrogel valves for disposable applications," *Journal of Microelectromechanical Systems*, vol.19, no.4, pp.944-950, Aug. 2010.

[35]    N. N. Pamela, I. R. Chad, and A. T. Woolley, "Advances in microfluidic materials, functions, integration, and applications", *Chemical Reviews*, 113 (4), pp.2550-2583, 2013.

[36]    N.J. Farcich, J. Salonen, and P.M. Asbeck, "Single-length method used to determine the dielectric constant of polydimethylsiloxane," *IEEE Trans. Microwave Theory and Tech.*, vol.56, no.12, pp.2963-2971, Dec. 2008.

[37]    H. Yi-Ling, H. Tsung-Yi, and K. Chakrabarty, "On-chip biochemical sample preparation using digital microfluidics," *IEEE Biomedical Circuits and Systems Conference (BioCAS)*, pp.297-300, 10-12 Nov. 2011.

[38]    H. Qing, P. Changlin, T. Yu-Chong, and T.D. Lee, "Ion liquid chromatography on-a-chip with beads-packed parylene column," *17th IEEE International Conference on Micro Electro Mechanical Systems, (MEMS),* vol., no., pp.212-215, 2004.

[39]    W. Li, D.M. Sipe, X. Yong, and Q. Lin, "A MEMS thermal biosensor for metabolic monitoring applications," *Journal of Microelectromechanical Systems*, vol.17, no.2, pp.318-327, Apr. 2008.

[40]    P.J. Lee, P.J. Hung, and L.P. Lee, "Microfluidic cell culture array for on-chip cell biology," *3rd IEEE/EMBS Special Topic Conference on Microtechnology in Medicine and Biology*, pp.382-384, 12-15 May 2005.

[41]    D.J. Beebe, J.D. Trumbull, and I.K. Glasgow, "Microfluidics and bioanalysis systems: issues and examples," *Proceedings of the 20th Annual International Conference of the IEEE Engineering in Medicine and Biology Society*, vol.4, pp.1692-1697, 29 Oct.-1 Nov. 1998.

[42]    T. Laksanasopin, C.D. Chin, H. Moore, J. Wang, C. K. Yuk, and S.K. Sia, "Microfluidic point-of-care diagnostics for resource-poor environments," *Annual International Conference of the IEEE Engineering in Medicine and Biology Society (EMBC)*, pp.1057-1059, 3-6 Sep. 2009.

[43]    P.S. Dittrich, and A. Manz, "Lab-on-a-chip: Microfluidics in drug discovery". *Nature Rev. Drug Discov*. 5, 210–218, 2006.

[44]  G.J. Hayes, So Ju-Hee, A. Qusba, M.D. Dickey, and G. Lazzi, "Flexible liquid metal alloy (EGaIn) microstrip patch antenna," *IEEE Trans. Antennas Propag*., vol.60, no.5, pp.2151-2156, May 2012.

[45]  A. Traille, Y. Li, A. Rida, and M. M. Tentzeris, "A novel liquid antenna for wearable bio-monitoring applications," *IEEE MTT-S International Microwave Symposium Digest,* pp.923-926, 15-20 Jun. 2008.

[46]  J.C.G. Matthews and G. Pettitt, "Development of flexible, wearable antennas," *3rd European Conference on Antennas and Propagation (EuCAP)*, pp.273-277, 23-27 Mar. 2009.

[47]  M.Kubo, Li Xiaofeng, Kim Choongik, M. Hashimoto, B.J. Wiley, Ham Donhee, and G.M. Whitesides, "Stretchable microfluidic electric circuit applied for radio frequency antenna," *IEEE 61st Electronic Components and Technology Conference (ECTC)*, pp.1582-1587, 2011.

[48]  S.J. Mazlouman, X.J. Jiang, A. Mahanfar, C. Menon, and R.G. Vaughan, "A reconfigurable patch antenna using liquid metal embedded in a silicone substrate," *IEEE Trans. Antennas Propag*., vol.59, no.12, pp.4406-4412, Dec. 2011.

[49]  A. Qusba, A.K. RamRakhyani, S. Ju-Hee, G.J. Hayes, M.D. Dickey, and G. Lazzi, "On the design of microfluidic implant coil for flexible telemetry system," *IEEE Sensors Journal*, vol.14, no.4, pp.1074-1080, Apr. 2014.

[50]  M. Rashed Khan, G.J. Hayes, J.-H. So, G. Lazzi, and M.D. Dickey, "A frequency shifting liquid metal antenna with pressure responsiveness," *Applied Physics Letters*, vol.99, no.1, pp.013501-013501-3, Jul. 2011.

[51]  A. Traille, S. Bouaziz, S. Pinon, P. Pons, H. Aubert, A. Boukabache, and M. Tentzeris, "A wireless passive RCS-based temperature sensor using liquid metal and microfluidics technologies," *41st European Microwave Conference (EuMC)*, pp.45-48, 10-13 Oct. 2011.

[52]    M. Kelley, C. Koo, H. Mcquilken, B. Lawrence, S. Li, A. Han, and G. Huff, "Frequency reconfigurable patch antenna using liquid metal as switching mechanism," *Electronics Letters* , vol.49, no.22, pp.1370-1371, Oct. 2013.

[53]    A. M. Morishita, C.K.Y. Kitamura, A.T. Ohta, and W.A. Shiroma, "A liquid-metal monopole array with tunable frequency, gain, and beam steering," *IEEE Antennas and Wireless Propagation Letters*, vol.12, pp.1388-1391, 2013.

[54]    D. Rodrigo, L. Jofre, and B.A. Cetiner, "Circular beam-steering reconfigurable antenna with liquid metal parasitics," *IEEE Trans. Antennas Propag*., vol.60, no.4, pp.1796-1802, Apr. 2012.

[55]    A.A. Gheethan, C.J. Myeong, R. Guldiken, and G. Mumcu, "Microfluidic based Ka-band beam-scanning focal plane array," *IEEE Antennas and Wireless Propagation Letters*, vol.12, pp.1638-1641, 2013.

[56]    L. Tingyi, P. Sen, and K. Chang-Jin, "Characterization of nontoxic liquid-metal alloy galinstan for applications in microdevices," *Journal of Microelectromechanical Systems*, vol.21, no.2, pp.443-450, Apr. 2012.

[57]    L. Meng and N. Behdad, "Fluidically tunable frequency selective/phase shifting surfaces for high-power microwave applications," *IEEE Trans. Antennas Propag*., vol.60, no.6, pp.2748-2759, Jun. 2012.

[58]    S.A. Long, and G.H. Huff, "A fluidic loading mechanism for phase reconfigurable reflectarray elements," *IEEE Antennas and Wireless Propagation Letters*, vol.10, pp.876-879, 2011.

[59]    G. Mumcu, A. Dey, and T. Palomo, "Frequency-agile bandpass filters using liquid metal tunable broadside coupled split ring resonators," *IEEE Microwave and Wireless Components Letters*, vol.23, no.4, pp.187-189, Apr. 2013.

[60]    ANSYS® HFSS, Version 13, Online Help, Master and Slave Boundaries.

[61]    A.K. Bhattacharyya, Phased Array Antennas: Floquet Analysis, Synthesis, BFNs, and Active Array Systems, Hoboken, NJ: Wiley, 2006.

[62]    E. Erdil, K. Topalli, O. Zorlu, T. Toral, E. Yildirim, H. Kulah, and O. Aydin Civi, "Reconfigurable Microfluidic Transmitarray Unit Cells" *14$^{th}$ Workshop on MEMS for MilimeterWave Communications (MEMSWAVE)*, Potsdam, Germany, June 2013.

[63]    E. Erdil, K. Topalli, O. Zorlu, T. Toral, E. Yildirim, H. Kulah, and O.A. Civi, "A reconfigurable microfluidic transmitarray unit cell," *7th European Conference on  Antennas and Propagation (EuCAP),* pp. 2957-2960, April 2013.

[64]    GalliumSource, LLC, www.galliumsource.com, last visited on May 2014.

[65]    P. Hannan and M. Balfour, "Simulation of a phased-array antenna in waveguide," *IEEE Trans. Antennas Propag.,* vol.13, no.3, pp. 342-353, May 1965.

[66]    S. V. Hum, J. Perruisseau-Carrier, "Reconfigurable Reflectarrays and Array Lenses for Dynamic Antenna Beam Control: A Review," *IEEE Trans. Antennas Propag.,* vol.62, no.1, pp.183-198, Jan. 2014

[67]    J. D. Baena, J. Bonache, F. Martin, R. M. Sillero, F. Falcone, T. Lopetegi, M. A. G. Laso, J. Garcia-Garcia, I. Gil, M. F. Portillo, and M. Sorolla, "Equivalent-circuit models for split-ring resonators and complementary split-ring resonators coupled to planar transmission lines," *IEEE Trans. Microwave Theory Tech*., vol.53, no.4, pp.1451-1461, Apr. 2005.

[68]    K. Aydin, I. Bulu, K. Guven, M. Kafesaki, C. M. Soukoulis, and E. Ozbay, "Investigation of magnetic resonances for different split-ring resonator parameters and designs" *New J. Phys*. 7, 168, 2005.

[69]    B. Sauviac, C. R. Simovski, and S. A. Tretyakov. "Double split-ring resonators: Analytical modeling and numerical simulations." *Electromagnetics* 24.5 (2004): 317-338.

114

[70]     E. Erdil, K. Topalli, N. S. Esmaeilzad, O. Zorlu, H. Kulah, and O.A. Civi, "A reconfigurable nested ring-split ring transmitarray unit cell by microfluidic technology," *8th European Conference on  Antennas and Propagation (EuCAP),* The Hague, Netherlands, April 2014.

[71]     E. Erdil, K. Topalli, N. S. Esmaeilzad, O. Zorlu, H. Kulah, and O. A. Civi, "Reconfigurable Nested Ring-Split Ring Transmitarray Unit Cell Employing the Element Rotation Method by Microfluidics," *submitted to IEEE Trans. Antennas Propag*.

[72]     Z. Sheng, and V.V. Varadan. "Tuning the effective properties of metamaterials by changing the substrate properties." *Journal of applied physics* 101.1 (2007): 014909.

[73]     S. Mener, R. Gillard, R. Sauleau, C. Cheymol, and P. Potier, "Design and characterization of a CPSS-based unit-cell for circularly polarized reflectarray applications," *IEEE Trans. Antennas Propag.,* vol.61, no.4, pp.2313-2318, April 2013.

# APPENDIX

# UNIT CELL CHARACTERISTICS

This chapter presents the geometries, design parameter values and the reflection, transmission coefficient and insertion phase characteristics of the designs presented in Chapter 3.

## 1.    CSRR Unit Cell with Metal Extensions

Figure A.1 shows the CSRR unit cell with metal extensions to increase the contact area between the PDMS layer and the glass layer. The design satisfies the phase shifting conditions for the parameter values shown in Table A.1. The reflection, transmission and insertion phase characteristics are shown in Figure A.2.
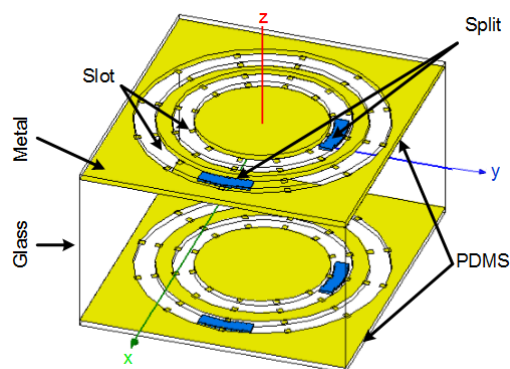


Figure A.1    Geometry of the CSRR transmitarray unit cell with metal extensions.

Table A.1    The values of the parameters of the CSRR transmitarray unit cell with metal extensions.

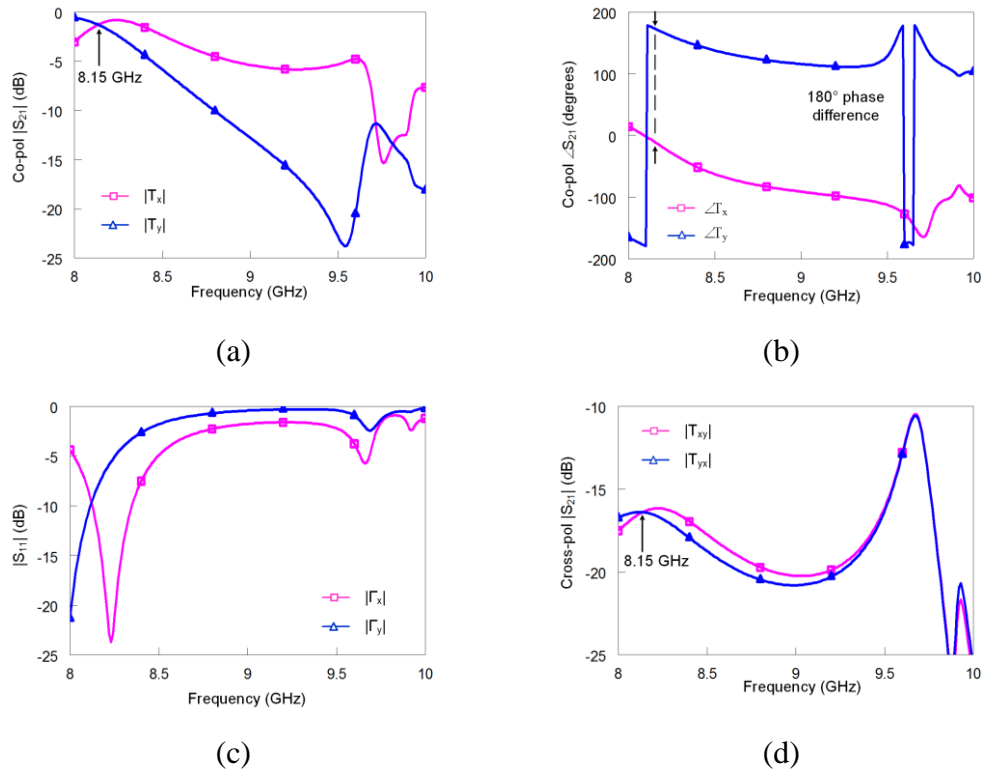| Substrate thickness | Split length | Outer ring radius | Inner ring radius |
|---|---|---|---|
| 6 mm | 2 mm | 4.7 – 3.9 mm | 3.3 – 2.5 mm |



(a)

(b)

(c)

(d)

Figure A.2    Simulated characteristics of the CSRR transmitarray unit cell with metal extensions. (a) Magnitude of the co-pol transmission coefficients, (b) phase of the co-pol transmission coefficients, (c) magnitude of the cross-pol transmission coefficients, (d) magnitude of the reflection coefficients.

## 2.     CSRR Unit Cell with Zigzag Type Channels

Figure A.3 and Table A.2 shows the CSRR unit cell with zigzag type channels and its parameter values satisfying the phase shifting conditions. The reflection, transmission and insertion phase characteristics are shown in Figure A.4.
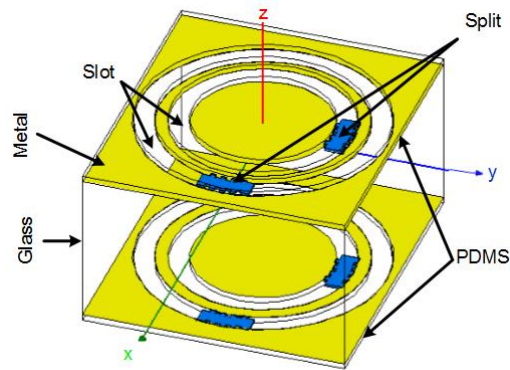


Figure A.3      Geometry of the CSRR transmitarray unit cell with zigzag type channels.

Table A.2      The values of the parameters of the CSRR transmitarray unit cell with zigzag type channels.

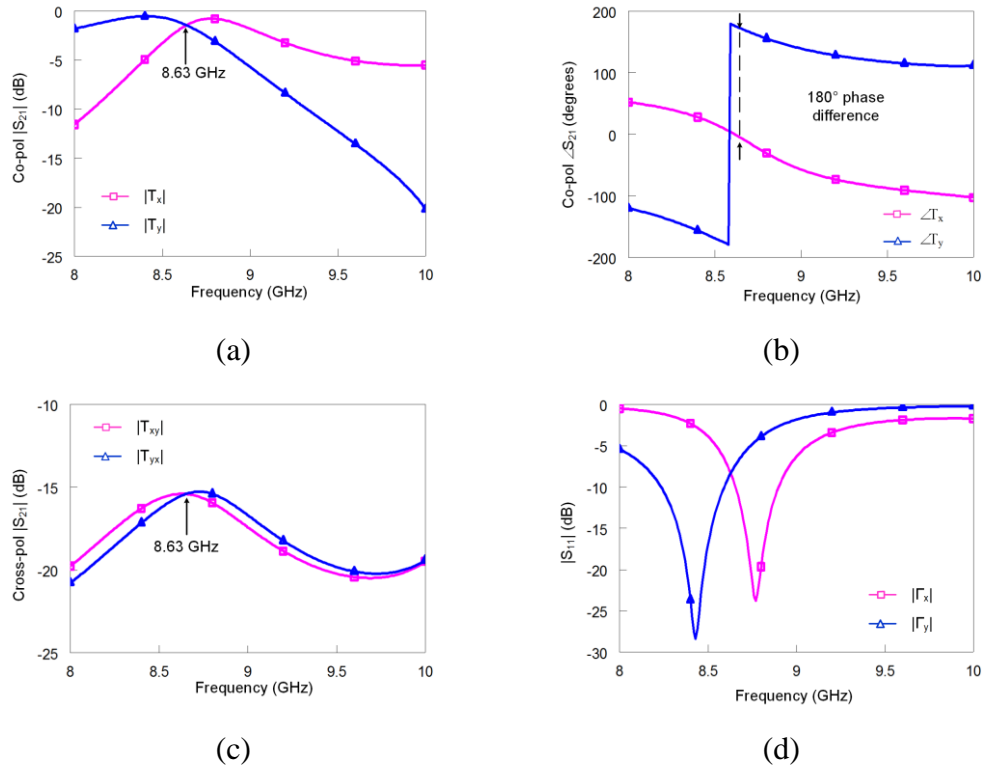| Substrate thickness | Split length | Outer ring radius | Inner ring radius |
|---|---|---|---|
| 5.5 mm | 2 mm | 4.8 – 4 mm | 3.5 – 2.7 mm |

(a)

(b)

(c)

(d)

Figure A.4    Simulated characteristics of the CSRR transmitarray unit cell with zigzag type channels. (a) Magnitude of the co-pol transmission coefficients, (b) phase of the co-pol transmission coefficients, (c) magnitude of the cross-pol transmission coefficients, (d) magnitude of the reflection coefficients.

# 3.     OS-SRR Unit Cell

Figure A.5 shows the OS-SRR unit cell geometry and the design parameters are given in Table A.3. The reflection, transmission and insertion phase characteristics are shown in Figure A.6.
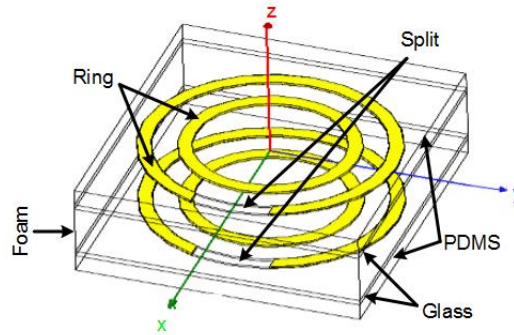


Figure A.5      Geometry of the OS-SRR transmitarray unit cell.

Table A.3      The values of the parameters of the OS-SRR transmitarray unit cell.

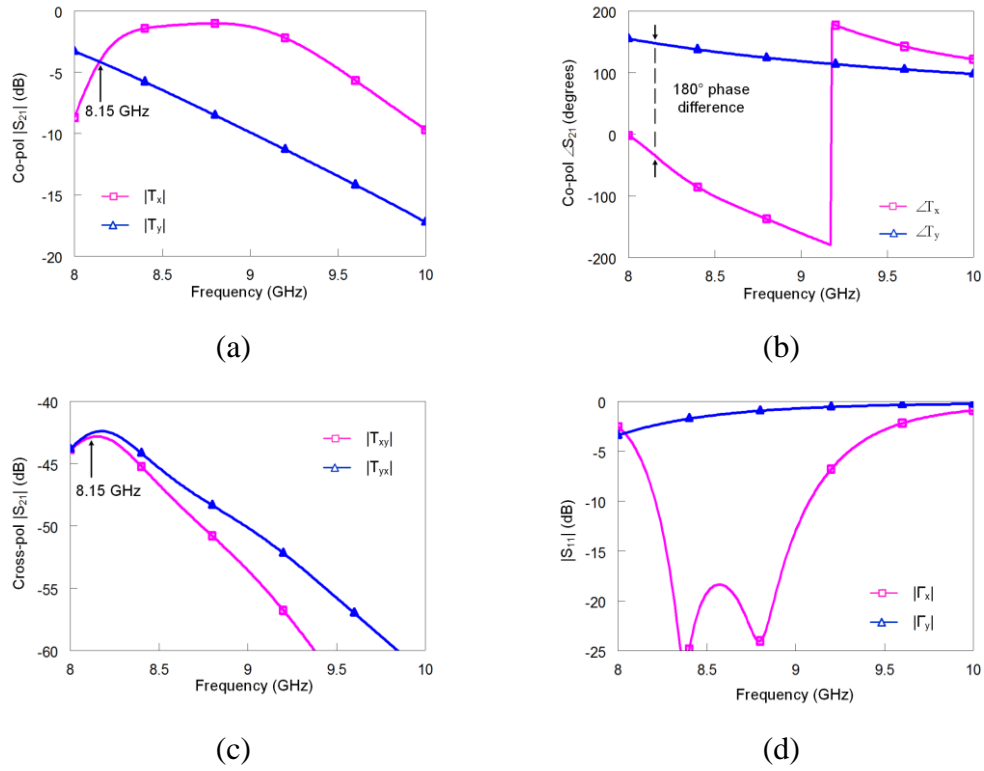| Foam thickness | Glass thickness | Split length | Outer ring radius | Inner ring radius |
|---|---|---|---|---|
| 4.5 mm | 0.5 mm | 2.75 mm | 4.55 – 4.05 mm | 3.15 – 2.65 mm |

Figure A.6     Simulated characteristics of the OS-SRR transmitarray unit cell. (a) Magnitude of the co-pol transmission coefficients, (b) phase of the co-pol transmission coefficients, (c) magnitude of the cross-pol transmission coefficients, (d) magnitude of the reflection coefficients.

# 4.    IS-SRR Unit Cell with Foam Substrate Between the Layers

Figure A.7 shows the IS-SRR unit cell with foam substrate between the layers and the design parameters are given in Table A.4. The reflection, transmission and insertion phase characteristics are shown in Figure A.8.
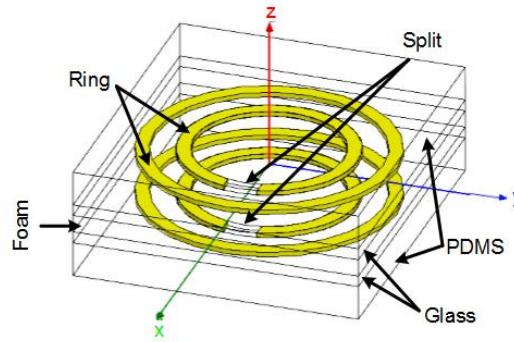


Figure A.7    Geometry of the IS-SRR transmitarray unit cell with foam substrate between the layers.

Table A.4    The values of the parameters of the IS-SRR transmitarray unit cell with foam substrate between the layers.

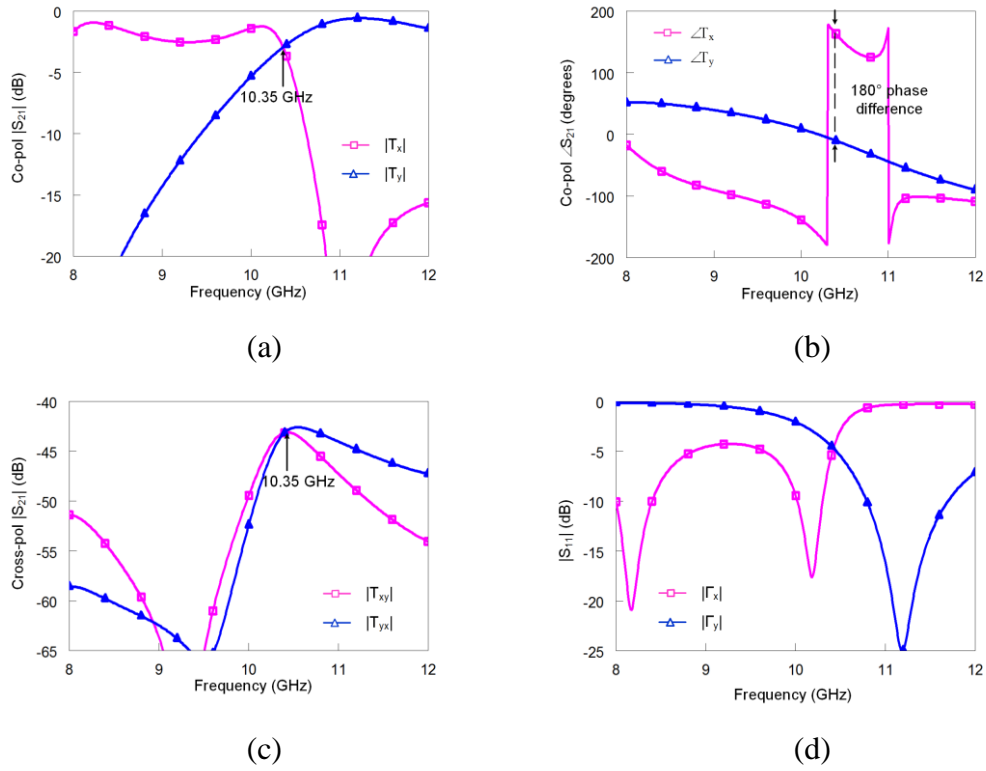| Foam thickness | Glass thickness | Split length | Outer ring radius | Inner ring radius |
|---|---|---|---|---|
| 0.75 mm | 0.5 mm | 1.2 mm | 4.55 – 4.05 mm | 3.15 – 2.65 mm |

Figure A.8    Simulated characteristics of the IS-SRR transmitarray unit cell with foam substrate between the layers. (a) Magnitude of the co-pol transmission coefficients, (b) phase of the co-pol transmission coefficients, (c) magnitude of the cross-pol transmission coefficients, (d) magnitude of the reflection coefficients.

# 5. IS-SRR Unit Cell with Air Gap Between the Layers

Figure A.9 shows the IS-SRR unit cell with air gap between the layers and the design parameters are given in Table A.5. The reflection, transmission and insertion phase characteristics are shown in Figure A.10.
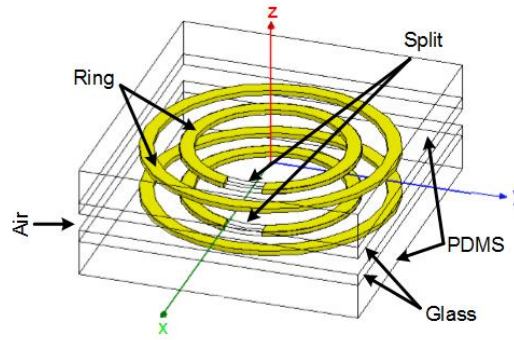


Figure A.9    Geometry of the IS-SRR transmitarray unit cell with air gap between the layers.

Table A.5    The values of the parameters of the IS-SRR transmitarray unit cell with air gap between the layers.

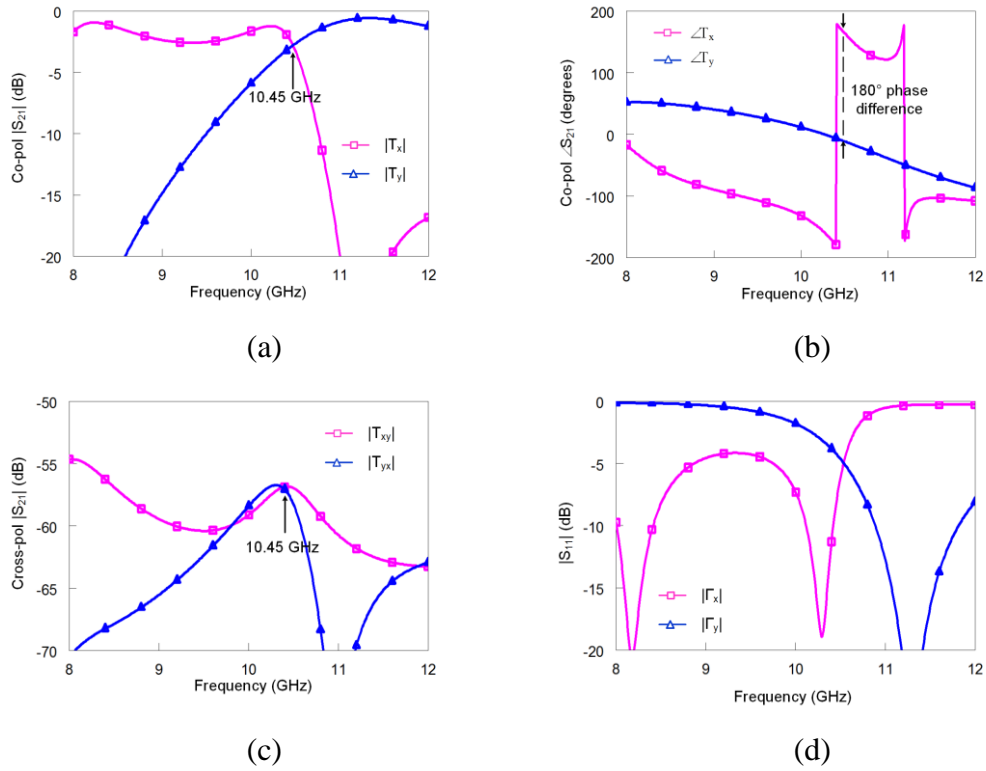| Air thickness | Glass thickness | Split length | Outer ring radius | Inner ring radius |
|---|---|---|---|---|
| 0.75 mm | 0.5 mm | 1.4 mm | 4.55 – 4.05 mm | 3.15 – 2.65 mm |

(a)

(b)

(c)

(d)

Figure A.10    Simulated characteristics of the IS-SRR transmitarray unit cell with air gap between the layers. (a) Magnitude of the co-pol transmission coefficients, (b) phase of the co-pol transmission coefficients, (c) magnitude of the cross-pol transmission coefficients, (d) magnitude of the reflection coefficients.

## 6.     IS-SRR Unit Cell with Glass Substrate

Figure A.11 shows the IS-SRR unit cell with glass substrate and the design parameters are given in Table A.6. The reflection, transmission and insertion phase characteristics are shown in Figure A.12.
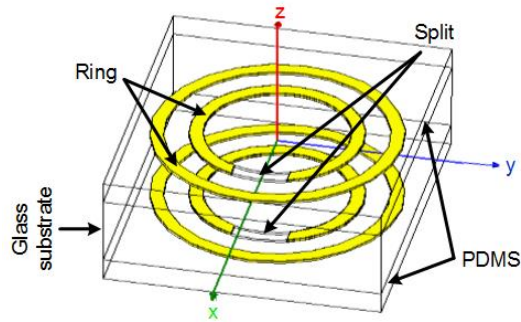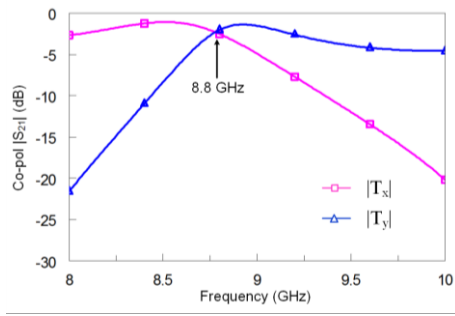


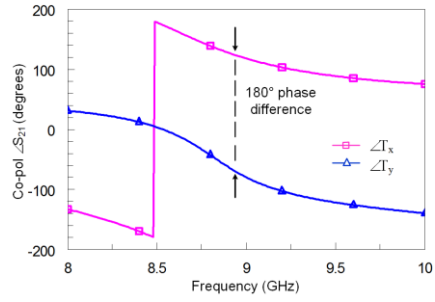Figure A.11    Geometry of the IS-SRR transmitarray unit cell with glass substrate.

Table A.6       The values of the parameters of the IS-SRR transmitarray unit cell with glass substrate.

| Substrate thickness | Split length | Outer ring radius | Inner ring radius |
|---------------------|--------------|-------------------|-------------------|
| 5.5 mm              | 2.05 mm      | 4.55 – 4.05 mm    | 3.15 – 2.65 mm    |

(a)                                      (b)
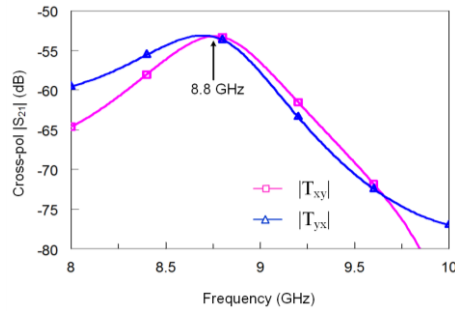
(c)                                      (d)

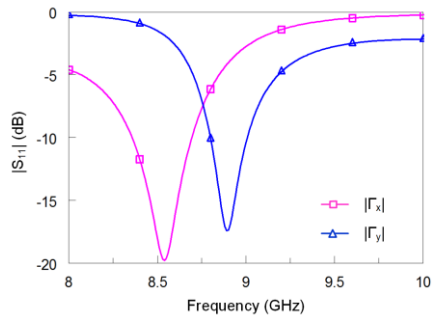Figure A.12    Simulated characteristics of the IS-SRR transmitarray unit cell with glass substrate. (a) Magnitude of the co-pol transmission coefficients, (b) phase of the co-pol transmission coefficients, (c) magnitude of the cross-pol transmission coefficients, (d) magnitude of the reflection coefficients.

# CURRICULUM VITAE

## PERSONAL INFORMATION

Surname, Name: Erdil, Emre
Nationality: Turkish (TC)
Date and Place of Birth: 27 September 1979, Bursa
Marital Status: Married
Phone: +90 312 292 86 38
Fax: +90 312 292 86 03
email: eerdil@gmail.com

## EDUCATION

| Degree | Institution | Year of Graduation |
|---|---|---|
| M.Sc. | METU Electrical and Electronics Engineering | 2005 |
| B.Sc. | METU Electrical and Electronics Engineering | 2001 |
| High School | Atatürk Anadolu High School, Ankara | 1997 |

## WORK EXPERIENCE

| Year | Place | Enrollment |
|---|---|---|
| 2002-Present. | Capital Markets Board of Turkey | Engineer |

## FOREIGN LANGUAGES

Advanced English

## PATENT PENDING

1. E. Erdil, K. Topalli, E. Yildirim, O. Zorlu, Haluk Külah, Ozlem Aydin Civi, PCT/TR2013/000103, International patent application was filed in 2013.

**INTERNATIONAL JOURNAL PUBLICATIONS**

1. E. Erdil, K. Topalli, N. S. Esmaeilzad, O. Zorlu, H. Kulah, and O. A. Civi, "Reconfigurable Nested Ring-Split Ring Transmitarray Unit Cell Employing the Element Rotation Method by Microfluidics," *submitted to IEEE Trans. Antennas Propag.*

2. K. Topalli, E. Erdil, O.A. Civi, S. Demir, S. Koc, and T. Akin, "Tunable dual-frequency RF MEMS rectangular slot ring antenna," *Sensors and Actuators A: Physical*, vol. 156, no. 2, pp. 373-380, December 2009.

3. E. Erdil, K. Topalli, M. Unlu, O. Aydin Civi, and T. Akin, "Frequency Tunable Microstrip Patch Antenna using RF MEMS Technology," *IEEE Trans. Antennas and Propagation*, vol.55, pp. 1193-1196, April 2007.


**INTERNATIONAL CONFERENCE PUBLICATIONS**

1. E. Erdil, K. Topalli, N. S. Esmaeilzad, O. Zorlu, H. Kulah, and O.A. Civi, "A reconfigurable nested ring-split ring transmitarray unit cell by microfluidic technology," *8th European Conference on Antennas and Propagation (EuCAP),* The Hague, Netherlands, April 2014.

2. E. Erdil, K. Topalli, O. Zorlu, T. Toral, E. Yildirim, H. Kulah, and O. Aydin Civi, "Reconfigurable Microfluidic Transmitarray Unit Cells" *14th Workshop on MEMS for MilimeterWave Communications (MEMSWAVE)*, Potsdam, Germany, June 2013.

3. E. Erdil, K. Topalli, O. Zorlu, T. Toral, E. Yildirim, H. Kulah, and O.A. Civi, "A reconfigurable microfluidic transmitarray unit cell," *7th European Conference on Antennas and Propagation (EuCAP),* pp. 2957-2960, April 2013.

4. E. Erdil, K. Topalli, M. Unlu, I. Istanbulluoglu, E. U. Temocin, H. I. Atasoy, O. Bayraktar, O. A. Civi, S. Demir, S. Koc, T. Akin, "Reconfigurable Slot Antenna with Fixed-fixed Beam Type RF MEMS Capacitors," *European Conference on Antennas and Propagation*, Nice, France, 6-10 November 2006.

5. K. Topalli, E. Erdil, O. Aydin Civi, "Reconfigurable Antenna Structures using MEMS technology," *URSI GA 2005*, New Delhi, India, 23-29 October 2005.

6. E. Erdil, S. Onat, K. Topalli, I. Istanbulluoglu, M. Unlu, S. Demir, L. Alatan, O. Aydin Civi, S. Koc, and T. Akin, "Reconfigurable Antenna Structures using MEMS technology," *6th Workshop on MEMS for MilimeterWave Communications (MEMSWAVE),* pp. 35-38, Lausanne, Switzerland, 23-24 June 2005.

7. E. Erdil, K. Topalli,, O. Aydin Civi, and T. Akin, "Reconfigurable CPW-fed dual frequeny rectangular slot antenna," 2005 *IEEE AP-S International Symposium and USNC/URSI National Radio Science Meeting*, Washington D.C., vol.2A, pp. 392-395, 3-8 July 2005.

8. M. Secmen, K. Topalli, M. Ünlü, E. Erdil, O.A. Civi, and A. Hizal, "Dual wideband antenna analysis for linear FMCW radar applications," *IEEE 14th Signal Processing and Communications Applications,* pp. 1-4, April 2006.